

**OPTICAL AND X-RAY DIAGNOSTICS OF A PLASMA
FOCUS**

LEE MING CHUAN

**FACULTY OF SCIENCE
UNIVERSITY OF MALAYA
KUALA LUMPUR**

2017

**OPTICAL AND X-RAY DIAGNOSTICS OF A PLASMA
FOCUS**

LEE MING CHUAN

**DISSERTATION SUBMITTED IN FULFILMENT OF THE
REQUIREMENTS FOR THE DEGREE OF MASTER OF
SCIENCE**

**DEPARTMENT OF PHYSICS
FACULTY OF SCIENCE
UNIVERSITY OF MALAYA
KUALA LUMPUR**

2017

UNIVERSITY OF MALAYA
ORIGINAL LITERARY WORK DECLARATION

Name of Candidate: **LEE MING CHUAN**

Matric No: **SGR130071**

Name of Degree: **Master of Science**

Title of Project Paper/Research Report/Dissertation/Thesis (“this Work”):

Optical and X-ray Diagnostics of A Plasma Focus

Field of Study: **Experimental Physics**

I do solemnly and sincerely declare that:

- (1) I am the sole author/writer of this Work;
- (2) This Work is original;
- (3) Any use of any work in which copyright exists was done by way of fair dealing and for permitted purposes and any excerpt or extract from, or reference to or reproduction of any copyright work has been disclosed expressly and sufficiently and the title of the Work and its authorship have been acknowledged in this Work;
- (4) I do not have any actual knowledge nor do I ought reasonably to know that the making of this work constitutes an infringement of any copyright work;
- (5) I hereby assign all and every rights in the copyright to this Work to the University of Malaya (“UM”), who henceforth shall be owner of the copyright in this Work and that any reproduction or use in any form or by any means whatsoever is prohibited without the written consent of UM having been first had and obtained;
- (6) I am fully aware that if in the course of making this Work I have infringed any copyright whether intentionally or otherwise, I may be subject to legal action or any other action as may be determined by UM.

Candidate’s Signature

Date:

Subscribed and solemnly declared before,

Witness’s Signature

Date:

Name:

Designation:

ABSTRACT

The plasma pinch evolution and X-ray emission of a dense plasma focus are investigated with several diagnostics techniques together with the time resolved and time integrated imaging techniques. The experiment is carried out on the 3.3 kJ Plasma Focus Facility, UNU/ICTP PFF (United Nations University/International Centre for Theoretical Physics Plasma Focus Facility) with neon gas filled at the pressure of 4 mbar. ICCD camera and MCP (microchannel plate) camera setups are established to capture the visible spectra and the X-ray emission from the plasma focus at radial direction aiming on the anode axis. Magnetic probe and an array of PIN diode detectors are used to measure the rate of change of the discharge current and time profile of the X-ray emissions. The time profile of the discharge current and discharge voltage signals are correlated to the timing of the ICCD imaging and MCP imaging. An X-ray spectrometer is employed to measure the integrated emission of the neon plasma. The current sheath dynamics in their radial trajectory and compression phase have been revealed by a series of images carefully obtained at different timings. The neon plasma focus is observed to have multiple compressions. The radial compression phase is explained by considering three main regions (first region, second region and third region). Neon X-ray emission is observed in the first region, while X-ray emission from copper K-alpha is measured in the second and third region. The electron temperature estimated based on the neon X-ray emission is around 500 eV and the highest electron temperature has been estimated at 10 keV.

ABSTRAK

Evolusi plasma fokus dan sinaran X daripada satu padat plasma fokus telah dikaji dengan beberapa diagnostik teknik bersama dengan teknik pengimejan masa tentu dan masa integrase. Eksperimen ini dikendalikan dengan gas neon pada 3.3 kJ UNU / ICTP PFF (United Nations University/International Centre for Theoretical Physics Plasma Focus Facility) pada 4 mbar. Kedua-dua kamera ICCD dan MCP (microchannel plate) digunakan untuk menangkap imej pada keadaan spectrum kasar mata dan sinaran X pada arah jejarian paksi anod. Menduga magnet dan pengesan PIN diod digunakan untuk menangkap kadar perubahan arus nyahcas dan sinaran X. Kadar perubahan arus nyahcas dan voltan nyahcas digunakan untuk menunjukkan masa imej ICCD. Satu spektrometer X-ray digunakan untuk mendapatkan tenaga integrasi bagi plasma fokus neon. Satu siri dinamik arus sarung imej dalam fasa jejarian trajektori dan mampatan telah digambarkan pada masa yang berbeza. Plasma fokus neon dalam eksperimen ini didapati adalah pelbagai pemampatan. Keputusan fasa mampatan jejarian ini dibahagikan kepada tiga rantau utama (rantau pertama, rantau kedua dan rantau ketiga). Rantau pertama adalah di mana pelepasan sinaran X neon dipancarkan; pelepasan sinaran X di rantau kedua dan ketiga adalah kuprum tembaga K-alfa. Majoriti pelepasan sinaran X adalah 500 eV tetapi suhu elektron yang paling tinggi boleh dicapai dalam eksperimen ini adalah 10 keV.

ACKNOWLEDGEMENTS

I would like to express my deepest gratitude to my supervisor, Associate Professor Dr. Yap Seong Ling, a respectable and responsible scholar who has guided me on the various aspects of my research project.

I sincerely thank Mr. Jasbir Singh for his assistants and for providing his invaluable knowledge and experience. I would also like to thank Prof. Wong Chiow San and Prof Lee Sing for ideas shared. In addition, I am very grateful to Mr. Lim Lian Kuang, Mr. Ngoi Siew Kien and Mr. Ma Jian for their help, suggestions and encouragement. The lab has been the most enjoyable and productive workplace though we have to share many equipment and facilities. I would also like to thank Dr. Zubair and Mr. Rosli Abdullah for their help and support, and all the lab mates, seniors and juniors, with whom we have worked together and solved many problems

I would like to express my heartfelt gratitude to my parents and sisters for the tremendous support and encouragement throughout the duration of my study.

Lastly, I dedicate the work to the Plasma Research Laboratory, Department of Physics for providing the environment for us to carry out fundamental research on plasma physics. Facilities and grants from University of Malaya, Ministry of Education, Malaysia Toray Science Foundation are gratefully acknowledged.

TABLE OF CONTENTS

ABSTRACT	iii
ABSTRAK	iv
ACKNOWLEDGEMENTS	v
TABLE OF CONTENTS	vi
LIST OF FIGURES	viii
CHAPTER 1: INTRODUCTION	1
1.1 Objective of the Dissertation	2
1.2 Breakdown/lift-off phase	3
1.3 Rundown/acceleration phase	3
1.4 Radial compression/collapse phase	4
CHAPTER 2: LITERATURE REVIEW	8
2.1 Single Pinch and Multiple Pinches	8
2.2 Plasma Focus Imaging	10
2.3 First region imaging	11
2.4 Hot Spot	13
2.5 Plasma Bubble	14
2.6 After Plasma Bubble	16
2.7 Rate of Change of Discharge Current (dI/dt)	16
2.8 Plasma Focus as X-rays Source	17
2.9 Plasma Focus Modeling: Lee Model	19

CHAPTER 3: EXPERIMENTAL SETUP	20
3.1 Plasma Focus Facility	22
3.1.1 Triggering Unit.....	23
3.1.2 Plasma Focus Tube.....	24
3.1.3 Capacitor Bank and Spark Gap Switch	25
3.1.4 High Voltage Charger	26
3.1.5 MCP chamber.....	27
3.2 Diagnostic Tools.....	28
3.2.1 Array of PIN Diode Detectors.....	28
3.2.2 Multiple Pinholes Camera.....	32
3.2.3 Rogoswki Coil / Magnetic Probe	34
3.2.4 Voltage Probe	36
3.2.5 X-ray Spectrometer (XR-100 CR)	37
3.2.6 Microchannel Plate (MCP).....	38
3.2.7 ICCD camera.....	40
3.2.8 X-ray Film Processing.....	40
CHAPTER 4: RESULT AND DISCUSSION	
4.1 Introduction.....	41
4.2 Results and Analysis.....	43
CHAPTER 5: CONCLUSION.....	86
SUGGESTION FOR FUTURE WORK	89
REFERENCES	90
LIST OF PUBLICATIONS AND PAPERS PRESENTED	96
APPENDIX	97

LIST OF FIGURES

Figure 1.1	: Filippov type (left) and Mather type (right).....	2
Figure 1.2 (a)	: Three phases of plasma focus discharge for breakdown / lift-off phase	5
Figure 1.2 (b)	: Three phases of plasma focus discharge for rundown / acceleration phase	6
Figure 1.2 (c)	: Three phases of plasma focus discharge for radial compression / collapse phase	7
Figure 2.1 (a)	: Multiple pinches result examples for three main phases	9
Figure 2.1 (b)	: Multiple pinches result examples for three main regions	10
Figure 3.1 (a)	: Schematic diagram of the experimental setup for side view	21
Figure 3.1 (b)	: Schematic diagram of the experimental setup for top view.....	22
Figure 3.2	: Plasma focus facilities schematic diagram	23
Figure 3.3	: Geometrical arrangement of anode and cathode 3D schematic diagram	24
Figure 3.4	: Capacitor and swinging cascade spark gap schematic diagram.....	26
Figure 3.5	: Charger and dumping switch schematic diagram	27
Figure 3.6	: Schematic showing a set of PIN diode detector and the biasing circuit	28
Figure 3.7	: Array of pin diode detectors 3D schematic diagram.....	30
Figure 3.8	: Sensitivity curve for different filter thickness.....	31
Figure 3.9	: Graph of ratio versus aluminum foil thickness at different plasma electron temperature	31
Figure 3.10	: Multiple pinholes camera 3D schematic diagram	32
Figure 3.11	: Pinholes' image resolution where x is pinched plasma size (object size), p is pinhole size, q is image size, L_0 is distance between pinched plasma and pinhole, L_1 is distance between pinhole and image	33

Figure 3.12	: Rogowski coil schematic diagram	34
Figure 3.13	: Reversal ratio (peak voltage from first to fifth)	35
Figure 3.14	: Voltage probe schematic diagram	36
Figure 3.15	: Voltage divider principal schematic diagram	37
Figure 3.16	: X-ray spectrometer schematic diagram	38
Figure 3.17 (a)	: Microchannel plate and pulse generator for MCP	39
Figure 3.17 (b)	: Microchannel plate and pulse generator for pulse generator	39
Figure 3.18	: Sensitivity curve for gold foil + mylar	39
Figure 3.19	: MCP process	40
Figure 4.1	: Typical results of high voltage probe, magnetic probe, array of PIN diode detectors, ICCD and MCP	42
Figure 4.2 (a)	: Before first region pinch for axial acceleration phase	53
Figure 4.2 (b)	: Before first region pinch for end of axial acceleration phase and at the point of beginning of the radial compression phase	54
Figure 4.2 (c)	: Before first region pinch for radial compression phase	55
Figure 4.2 (d)	: Before first region pinch for radial compression phase	56
Figure 4.2 (e)	: Before first region pinch for radial compression phase	57
Figure 4.2 (f)	: Before first region pinch for radial compression phase	58
Figure 4.2 (g)	: Before first region pinch for radial compression phase	59
Figure 4.2 (h)	: Before first region pinch for radial compression phase	60
Figure 4.3 (a)	: First region pinch for distortion observed on current sheath due to RT instability, arrow 1 and 2 in dI/dt show in MCP3 (X-ray emitted from elongated plasma column) and MCP4 (column breaks into hot spots) respectively	61
Figure 4.3 (b)	: First region pinch for MCP2 and MCP3 at the peak of V (arrow) and dI/dt (arrow) where plasma column elongated and break into hot spots respectively	62

Figure 4.3 (c)	: First region pinch for MCP open shuttle time is 20 ns, kink instabilities is clearly view, ICCD's image shows the first compression at the first peak of dI/dt (arrow) and before first peak of V (arrow)	63
Figure 4.3 (d)	: First region pinch for arrow 1 (V and dI/dt) is first compression and plasma column elongated, arrow 2 (dI/dt , MCP2) is hot spots, arrow 3 (dI/dt , MCP4) is second compression breaks into hot spot ..	64
Figure 4.3 (e)	: First region pinch for arrow 1 of dI/dt is maximum compression, arrow 2 is plasma column break down as shown in MCP1	65
Figure 4.3 (f)	: First region pinch for in ICCD's image, the bottom black arrow 1 is hot spot from first compression, the upper black arrow 2 is second compression, arrow in dI/dt is second compression plasma column breaks into hot spots	66
Figure 4.3 (g)	: First region pinch for in ICCD's image, the bottom black arrow 1 is hot spot from first compression undergoes diffusion, the upper black arrow 2 is second compression	67
Figure 4.3 (h)	: First region pinch for a layer of visible light is observed on the anode's surface, arrow in dI/dt shows remaining plasma is compressed to higher area	68
Figure 4.3 (i)	: First region pinch for the remaining plasma is compressed into another intense spot	69
Figure 4.3 (j)	: First region pinch for intense spot starts to decay and induce a shock wave	70
Figure 4.3 (k)	: First region pinch for induced shock wave move outward and form plasma bubble	71
Figure 4.4 (a)	: Second region pinch for plasma bubble continues expand	72
Figure 4.4 (b)	: Second region pinch for another pinch is formed inside plasma bubble, top of plasma bubble distorted may due to burst out of ion beams	73
Figure 4.4 (c)	: Second region pinch for ablation of anode continues	74
Figure 4.5 (a)	: Ablation on anode for ablation of anode continues	75
Figure 4.5 (b)	: Ablation on anode for ablation of anode continues	76
Figure 4.5 (c)	: Ablation on anode for ablation of anode continues	77

figure 4.6 (a)	: Plasma temperature first region pinch for electron temperature of peak 1 and 2 in X5 from Figure 4.3(a)	78
Figure 4.6 (b)	: Plasma temperature first region pinch for electron temperature of peak 1 and 2 in X5 from Figure 4.3(d)	78
figure 4.7	: Neon X-ray (X2) and copper K-alpha (X1), X1 detected is 1 ns later 1 after X2	79
figure 4.8 (a)	: Black spots (inside white circle) observed on the surface of the anode at sharp drop of dI/dt for before dI/dt sharp drop	79
figure 4.8 (b)	: Black spots (inside white circle) observed on the surface of the anode at sharp drop of dI/dt for when dI/dt sharp drop	79
figure 4.9	: Second region pinch image	80
figure 4.10	: Third region pinch image	81
figure 4.11 (a)	: After third region pinch for more copper vaporized	82
figure 4.11 (b)	: After third region pinch for copper vapour diffuse into surrounding	82
figure 4.11 (c)	: After third region pinch for copper vapour diffuse into surrounding	82
figure 4.11 (d)	: After third region pinch for copper vapour starts compressed when V goes into positive cycle	83
figure 4.11 (e)	: After third region pinch for copper vapour compressed	83
figure 4.11 (f)	: After third region pinch for compression continues	83
figure 4.11 (g)	: After third region pinch for starts to diffuse when V enter reverse cycle	84
figure 4.11 (h)	: After third region pinch for diffusion continues	84
figure 4.11 (i)	: After third region pinch for re-compressed again, and starts diffuse when enter reverse cycle	84
figure 4.11 (j)	: After third region pinch for diffuse into surrounding	85
figure 4.11 (k)	: After third region pinch for diffuse into surrounding	85
figure 4.12	: X-ray spectrometer accumulated 234 successive shots, below 400 eV are majority background radiation, majority of Neon X-ray is 500 eV but both PIN diode detector and MCP are not sensitive to 500 eV range	85

CHAPTER 1: INTRODUCTION

Two types of plasma focus devices; Mather type and Filippov type were developed independently in 1960s and named after their founders Mather (United States) and Filippov (Soviet Union), respectively (Filippov et al., 1962; Mather, 1965). The schematic of the two types of the plasma focus are shown in Figure 1.1.

In this project, Mather type plasma focus is used. The Mather type is advantage as X-ray source as the pinch can be observed from both end-on and side-on direction. Plasma focus discharge produces a hot and dense plasma with typical density of $2 - 3 \times 10^{-19} \text{cm}^{-3}$ and temperature of 1-3 keV (Mather, 1965). Plasma emission covers a broad spectrum such as X-rays, EUV and charged particles where its characteristic is dependent on the operating gas and energy supplied to the plasma focus (Mather, 1965).

The formation of the pinched plasma is due to the electromagnetic acceleration and compression of the current sheath. The evolution of the plasma focus discharge can be divided into three phases, started with the breakdown/lift-off phase followed by the rundown/acceleration phase and finally the radial compression/collapse phase (Mather, 1971).

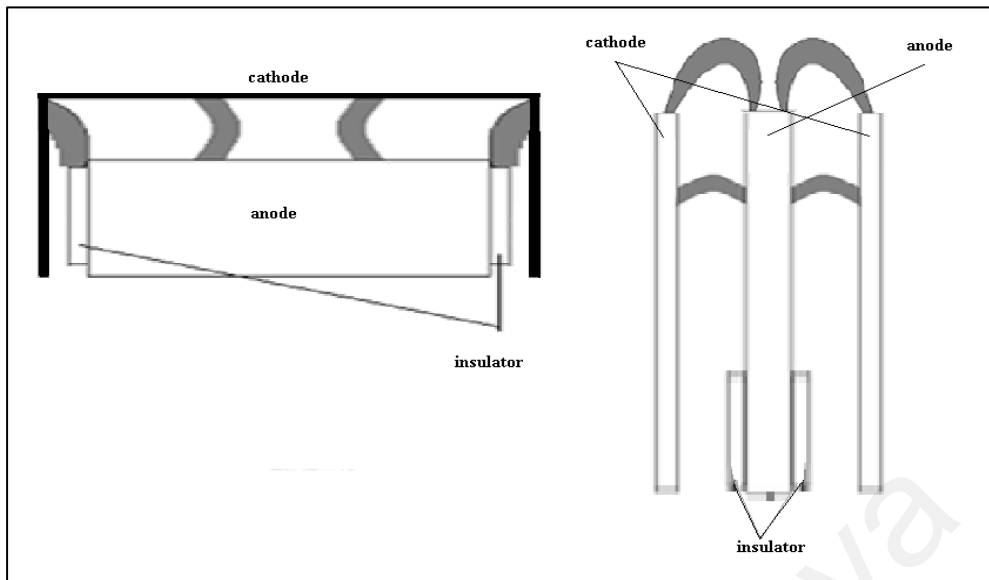


Figure 1.1: Filippov type (left) and Mather type (right).

1.1 Objective of the Dissertation

Detailed formation of the plasma pinch in the plasma focus device remain unclear although the development of plasma focus device dated back to year 1962 and 1965. The understanding of the mechanisms involved in pinch formation shall provide insights to enable the device to be formulated for various applications, including fusion study, particle beam source and X-ray sources. High speed visible frame imaging will be of great advantage to reveal the dynamic of the plasma while X-ray emission measurements give information about the formation of the hot dense plasma.

The objectives of this project are to investigate the formation of the Neon plasma focus operated at the filling pressure of 4 mbar. The time resolved and time integrated measurement techniques are developed and applied simultaneously to investigate the pinched plasma; based on the X-ray emissions and visible emissions from the plasma. This includes imaging techniques with ICCD for the current sheath, gated MCP and

X-ray pinhole imaging for X-ray emissions, all focused at the pinch phase, together with other electrical diagnostics and spectroscopy. Series of plasma pinch images obtained for the plasma pinching and emitting zone are correlated with the X-ray signals and the current and voltage signals.

1.2 Breakdown/lift-off phase

The breakdown phase is the initial phase when high voltage supplied into anode, the high voltage will track along the insulator surface to cathode. The insertion of insulator between the anode and cathode in the plasma focus device is essential as it plays the important role to prevent the current discharge directly from the anode to the cathode. Stray electrons are attracted to the insulator and gain energy. The electrons will collide with atoms and emit secondary electrons. This process continues, gas ionization occurs and forms a high current track along the insulator surface from the anode to the cathode where the current sheath will be formed. Then, a magnetic field, B is induced around the anode in the azimuthal direction (using right hand grip rule) due to the high current. Next, a Lorentz force J (current density) $\times B$ (magnetic field) will act on the current sheath to form a curve shape (Figure 1.2(a)), a second phase which is the rundown phase will begin.

1.3 Rundown/acceleration phase

In this phase, the lifted current sheath will start to accelerate towards the end of the anode driven by its self-generated Lorentz force (Figure 1.2(b)). During the propagation, the current sheath acts like a snowplow machine to collect the gas particles it encounters. Towards the end of this phase, the current sheath will reach the end of anode and this marks the beginning of radial compression phase.

1.4 Radial compression/collapse phase

In this phase (Figure 1.2(c)), the current sheath starts to accelerate radially inwards towards the center of anode axis. The current sheath eventually compresses and forms a plasma column. Finally the plasma column breaks into high temperature and high density hotspots with radiation emissions depending on the pinching and operating conditions.

University of Malaya

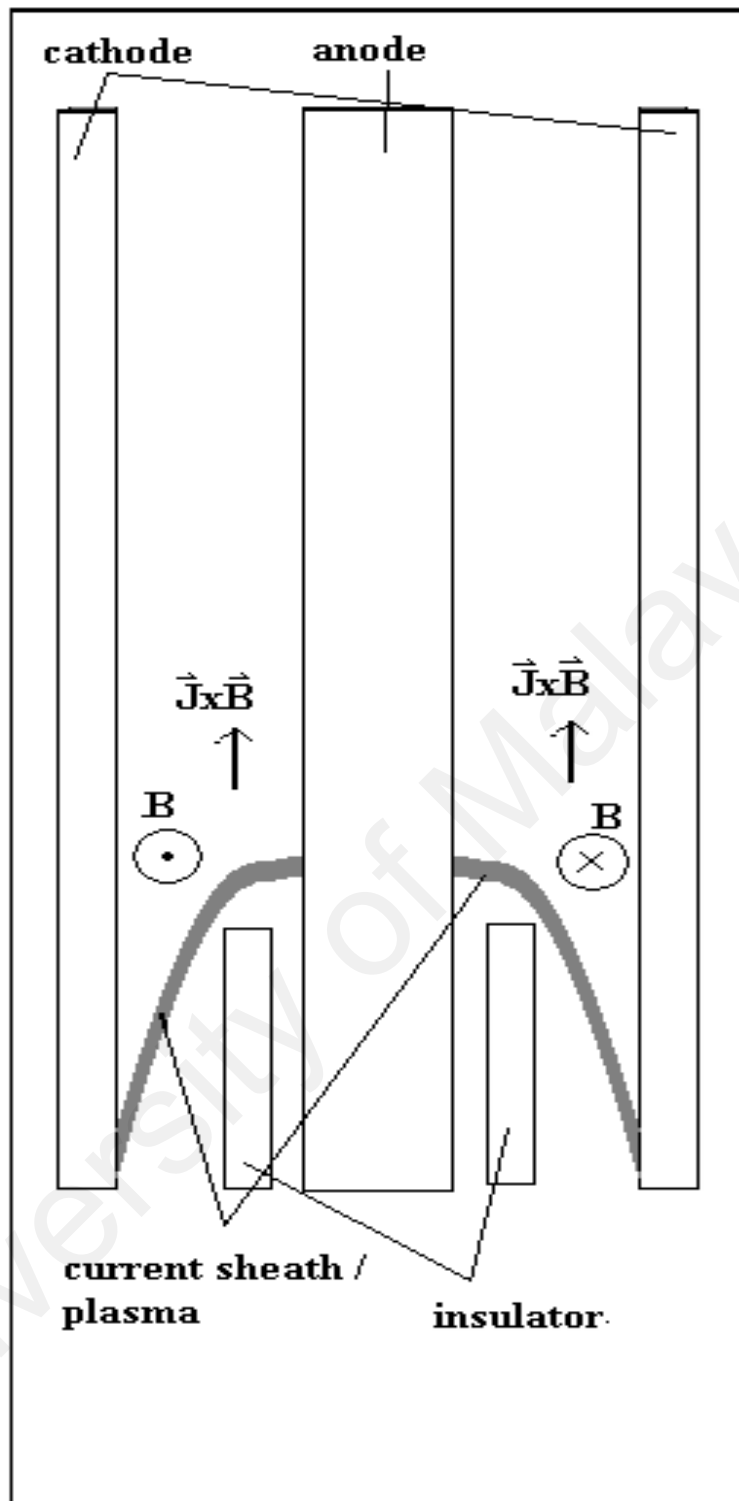


Figure 1.2(a): Three phases of plasma focus discharge for breakdown / lift-off phase.

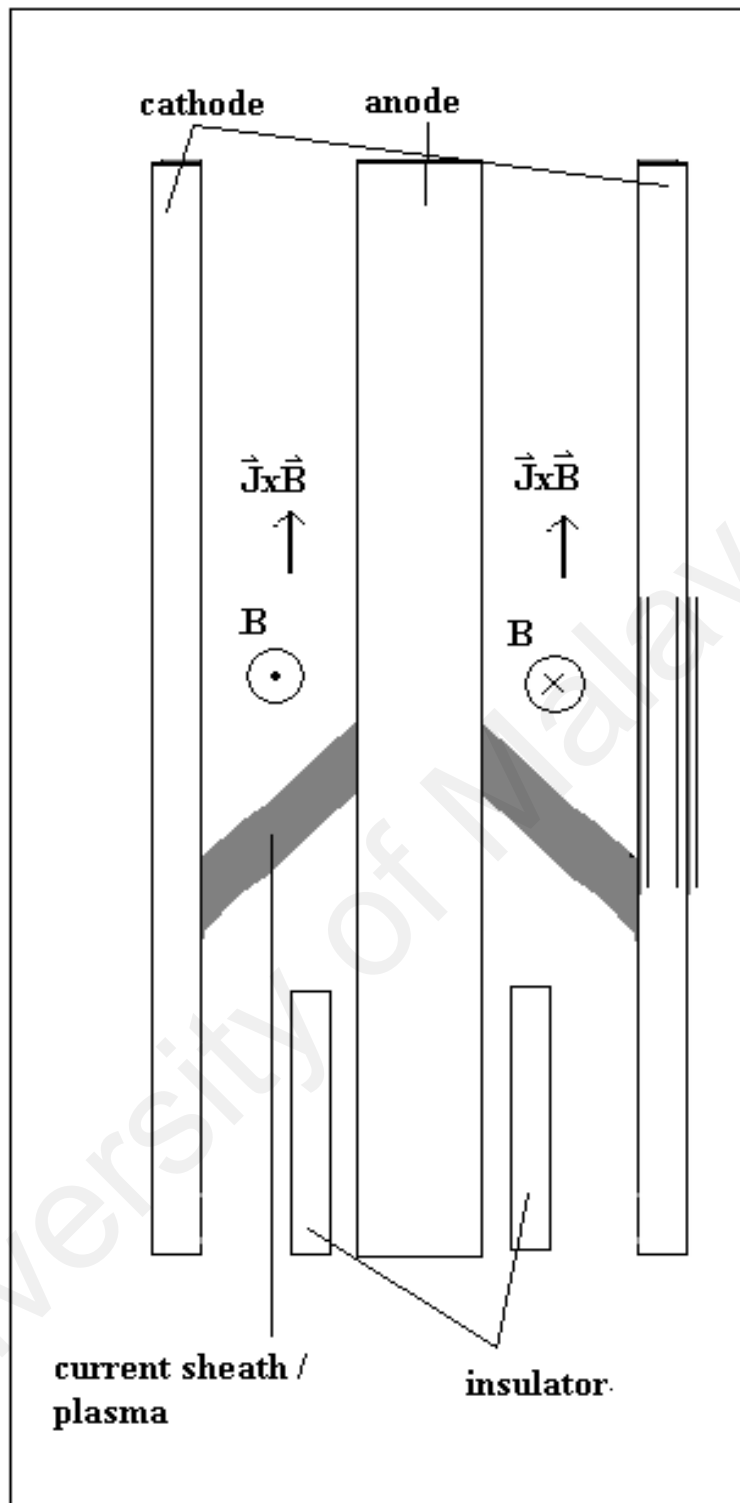


Figure 1.2(b): Three phases of plasma focus discharge for rundown / acceleration phase.

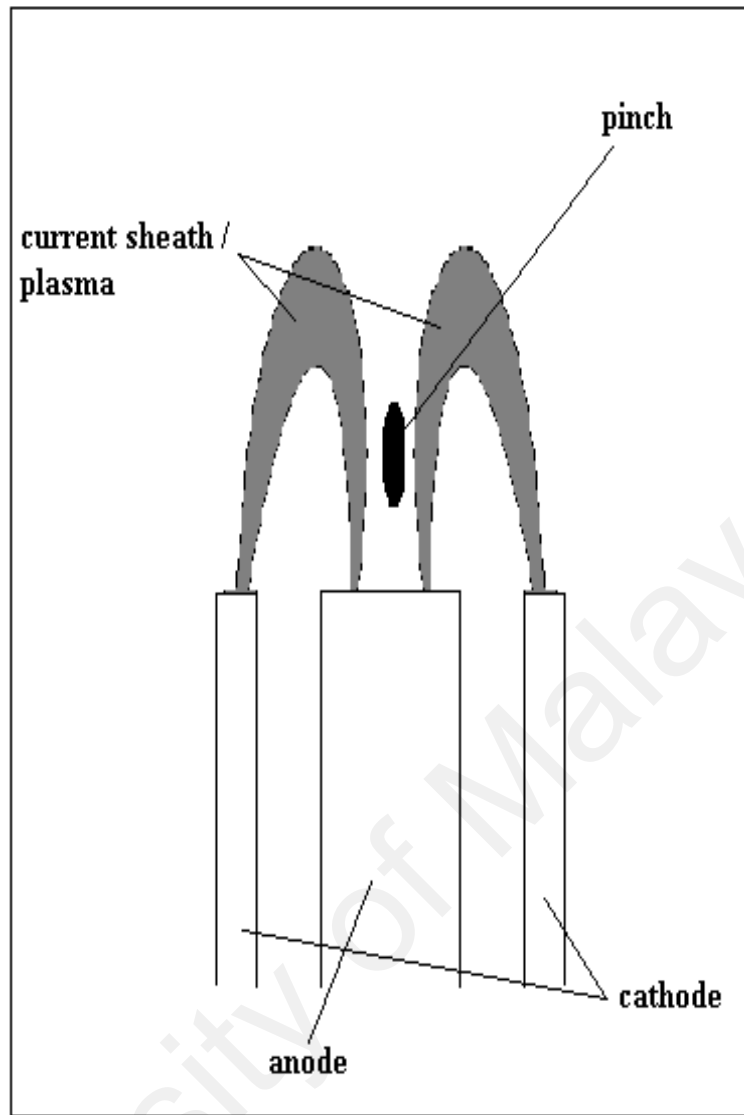


Figure 1.2(c): Three phases of plasma focus discharge for radial compression / collapse phase.

CHAPTER 2: LITERATURE REVIEW

In early research, the plasma focus was studied as a nuclear fusion facility (Filippov et al., 1962; Mather, 1965). Many researches have been carried out in order to study and understand both dynamics and emissions of the plasma focus (Goh et al., 2013; Goudarzi et al., 2017; Hirano et al., 1986; Lim et al., 2016; Lim et al., 2013; Momenei et al., 2017; Rafique et al., 2010; Shad Sanjabad et al., 2017; Tzeng et al., 1992; Vinogradov et al., 2016; Yap & Wong, 2003). Theoretical works have been done to improve efficiency of the plasma focus (Akel et al., 2009; Lee, 2014; Lim et al., 2017; Raeisdana et al., 2017; Saw et al., 2014).

2.1 Single Pinch and Multiple Pinches

Presence of either single pinch or multiple pinches is a characteristic feature of plasma focus discharge. This indicates either single spike or multiple spikes shown on discharge voltage and rate of change of discharge current measurement on oscilloscope. The voltage probe signal shows multiple spikes indicates multiple compressions because of either uneven energy transfers into plasma focus system from capacitor or weak current sheath formation near insulator surface during break down phase. The first and second region voltage spikes occur due to first and second pinch respectively. The third region voltage spike occurs probably due to sputtering of anode (Rafique et al., 2010).

An observation on the current and voltage signals indicating multiple pinches is shown in Figure 2.1. The three main phases of plasma focus dynamic is marked in Figure 2.1(a) and the extended time scale showing the pinch region is shown in Figure 2.1(b). In Figure 2.1(b), the three regions indicate first, second and third pinch respectively, though practically the signals can reflect more mechanisms in one region, in which cases more than one pinch (with a single voltage spike) occur in one region. Following the signals, we could read that the first pinch forms during the radial compression phase; second region occurs around 150 ns to 200 ns from the first pinch; third region occurs around 450 ns to 500 ns from the first pinch.

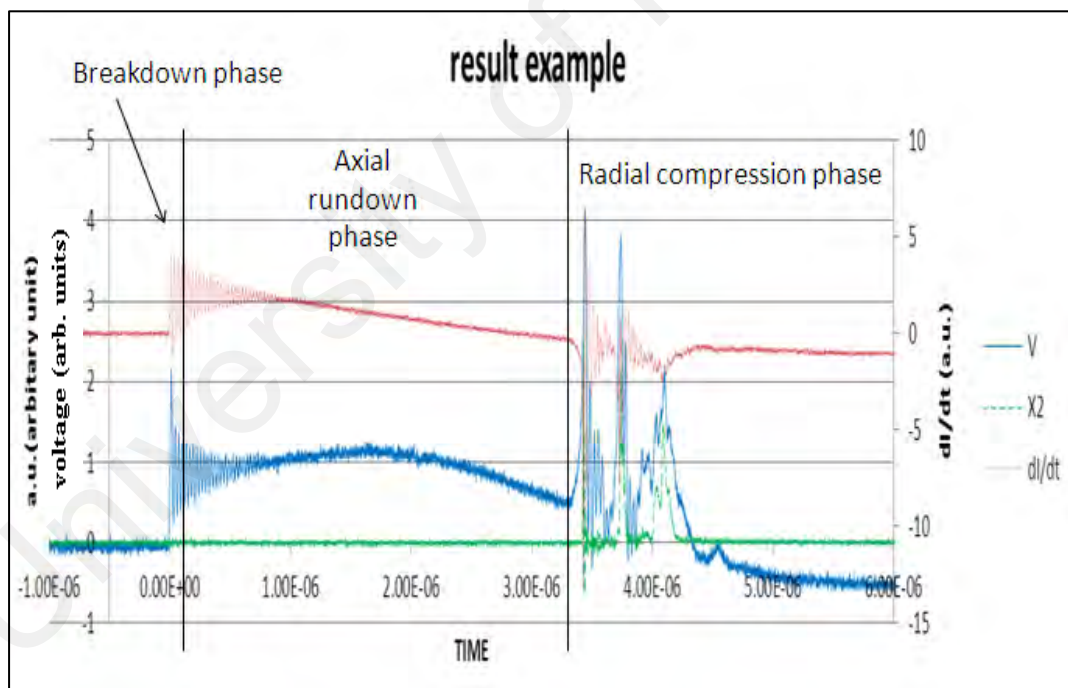


Figure 2.1(a): Multiple pinches result examples for three main phases.

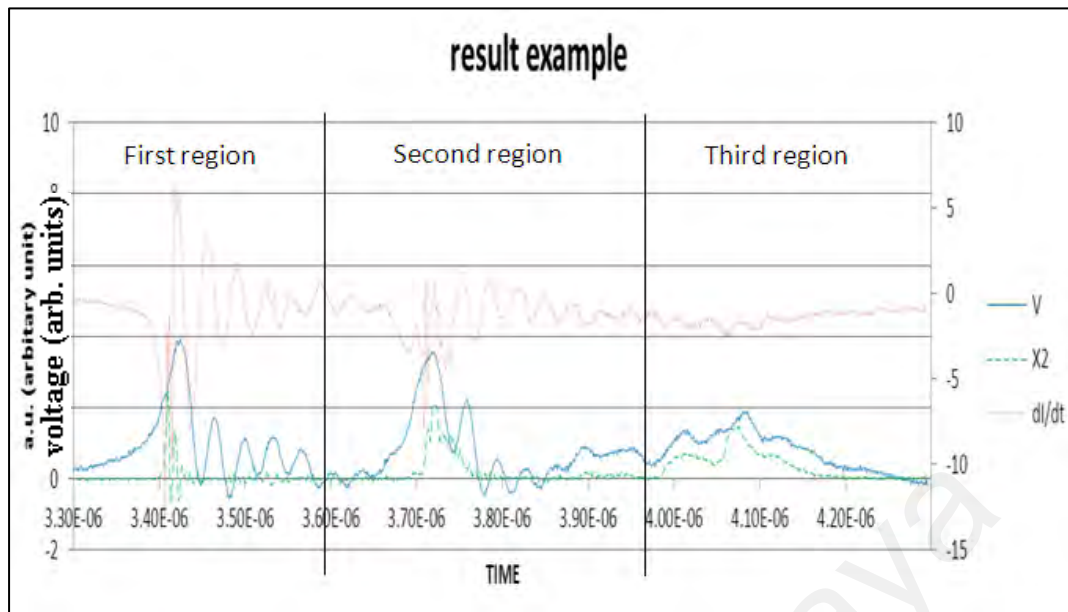


Figure 2.1(b): Multiple pinches result examples for three main regions.

2.2 Plasma Focus Imaging

Previous studies have reported a series of radial compression phase images (Borowiecki et al., 2006; Chen, 1972; Gribkov et al., 2007; Gribkov et al., 2007; Kalaiselvi et al., 2015; Kwek, 1989; Rafique et al., 2010; Soh et al., 2004; Soto et al., 2014; Tzeng et al., 1992). At the radial compression phase, the current sheath move into center axis of the anode. At the center axis of the anode, the current sheath compressed into a plasma column, coupled with magnetic field and breaks into small hot spots due to instabilities.

Kwek (Kwek, 1989; Kwek et al., 1990), Soh (Soh et al., 2004) and Rafique (Rafique, 2000) have observed shock front and magnetic piston (current sheath) at axial acceleration phase. As the shock front move forward, more gas particles pushed forward and cause the shock front slowdown. Moreover, along the axial acceleration phase, the velocity of current sheath will continue increase (Al-Hawat, 2004; Saw et

al., 2012). When reach radial compression phase, shock front and current sheath is seen to be closely to each other.

2.3 First region imaging

Based on Rafique's results (Rafique et al., 2010), first region of radial compression phase has divided into three phases, pre-focus phase, focus phase and post phase. At pre-focus phase, the current sheath starts to move into the open end of anode and accelerates towards center axis of anode. When current sheath is about to reach the center axis of the anode, Rayleigh-Taylor instability can be seen on current sheath. Follow by focus phase which occurred during and near maximum compression, the current sheath compressed into plasma column. X-ray emission, neutron, ion and electron beams emitted during or near maximum compression. Lastly is post-focus phase, the plasma column decays and breaks into single or few hot spots due to instabilities. Moreover, Gribkov reports the plasma pinch image has observed filament, halo, copper vapour and plasma diode; ion beam with few discs occurred after the plasma pinch (Gribkov et al., 2007; Gribkov et al., 2007).

Besides that, Borowiecki (Borowiecki et al., 2006) has used streak camera to capture radial compression phase. At time $t = 0$ is when current sheath compressed into minimum diameter of the plasma column as well as peak soft X-ray occurred. The minimum diameter of the plasma column is also known as maximum compression. The second compression has an implosion of a weak radiation plasma surround by low temperature and low density plasma (dark region); the compression diameter decrease

and intensity of the compression increase. Borowiecki suspected the second compression occurred very fast and failed to capture by frame images; the frame images capture have shown similar dense structure with the first compression.

On the first region, Hirano (Hirano et al., 1986; Hirano et al., 1985) has used microchannel plate (MCP) to observe X-ray emission from the plasma pinch. The soft X-ray emitted from the plasma column before the maximum compression near anode and lasts for 60 to 70 ns (8.15 kJ). The peak of the first X-ray emission approximate to the maximum compression based on time resolve image from Mach-Zehnder interferometer. After the maximum compression is expanding phase, the electron density distributed almost uniformly above anode in axial direction. Followed by unstable phase, where macroscopic instabilities observed in the collapse plasma column. In this phase, most intense X-ray observed with higher electron temperature but lower electron density at the constricted area. Next, a high intensity spot observed at the center part of the plasma from the plasma column disrupted. Finally after disrupted phase, X-ray emitted from the anode surface or interaction with the evaporation of the anode material. Similarly results have been obtained by Tzeng (Tzeng et al., 1992).

By comparing Hirano (Hirano et al., 1985) and Rafique (Rafique et al., 2010) radial compression phase, the focus phase (Rafique) is similar to the maximum compression and expanding phase (Hirano). The post focus phase is including unstable phase and disrupted phase.

2.4 Hot spot

Decker (Decker et al., 1996) has reported after the maximum compression, the macroscopic instabilities $m = 0$, the plasma column disrupted and first necking area developed near the anode. Later necking area also developed at higher Z position and last for 70 to 100 ns (SPEED 2) but lower necking area already decay. The necking areas followed by micropinch and decay; the diffusing areas often failed to produce micropinch. By using stronger filters, a small spot observed at the necking area surrounded by softer radiation. The small spot is also known as hot spot. By looking back to Hirano's results, the high intensity spots are same position with the constricted area (necking area) which agree with Decker's results. Similarly, Favre (Favre et al., 1998) also has used different filter pairs on pin hole camera, softer filter pair and harder filter pair. Through this, Favre has estimated the electron temperature of hot spots. Favre has found out that both filter pairs have given different electron temperature; softer filter pair has colder electron temperature than harder filter pair. Favre stated that majority X-ray emission detected through softer filter pair is lower temperature plasma; whereas harder filter pair has attenuated the lower temperature plasma and allowed K-shell emission from Argon ions to pass through.

Later, Jakubowski and Rawat (Jakubowski et al., 2000; Jakubowski & Sadowski, 2002; Rawat et al., 2004) have reported hot spots have stochastic characteristic in electron density and plasma temperature, formation of hot spots are independent with each other and emit X-ray emission one after the other. Each hot spot is surrounded by lower temperature plasma and lasts for 10 ns (MAJA-PF); whole hot spot population

sustains around 100 ns (MAJA-PF). If distance between two hot spots formed in about 1 mm, the earlier hot spot formed will heat up next hot spot formed. The X-ray radiation emitted from several hot spots only will give average characteristic. Thus, Jakubowski (Jakubowski et al., 2004) has use a crowned quasi conical prominence (anode shape like a small cone laid on a cylinder) to form a single hot spot for further study.

Plasma column breaks into hot spots due to either instabilities or may due to density fluctuation connected with micro turbulences (Lee, 2014; Rafique et al., 2010). When plasma column breaks up, the ion velocity no longer Maxwellian, the intensity of scattered light increase more than thermal level. Rafique proposed that these instabilities proportional to drift velocity which were created by the flowing current between the electrons and ions. Increase in the drift velocity cause the breaking up of plasma column into more hot spots and radiation. During the plasma pinch, inductance of the pinch much higher than resistance. Plasma gains energy through Joule heating and energy loses through X-ray emission.

2.5 Plasma bubble

In addition, Gribkov has reported the plasma pinch is always accompanied by a hemisphere shock wave. Chen (Chen, 1972), Tzeng (Tzeng et al., 1992), Borowiecki (Borowiecki et al., 2006) and Gribkov (Gribkov et al., 2007; Gribkov et al., 2007) have used fast frame camera to capture visual wavelength range images. From Tzeng's results, a bubble like shock wave occurs after the plasma column breakdown but

Chen's results failed to observe clearly due to 20 ns exposure duration where as Tzeng used 10 ns; Borowiecki's results only have shown until the pinch column breakdown. In Kwek's result (Kwek, 1989), a very good resolution radial compression phase images have been obtained with Schlieren system but the results also have shown until the pinch column breakdown. Other researchers (Kalaiselvi et al., 2015; Rafique et al., 2010; Soh et al., 2004; Soto et al., 2014) have either used Schlieren system or shadowgraphy system to obtain radial compression phase images; all results have shown bubble like (plasma bubble) occur after the plasma column breakdown.

Choi (Choi et al., 1989) has used streak camera to capture 5 to 10 ns after maximum compression at radial compression phase along x-axis direction (DPF-78). Four types of filters are used; softer filtered 150 nm Ag and 150 nm Ag + 2.5 μm Kimfol + 0.4 nm Al, harder filtered 5 μm Kimfol + 150 nm Al and 3.15 μm Al. For softer filtered, three classes of plasma have been identified. First, current sheath compressed into plasma column and elongated axially; second is plasma move toward to anode and third is plasma move away from anode. After 40 to 80 ns, a second plasma emission (plasma blob or plasma bubble) observed at a position of the third class of plasma. The plasma bubble also extends axially toward and away from anode. Similarly, Tzeng (Tzeng et al., 1992) also has reported same streak camera images as Choi by using streak camera at radial compression phase along x-axis (3.2 kJ plasma focus device). The image shows clearer view of three classes of plasma. The second compression mentioned by Tzeng is the plasma bubble because the occurring patterns are the same. When harder filtered is used, the first hot spot is observed near the anode

and moving away from anode. But some results also have shown that the hot spot are observed moving toward anode. Choi (Choi et al., 1989) also conclude that the first compression point varied along the axis correspond to gas condition.

2.6 After plasma bubble

After the plasma bubble occurred, Soh (Soh et al., 2004) has continue used laser shadowgraphic system to capture images. The images shown after plasma column break into hot spots, more than several keV electrons emitted and bombarding the anode and causing ablation of anode material. A very dense plasma cloud observed on the images, the ablation continues over 1 μ s. After the plasma bubble, when second pinch occur, second electron beam emitted and cause another ablation phase on the anode. The first ablation aided by second ablation lead to reduction in plasma cloud density and success view clearer on plasma cloud. Later, an explosion observed within the plasma cloud. The ablation plasma cloud continues expand upward collimated along the anode axis. The collimation is probably due to magnetic confinement because of azimuthal magnetic field induced by focus discharge current.

2.7 Rate of change of discharge current (dI/dt)

Later, Favre (Favre et al., 1998), Neog (Neog et al., 2008) and Talukdar (Talukdar et al., 2011) have used rate of change of discharge current signal (dI/dt) as reference signal instead of using discharge voltage signal. They found out first spike of dI/dt has appear near or coincided with first soft X-ray emission spike and electron beam spike; the first spike of dI/dt is the maximum compression. In addition, the hard X-ray is

detected after the maximum compression. The electron beam accelerated by the induced accelerating field in plasma column, the accelerating field proportional to dip of dI/dt , higher accelerating field, sharper dip of dI/dt , electron beam gains more energy. The results show that second region X-ray emission has coincided with second electron beam but is less intense compare to first electron beam. The second region X-ray emission also contained majority line emission emitted from hot spots.

2.8 Plasma Focus as X-rays Source

The X-ray emission from plasma focus can be divided into two main types (Favre et al., 1992; Ng et al., 1998; Rawat et al., 2004; Wong et al., 1996). First type is happening in first region where X-ray emission emitted from the plasma column and depends on the gas types used, typical are Argon, Neon and Krypton. Second type is occurring in second and third region where X-ray emission emitted due to electrons either bombardment on anode or interaction with vaporized anode material. Favre (Favre et al., 1992) found out that X-ray emission detected on axial direction above anode much higher than side on direction. However, the X-ray emission detected majority is similar to second region emission; and the first spike of the X-ray emission on axial direction detected 20 ns later than side on detector.

Ng (Ng et al., 1998) has divided operating gas pressure into three regimes based on time integrated X-ray film results. First regime has the lowest pressure range, both X-ray emission from hot spots and anode surface are weak. Second regime has the highest intensity of X-ray emission from anode surface. Third regime has the highest

pressure range, X-ray emission has higher intensity from hot spots and weaker intensity from anode surface. Kalaiselvi (Kalaiselvi et al., 2015) has obtained almost similar results with time resolve PIN diode detector. The results shown the hard X-ray has higher intensity at lower pressure and lower intensity at higher pressure; the soft X-ray is vice versa. This is because the electron density is lower at lower pressure; thus electron has more freedom of movement, accelerates to higher velocity and collides with anode to emit hard X-ray. The hard X-ray detected is either Bremsstrahlung radiation or excitation of outer electrons of the anode material. At high pressure, freedom of movement of electron is less, higher probability of energy transition to emit soft X-ray. The soft X-ray detected is line radiation from operating gas. Additional, time integrated X-ray images have been obtained by Tzeng and separated into two parts, lower and upper part (Tzeng et al., 1992). The upper part coincides to the second compression position which has weaker intensity than lower part.

Rafique (Rafique et al., 2010) reported majority emission from a disturbed current sheath is soft X-ray; a smooth current sheath produces high neutron yield and hard X-ray. Furthermore, the single compression produces high neutron yield and hard X-ray; the multiple compressions produces more soft X-ray. Afsharmanesh (Afsharmanesh & Habibi, 2013) stated that plasma temperature decrease after high radiation emitted, the gas between piston and shock front has colder thermodynamics, this lead to easier compression again for piston and shock front to form new hot spot.

Wong (Wong et al., 1996), Ng (Ng et al., 1998) and Asif (Asif & Xu, 2004) have used absorption curve to estimate the electron temperature by detect the X-ray emission with PIN diode detector. Intensity of the X-ray radiation through various thickness and materials is computed and plotted as the absorption curve. The absorption curve is based on multiple filters ratio method (Jahoda et al., 1960). Later Akel (Akel et al., 2013a, 2013b) has used non-local thermodynamic equilibrium model to compute the absorption curve.

2.9 Plasma Focus Modeling :Lee model

In the plasma focus model, Lee model considered the plasma focus dynamic in five distinct phases which are axial phase, radial inward shock phase, radial reflected shock phase, slow compression (Quiescent) or pinch phase and expanded column phase (Lee, 2014). The axial phase is the axial acceleration phase, the other four phases make up the radial compression phase. At the starting of radial compression phase (radial inward shock phase), the shock front and current sheath move into center. At the center axis, the shock front hits the axis and reflected back (radial reflected shock phase). After shock front reflected back, it hits with in coming current sheath (slow compression (Quiescent) or pinch phase). During the compression where the reflected shock hits the current sheath, this compression knows as maximum compression. Later, the current sheath compressed into plasma column and elongated on the axis of center anode (expanded column phase).

CHAPTER 3: EXPERIMENTAL SETUP

The experiments in this research were conducted with the United Nations University / International Centre for Theoretical Physics Plasma Fusion Facility (UNU/ICTP PFF). The system uses a capacitor of 30 μF with applied voltage of 15 kV which delivers a maximum energy of 3.3 kJ. Neon gas was used as the working gas throughout the experiment at 4 mbar. A unit of control system consists of a high voltage charger and triggering unit was setup. An array of pin diode detectors, multiple pinholes camera, X-ray spectrometer and microchannel plate (MCP) were setup for investigating the X-rays emission. A high speed ICCD camera was used to capture visible frame images. The schematic of the experimental setup is shown in Figure 3.1.

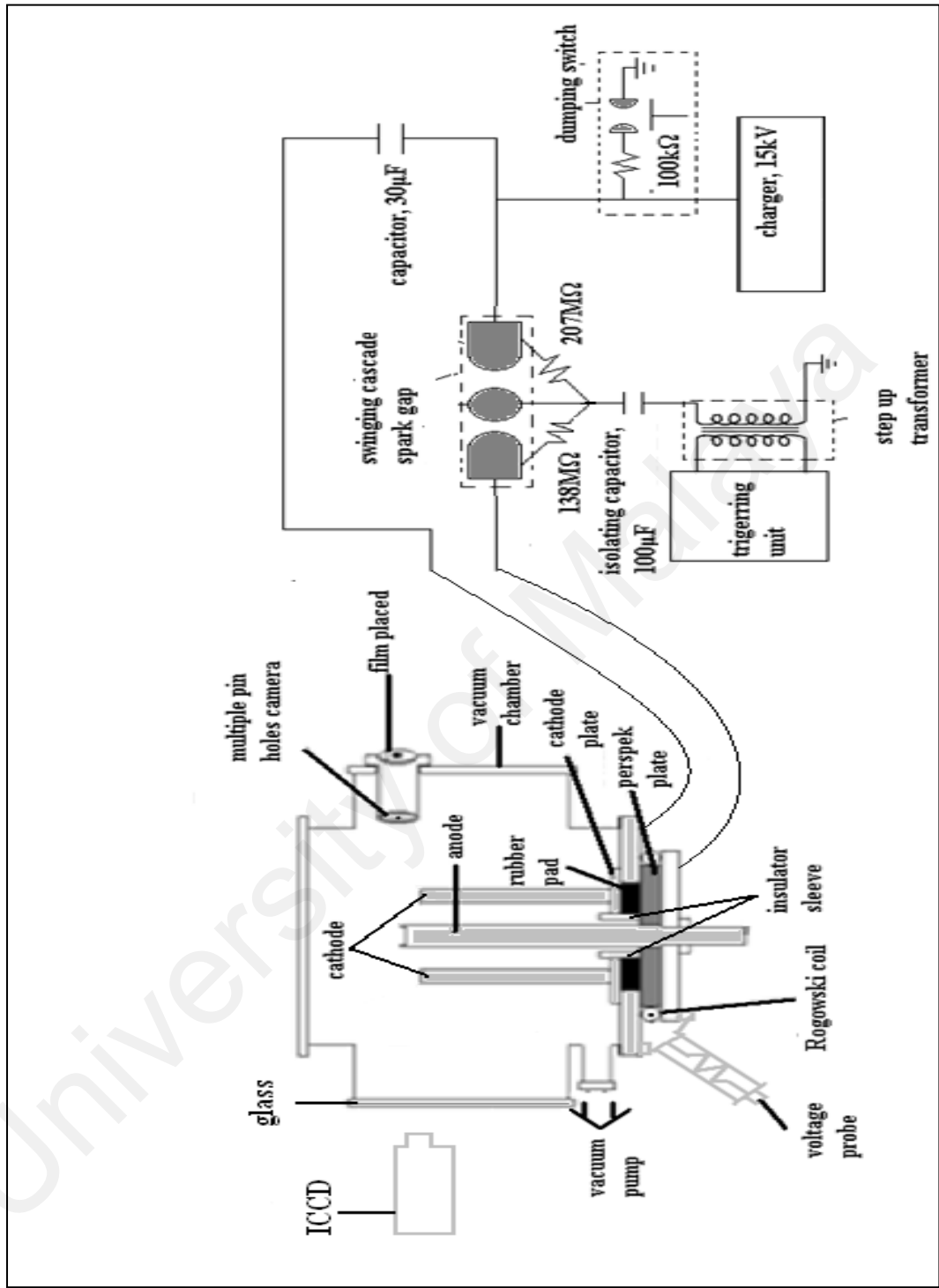


Figure 3.1(a): Schematic diagram of the experimental setup for side view.

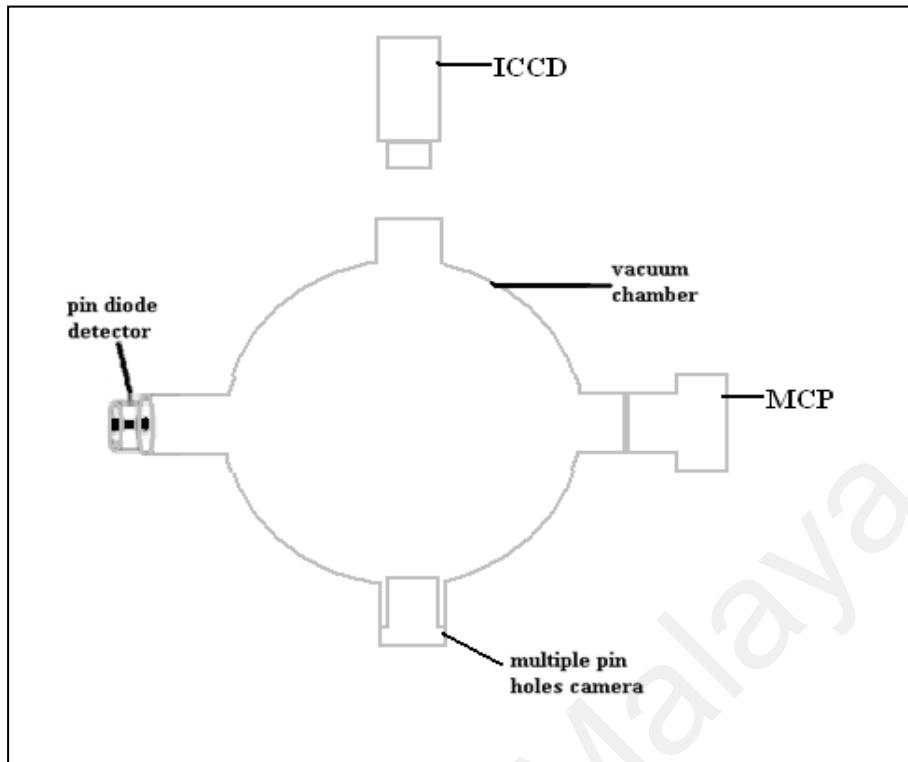


Figure 3.1(b): Schematic diagram of the experimental setup for top view.

3.1 Plasma Focus Facility

Plasma focus facility includes the plasma focus tube housed in a vacuum chamber, MCP chamber, the rotary pump, turbomolecular pump and pressure gauges, the capacitor and the high voltage charger, the spark gap, triggering unit and the dumping switch. The arrangement of the plasma focus facility is shown in Figure 3.2.

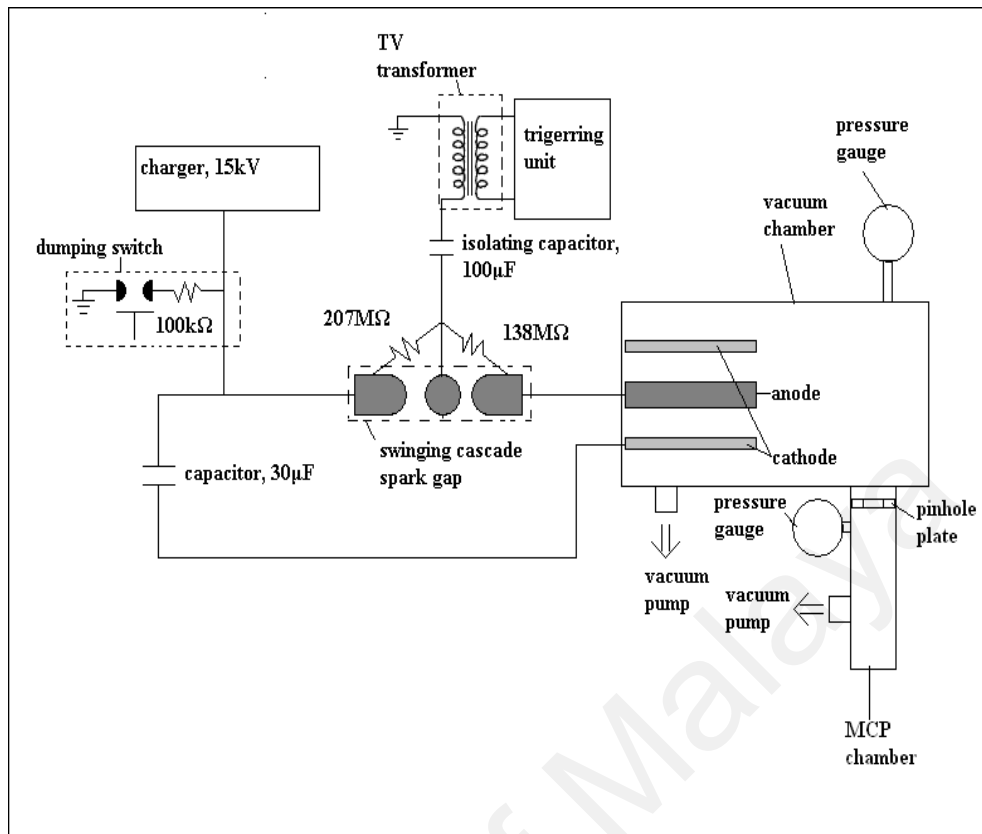


Figure 3.2: Plasma focus facilities schematic diagram.

3.1.1 Triggering Unit

The triggering unit is used to trigger a negative pulse to allow the breakdown of the spark gap switch which transfers the voltage from the capacitor to the plasma focus tube. The triggering unit is connected to a TV transformer, which has a step up ratio of 1: 27. The TV transformer is connected to an about 1 meter long isolating capacitor. The isolating capacitor is connected to swinging cascade spark gap. The ratio for the resistances of resistors which connected to the spark gap and the triggering rod is 3: 2 (207 MΩ: 138 MΩ).

3.1.2 Plasma Focus Tube

The plasma focus chamber is made from chromed brass connected to four ports and tested to vacuum of lower than 10^{-2} mbar. The vacuum pump used is BOC Edwards E2M2 rotary vane dual stage mechanical vacuum pump with pumping speed displacement of 1.5 cubic feet per minute at 60 Hz. Six 13 cm long cathode electrodes act as the outer electrodes will be setup around 14 cm central electrode (anode). The radius of the outer electrodes and anode is 3.2 cm and 0.95 cm, respectively. The geometrical arrangement of the anode and cathodes is shown in Figure 3.3. The electrodes are made from copper rods with the open end of the anode being engraved to 4 cm deep.

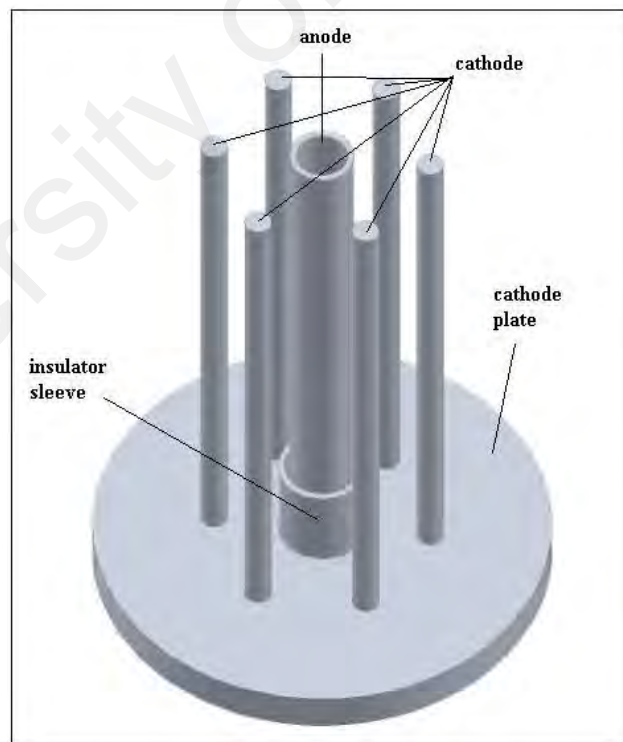


Figure 3.3: Geometrical arrangement of anode and cathode 3D schematic diagram.

3.1.3 Capacitor Bank and Spark Gap Switch

The capacitor bank is connected via a pair of swinging cascade spark gap switch, as shown in Figure 3.4. A single Maxwell capacitor with capacitance of 30 μF and charging voltage of 15 kV is used in this project. Swinging cascade spark gap switch is set with gap distance in the ratio 3:2 (4.5 mm: 3 mm) to switch the full voltage upon trigger. Smaller gap distance of 3 mm is placed in between the triggering rod and the focus tube (anode). The inductance of the spark gap is given as:

$$L = \frac{\mu_0 dl}{w} \quad (1)$$

where L is inductance, μ_0 is vacuum permeability, d is thickness of material, l is length of material which is parallel with current and w is width which is perpendicular with current.

The anode and cathode plate mounted on the capacitor are separated by multiple layers of Mylar and polyethene sheets. A Nylon cap is used as an extra insulation between the anode and the cathode.

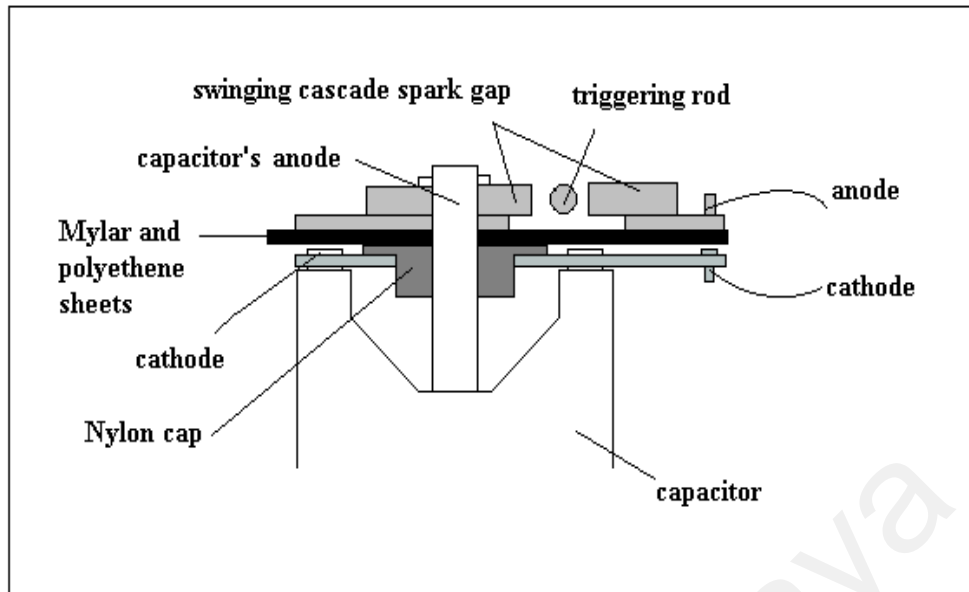


Figure 3.4: Capacitor and swinging cascade spark gap schematic diagram.

3.1.4 High Voltage Charger

The high voltage charger used is TECHNIX CCR20-P-600 model, a fast capacitor charger for the purpose of charging a capacitor for pulsed discharge experiment. The charger is connected to a dumping switch, spark gap and capacitor as shown in Figure 3.5. The dumping switch acts as a grounding switch. When dumping switch is on (open circuit) and high voltage charger is switched on, the charging voltage bypasses the dumping switch and charge up the capacitor. When dumping switch is off (closed circuit) and high voltage charger is switched off, the voltage from the capacitor will flow back through the dumping switch to the ground point. The resistor of high resistance (100 k Ω) and high power rating is used to slow down the rate of current dump to the ground for safety reason.

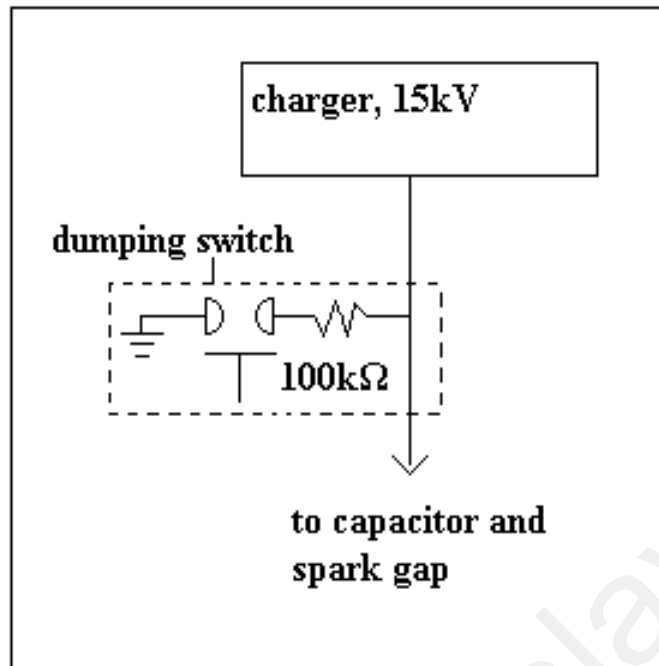


Figure 3.5: Charger and dumping switch schematic diagram.

3.1.5 MCP chamber

A MCP chamber is employed and it has been tested for vacuum down to about 10^{-5} mbar. The vacuum pump used is BOC Edwards EXT75DX ISO63 turbomolecular pump and BOC Edwards RV3 rotary vane dual stage mechanical vacuum pump with pumping speed displacement of 90000 revolution per minutes and 2.3 cubic feet per minute at 60 Hz respectively. A four 0.1 μm pinholes plate is placed between MCP chamber and plasma focus chamber for imaging purpose. Another 15 μm Mylar sheet covers the four pinholes to separate pressure different between two chambers.

3.2 Diagnostic Tools

Several diagnostic techniques are developed and used to analyze the pinched plasma and X-ray emission emitted from the pinch plasma focus simultaneously. These include an array of pin diode detectors, a multiple pinholes camera, X-ray spectrometer, MCP and ICCD camera.

3.2.1 Array of PIN Diode Detectors

The array of PIN diode detectors employed five channels of BPX65 PIN diodes, each couple to different filters. The PIN diodes are all negatively biased. The biasing circuit is shown in Figure 3.6 and the arrangement of the PIN diodes array is shown in Figure 3.7.

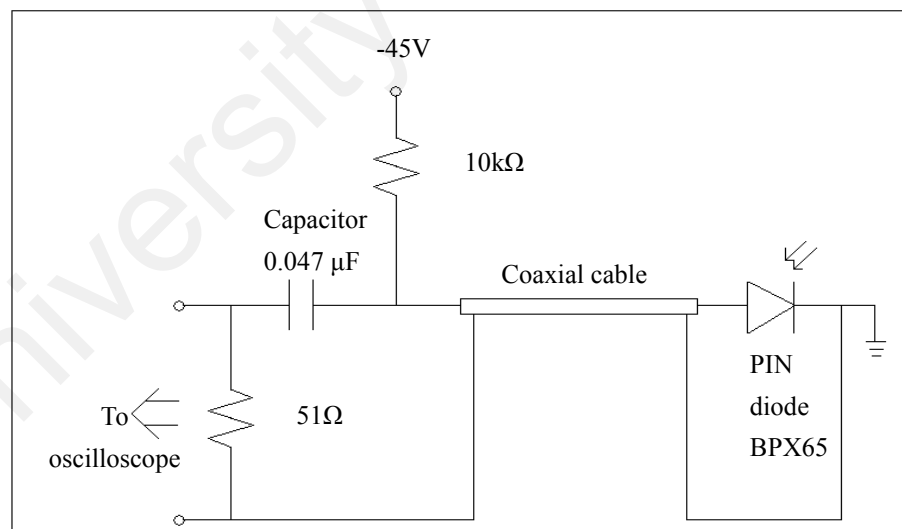


Figure 3.6: Schematic showing a set of PIN diode detector and the biasing circuit.

The five channels of PIN diodes array are made by using BPX65 pin diodes (channel 1, channel 2, channel 3, channel 4 and channel 5), all with their glass windows removed, and covered with a 30 μm aluminium foil to shield the visible

light. The spectral range of pin diode sensitivity is from 350 nm to 1100 nm with the glass window, and can be extended to shorter wavelength with the glass window removed. Additional filters of 20 μm , 30 μm and 40 μm aluminum foil are added to channel 4, channel 3 and channel 2 respectively. Another additional 10 μm copper foil is added to channel 1. The PIN diodes are negatively biased at 45 V.

The sensitivities of the detectors coupled with the different filters are shown in Figure 3.8. The double-foil technique calculates the electron temperature of the plasma by taking the ratio of the X-rays signals through the two different filters. By taking the ratio of the X-rays signals of the pairs of filters with different thickness, the graphs corresponding to electron temperature of 500 eV to 10 keV are shown in Figure 3.9 (absorption curve). In the case of line radiation, the ratio is a straight line.

In the calculation of the theoretical absorption curve, most of the X-ray emission is Bremsstrahlung radiation, thus Bremsstrahlung X-ray intensity from 500 eV to 10 keV was obtained through FLYCHK simulation (Chung et al., 2005). The ratio method is calculated as following formula (Akel et al., 2013b; Kwek, 1989):

Attenuated X-ray emission through BPX65 PIN diode and filters is given as:

$$I = \int P(\lambda, T_e) \cdot S(\lambda) \cdot \exp(-\mu_f(\lambda) \cdot \rho_f \cdot x_f) d\lambda \quad (2)$$

Finally, the ratio R is given as:

$$\begin{aligned}
 R &= \frac{\text{emission through additional Al foil}}{\text{emission through 30 } \mu\text{m Al foil}} \\
 &= \frac{I_{Al+}}{I_{Al}} \\
 &= \frac{\int P(\lambda, T_e) \cdot S(\lambda) \cdot \exp(-\mu_{Al}(\lambda) \cdot \rho_{Al} \cdot x_{Al+} - \mu_{Al+}(\lambda) \cdot \rho_{Al+} \cdot x_{Al+}) d\lambda}{\int P(\lambda, T_e) \cdot S(\lambda) \cdot \exp(-\mu_{Al}(\lambda) \cdot \rho_{Al} \cdot x_{Al}) d\lambda} \quad (3)
 \end{aligned}$$

where $P(\lambda, T_e)$ is X-ray intensity corresponding to wavelength and electron temperature

$S(\lambda)$ is sensitivity of BPX65 PIN diode

$\mu_f(\lambda)$ is coefficient of filter material (cm^2/g)

ρ_f is density of filter material (g/cm^3)

x_f is thickness of filter material (cm)

Al is 30 μm aluminium foil

Al+ is additional aluminium foil (20 m, 30 μm or 40 μm)

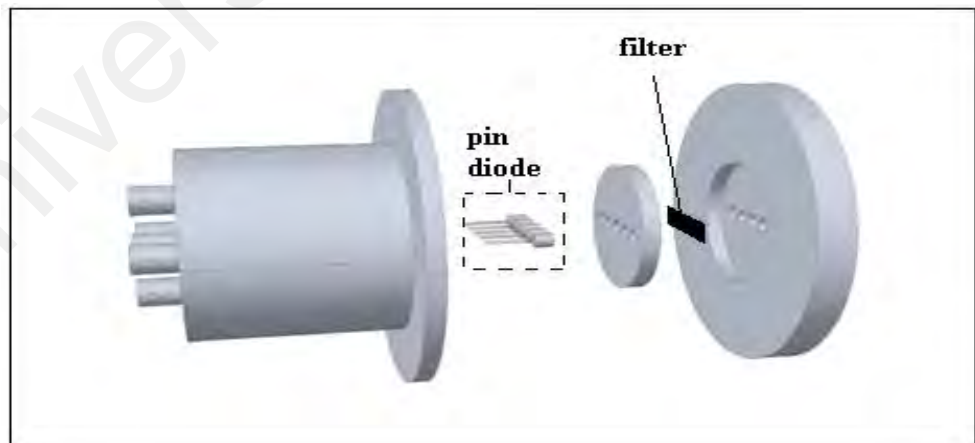


Figure 3.7: Array of pin diode detectors 3D schematic diagram.

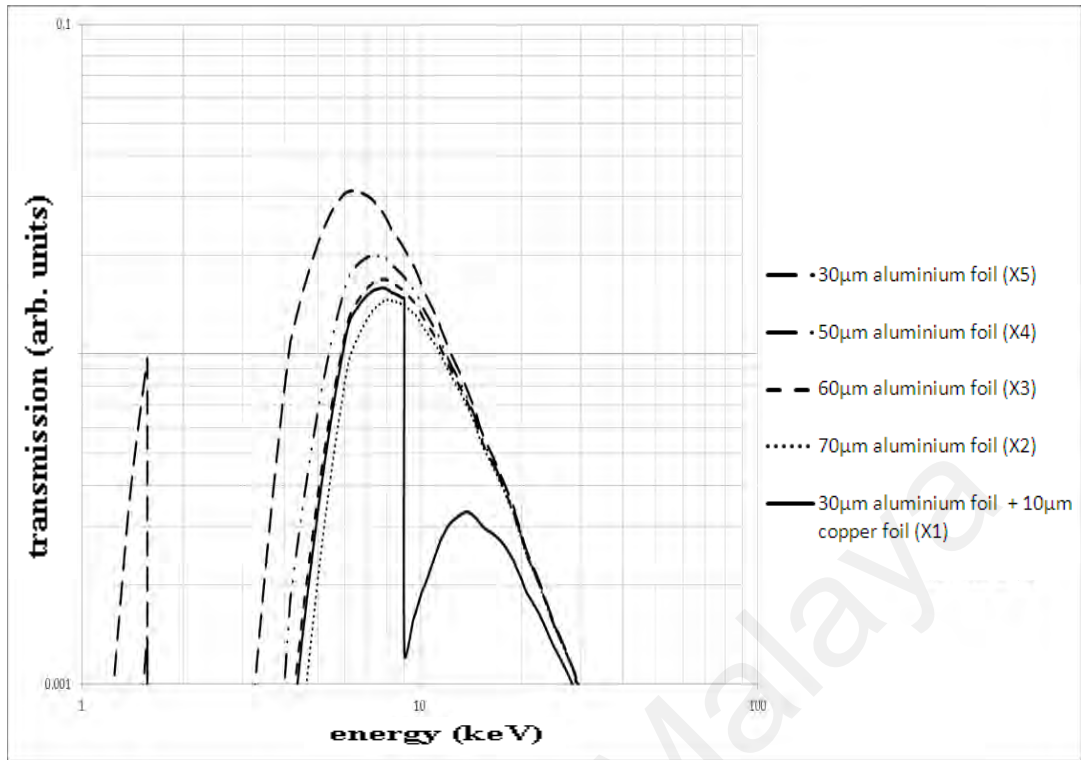


Figure 3.8: Sensitivity curve for different filter thickness.

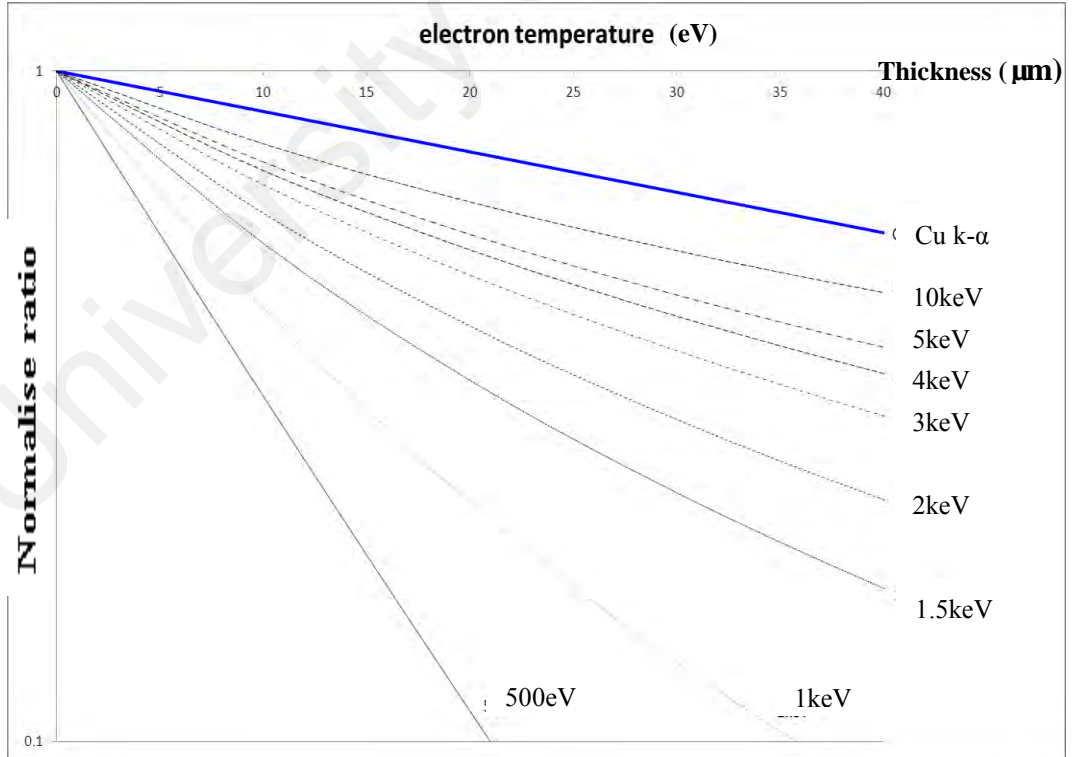


Figure 3.9: Graph of ratio versus aluminum foil thickness at different plasma electron temperature.

3.2.2 Multiple Pinholes Camera

Figure 3.10 represents the 3D schematic diagram for multiple pinholes camera. Multiple pinholes camera was setup by six 100 μm pinholes of different filters. The pinholes are covered by 30 μm Al foil, 50 μm Al foil, 60 μm Al foil and 30 μm Al foil + 10 μm Cu foil respectively. The last two pinholes are covered by 11.5 μm aluminized Mylar. Another sheet of 25 μm Mylar is added in between the pinhole camera and film holder for vacuum purpose. The 100 μm pinhole is positioned at the center and the rest are positioned at radial distance of 1 cm from the center pinhole (pinholes plate). The distances from centre of anode to pinholes and from pinholes to the films are (18.35 ± 0.01) cm and (6.65 ± 0.01) cm, respectively. Multiple pinholes were used in order to observe different energy of the X-rays images and the hot spots.

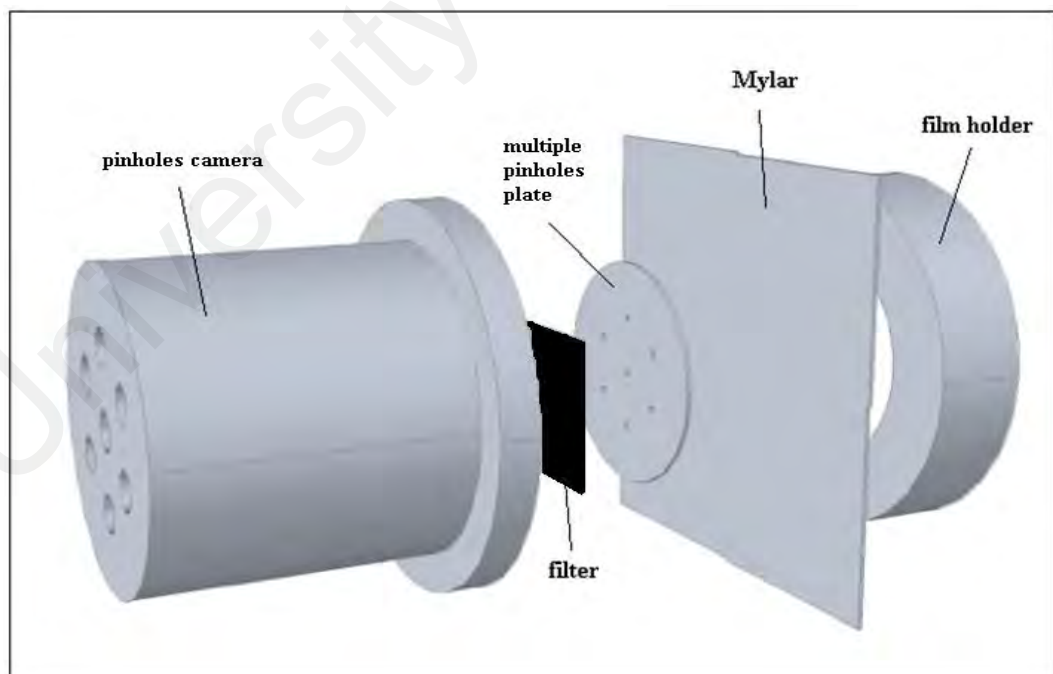


Figure 3.10: Multiple pinholes camera 3D schematic diagram.

The imaging of pinhole on the film is shown in Figure 3.11. The distance from pinched plasma focus (object) to X-ray film (image) is fixed. As seen in the Figure 3.11, the size of the hot spot (object) can be calculated. The equation to calculate the size of the hot spot or pinched plasma column is given as:

$$\text{for } x < p, x = \left(\frac{L_o(q-p)}{L_1} \right) - p \quad (4)$$

$$\text{for } x > p, x = \left(\frac{L_o}{L_1} \right) q \quad (5)$$

where x is the pinched plasma focus, p is pinhole size, q is image size, L_o is distance between the pinched plasma and pinhole, L_1 is distance between the pinhole and image.

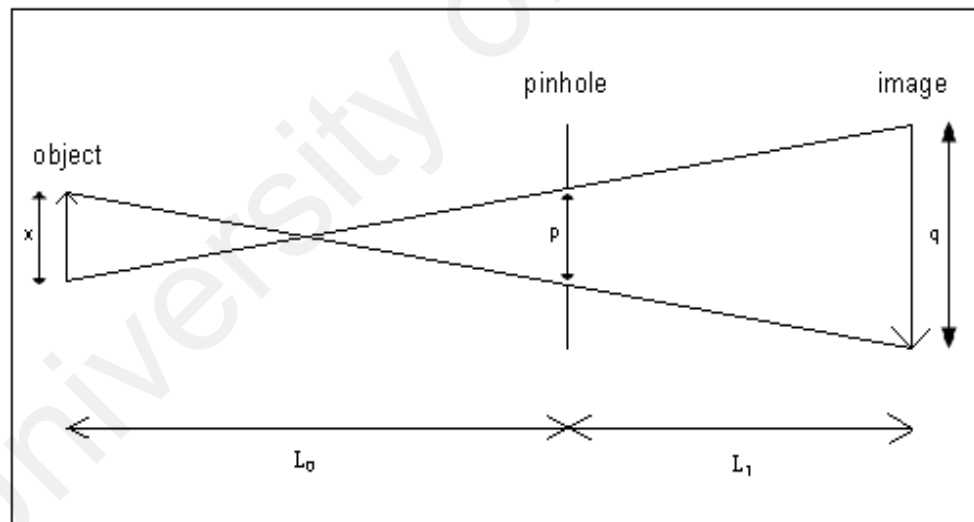


Figure 3.11: Pinholes' image resolution where x is pinched plasma size (object size), p is pinhole size, q is image size, L_o is distance between pinched plasma and pinhole, L_1 is distance between pinhole and image.

3.2.3 Rogowski Coil / Magnetic Probe

Rogowski coil is used to measure the discharge current of the system. Upon a discharge, high current is passing through the anode and the center of the Rogowski coil. Thus, a magnetic field is induced by the current and threads through the minor cross section of the Rogowski coil. This will induced a voltage across the terminals of the coil which can be measured across a small resistance, r connected as shown in Figure 3.12. The r is used as a current transformer and the induced voltage recorded by the oscilloscope is proportional to current.

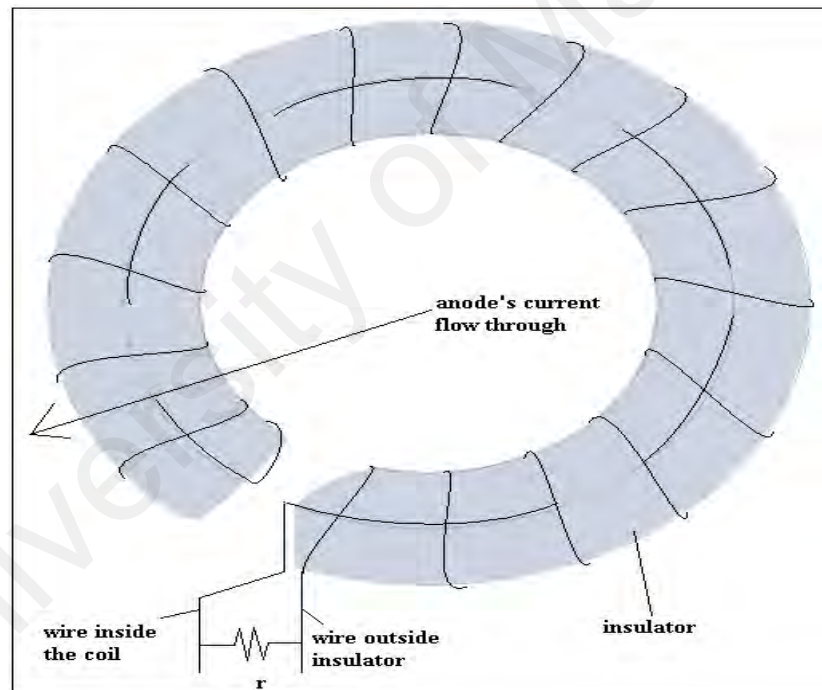


Figure 3.12: Rogowski coil schematic diagram.

In order to determine the absolute current flowing through the Rogowski coil, it needs to be calibrated. This is done at the discharge in high pressure to simulate a complete LCR circuit, where the peak current measured is determined. With the coil

working in the transformer mode, the current is registered by the digital oscilloscope in term of voltage.

To calibrate the Rogowski coil, the peak current (first current peak) is given by:

$$I_1 = \frac{\pi C_o V_o (1+f)}{T} \quad (6)$$

where $C_o = 30 \mu\text{F}$ is the capacitance of the capacitor we used, and the voltage applied is $V_o = 14.7 \text{ kV}$, $T =$ periodic time (average period for three cycles), $f =$ reversal ratio (Lee, 1984) (Figure 3.13) is given as:

$$\frac{V_2}{V_1} = \frac{1}{4} \left(\frac{V_5}{V_4} + \frac{V_4}{V_3} + \frac{V_3}{V_2} + \frac{V_2}{V_1} \right) \quad (7)$$

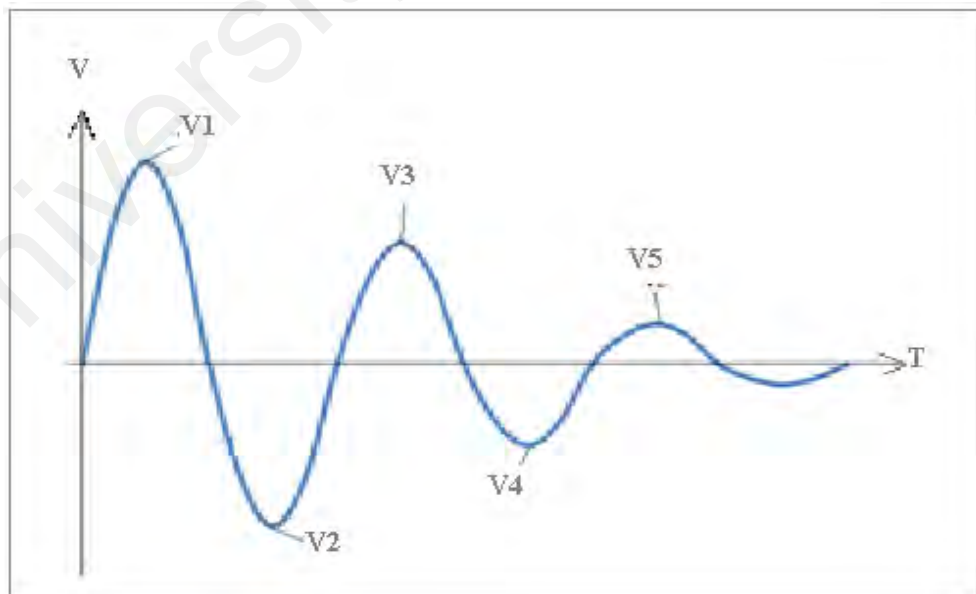


Figure 3.13: Reversal ratio (peak voltage from first to fifth).

The ratio of the current I_1 to V_1 is the calibration factor, $K_I = \frac{I_1}{V_1} A/V$ for the Rogowski coil. The process has been repeated to minimize error in measurements. The calibration factor K is used to give the value of discharge current in all the measurements. The current I_1 is the maximum current.

The magnetic probe is used to measure rate of change of the discharge current. The magnetic probe is almost similar concept with the Rogowski coil but without the current transformer, r and has number of turns of five to ten turns only.

3.2.4 Voltage Probe

The voltage probe has the multiplication factor of 101. The resistors are connected as shown in Figure 3.14. The insulator is used to avoid the ten 510Ω resistors chain in contact with the ground or cathode. The output voltage can be obtained by using voltage divider method (Figure 3.15).

$$\frac{V_o}{V_i} = \frac{R_2}{R_1 + R_2} = \frac{51\Omega}{510\Omega \times 10 + 51\Omega} = \frac{1}{101} \quad (8)$$

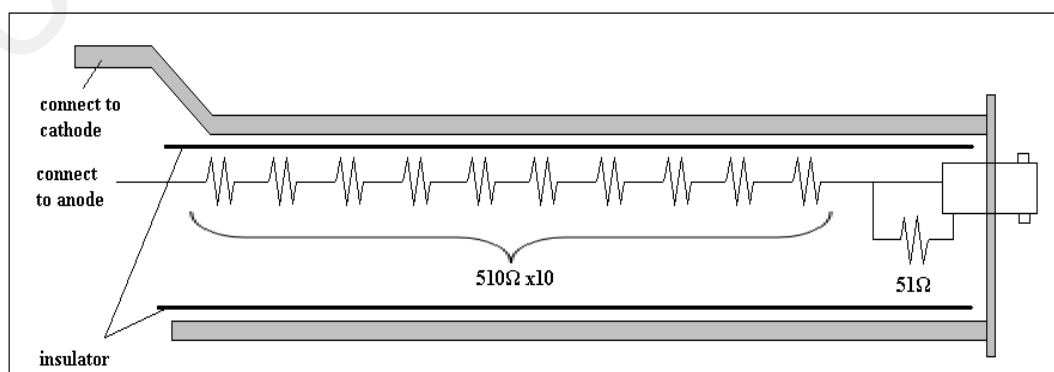


Figure 3.14: Voltage probe schematic diagram.

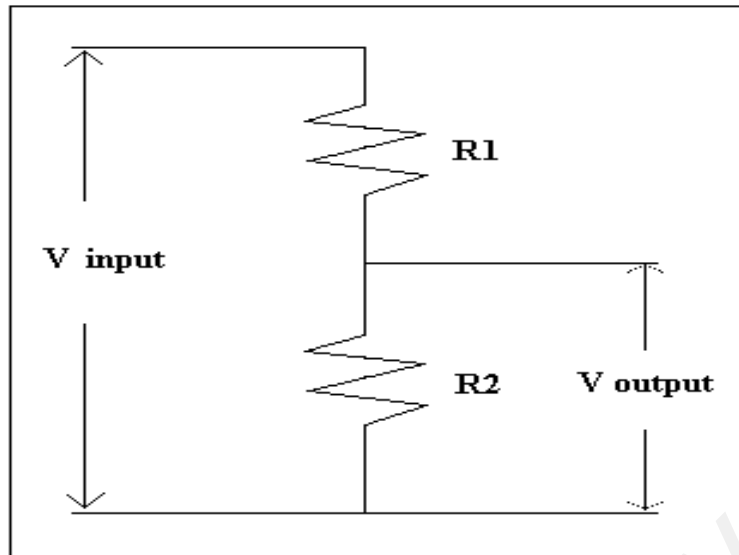


Figure 3.15: Voltage divider principal schematic diagram.

3.2.5 X-ray Spectrometer (XR-100 CR)

The schematic arrangement of X-ray spectrometer setup is shown in Figure 3.16. The Amptek program is used to record the data obtained from the spectrometer. 1024 channels are chosen with calibration factor for channel 327 equivalent to 13.95 keV and channel 416 equivalent to 17.74 keV. The spectrometer is mounted at the right angle above the anode. The sensitivity range for X-ray spectrometer is from 0.02 keV to 43.59 keV.

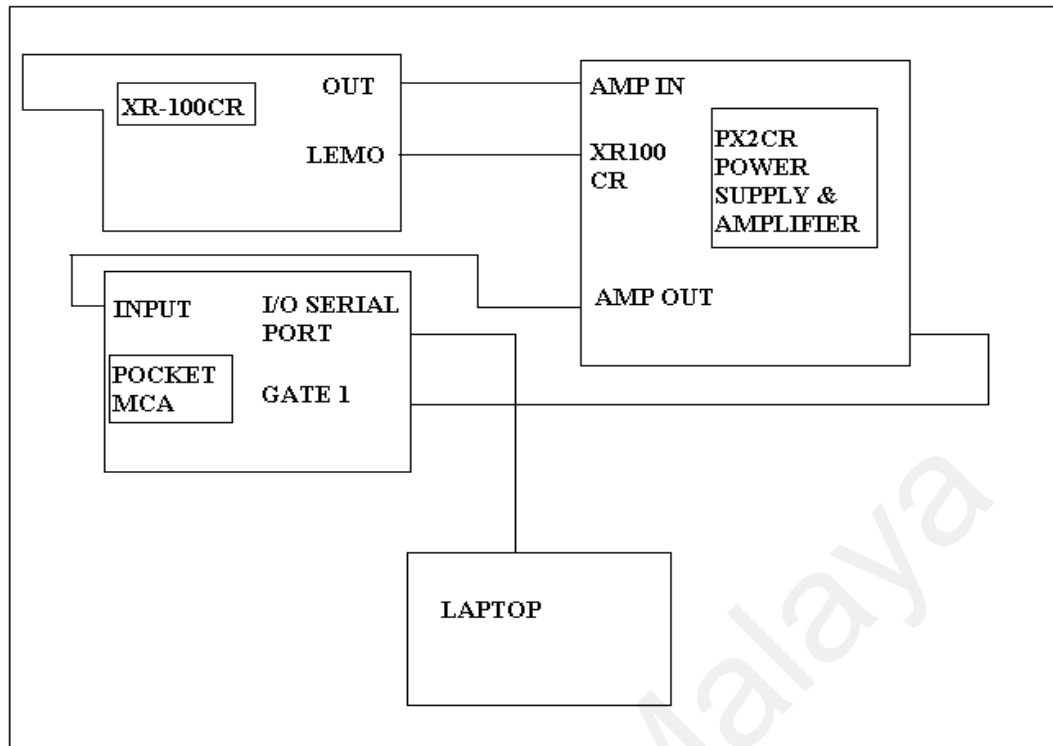


Figure 3.16: X-ray spectrometer schematic diagram.

3.2.6 Microchannel Plate (MCP)

A four channels MCP (Figure 3.17(a)) is set up by using the LSP-MCP/2S-D56 type with gating pulse generator capable of 5 ns, 10 ns or 20 ns open shutter time at a voltage supplied of 6 kV (Figure 3.17(b)). A 0.1 μm gold layer is coated on the MCP (Figure 3.18). Different coaxial cable lengths are used to provide delays between channels. Upon X-ray irradiation, secondary electrons emitted multiplies within the MCP wall as shown in Figure 3.19. When the electrons hit the phosphor screen, the phosphor screen shows visible image. A D3 camera with AF-S Micro NIKKOR 60 mm lens is used to capture the visible images on the phosphor screen.



Figure 3.17 (a): Microchannel plate and pulse generator for MCP.



Figure 3.17 (b): Microchannel plate and pulse generator for pulse generator.

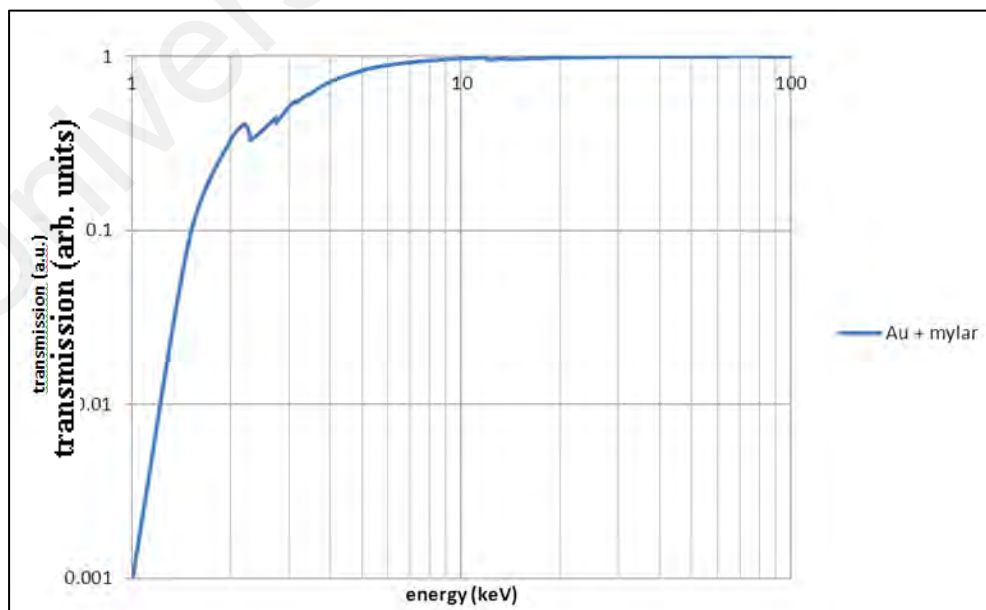


Figure 3.18: Sensitivity curve for gold foil + mylar.

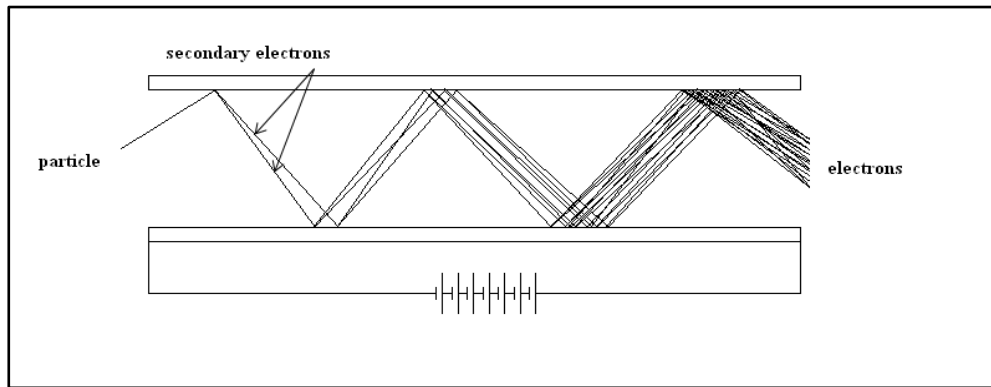


Figure 3.19: MCP process.

3.2.7 ICCD camera

The high speed camera used is ICCD PI-MAX3 with TAMRON micro lens SP 90mm F/2.8. The ICCD is used to image visible frame images during radial compression phase. The ICCD can provide the smallest open shutter time is 2.81 ns. In this experiment, the ICCD open shutter time is 5 ns.

3.2.8 X-rays Film Processing

The X-rays film is used in pinhole imaging. The film used is BioMax MS film which has high sensitivity and shortest exposure time. Solution of the developer and fixer are prepared for film processing according to the manual for the X-rays film. The X-ray film exposed in experiments will be developed in the dark room. The X-rays films are dipped into developer first for ten minutes. Next, the X-rays films are flushed with clean water to remove the chemicals. Then, the X-rays films are dipped into fixer for five minutes. Finally, the X-rays films are flushed with clean water and allowed to dry. The images produced on the film are reviewed.

CHAPTER 4: RESULT AND DISCUSSION

4.1 Introduction

In this report, the plasma dynamics leading to the formation of the pinch in the plasma focus discharges is investigated by employing the seven diagnostics techniques simultaneously. The implementation of the measurement techniques and their time correlation are crucial and has been carried out carefully. The diagnostics tools with reference to the discharge chamber are shown in Figure 3.1. The discharge is operated with neon gas at pressure of 4 mbar. Electrical signals are shown in Figure 4.1, they are discharge voltage (V), rate of change of discharge current (di/dt), X-ray signals from PIN diode detectors (X5 to X1), MCP (MCP1 to MCP4) and ICCD exposure time to give precise correlation to the images obtained from ICCD camera and MCP and X-ray films imaging. Based on Figure 4.1, the first region is around 2.225 μs to 3.275 μs , the second region is around 3.425 μs to 3.475 μs and the third region is around 3.6 μs to 3.65 μs .

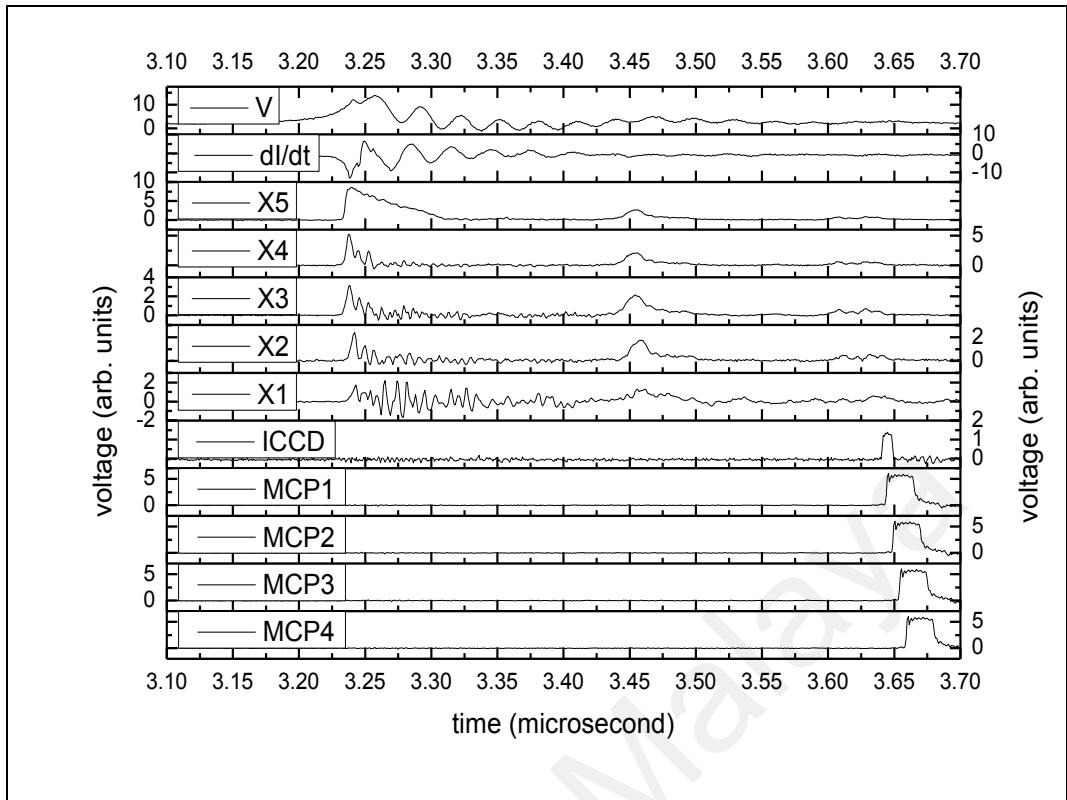


Figure 4.1: Typical results of high voltage probe, magnetic probe, array of PIN diode detectors, ICCD and MCP.

MCP's exposure times are either 5 ns or 20 ns, which are also shown in the graph. Ideally we wish to sync the time resolved MCP images with the ICCD image, and resolve the hot plasma with X-ray emission into the four gated frames of the MCP. This is done by sending precise trigger pulses to the devices. However jitter in the triggering pulses is often larger than the duration of the ICCD's windows thus the MCP channel's exposure time could hardly fall on the same time with ICCD's exposure time.

X-ray images are captured from MCP and by X-ray film via the pinhole camera. The images from both MCP and X-ray films are presented when both diagnostics X-ray emission are detected, particularly during the pinch when the plasma is hot. In the

case that MCP registers not X-ray images, results are shown with only X-ray images obtained from pinhole camera. The X-ray images on the developed X-ray film are scanned with high resolution negative scanner. The X-ray film used has low sensitivity in the range of soft X-ray thus weak or no images are registered with filters of 30 μm Al foil, 50 μm Al foil, 60 μm Al foil and 30 μm Al foil + 10 μm Cu foil. The results shown here are the X-ray images detected with pinhole camera covered with 11.5 μm Aluminized Mylar.

4.2 Results and Analysis

A complete set of results with reference to the ICCD images cover a duration of 850 ns from 200 ns before the pinch. The results are arranged in sequence, where first set of results consist of the ICCD image at 200 ns before pinch, while there was no X-ray signal registered on MCP. These are presented in Figure 4.2.

Figure 4.2(a) shown the axial acceleration phase; Figure 4.2(b) shown the end of axial acceleration phase and at the point of beginning of the radial compression phase and the implosion of current sheath from the outer edge of anode have been shown clearly in Figure 4.2(c) to Figure 4.2(h). The complete radial compression phases are revealed by studying the results as in Figure 4.3 first region pinch, Figure 4.4 second region pinch and Figure 4.5 on anode.

In Figure 4.2(c), dimly lit area is the current sheath, the center dark rod is the anode electrode and the dark background is the chamber wall. At this moment, the current sheath begin to move toward center axis of the anode, and as it moves toward the center axis, its intensity increases as shown in Figure 4.2(d), Figure 4.2(e), Figure 4.2(f), Figure 4.2(g) and Figure 4.2(h).

During the current sheath implosion at the end of the electrodes, voltage spikes and sharp drop in current signals are observed. The evolution of plasma pinch observed by MPC and pinhole camera are presented in Figure 4.3. In Figure 4.3(a) and Figure 4.3(b) the images shown current sheath distortion due to the Rayleigh-Taylor instability (Rafique et al., 2010). As shown in Figure 4.3(a), X-ray emission registered by MCP's channel 3 and 4 at time close to the sharp drop or peak of dI/dt . The channel 3 and 4's exposure time correspond to time just after the first peak of the dI/dt and another small peak after the first peak of dI/dt respectively (arrow show the peak of dI/dt in Figure 4.3(a)). The channel 3's exposure time covers first peak of discharge voltage (arrow shows the peaks of discharge voltage in Figure 4.3(a)). This indicates that the X-ray emission is emitted from an elongated plasma column and the column breaks into hot spots as shown in the images of channel 3 and 4 respectively. Peak 1 of the X-ray signals as in X5 signal are calculated through ratio method and the neon electron temperature estimated as around 10 keV. The results of electron temperature of peak 1 is plotted in Figure 4.6(a). Due to different thickness and sensitivity of aluminum filters, the electron temperature at first region pinch where various range of X-ray energy have been detected could not be obtained accurately. This is because electron

temperature curve is plotted based on area under the curve comprising all the emission as shown in Figure 3.8 and channel 4 PIN diode detector has a larger range of detection compared to channel 2.

Figure 4.3(b) shows that the current sheath begins to compress to center to form plasma column where a sharp drop in dI/dt signal is detected. X-ray emission has been registered during or approximate to the sharp drop or peak of dI/dt . ICCD's exposure time falls on the sharp drop of dI/dt and before first peak of discharge voltage. The intensity of the compressed current sheath near the center axis of the anode increases dramatically compared to previous ICCD's images. The four channels MCP shows the evolution of the current sheath: compressed into plasma column at channel 1, elongated at channel 2; broke into hot spots at channel 3 and formed second compression at channel 4. Note the time of channels 1 and 4 indicating the first and second compression correspond to the first and second peaks of discharge voltage respectively (arrows show the peak of discharge voltage in Figure 4.3(b)). The time when channel 2 and 3 registered plasma column elongated and hot spots correspond with the peak of discharge voltage and dI/dt respectively (arrows show the peak of discharge voltage and dI/dt in Figure 4.3(b)).

Figure 4.3(c) shows MCP images with exposure time of 20 ns, where the formation of plasma column and hot spots are not clear due to the long exposure. But these images showed the development of kink instabilities in the plasma column (Lee, 2014; Rafique et al., 2010). ICCD's exposure time covered first peak of dI/dt and before first

peak of discharge voltage (Note the arrow in Figure 4.3(c)). The ICCD's image showed that current sheath in the first compression and X-ray emission was observed.

In Figure 4.3(d), ICCD image showed current sheath compressed and elongated, with the exposure during the peak of di/dt and discharge voltage (arrow. MCP channel 1 opened at the same time with the ICCD's exposure time and X-ray emission has been registered. MCP's channel 2 and 3 subsequently showed hot spots and second compression. The channel 2's exposure time fall on a slope where failed to observe a peak of di/dt may due to insensitivity of magnetic probe (second arrow in di/dt Figure 4.3(d)). Second compression observed on channel 3 was registered before second peak of discharge voltage. The channel 4's exposure time falls on another peak of di/dt (last arrow in di/dt), dim hot spots like are observed on the MCP, another X-ray PIN diode peak is detected. By measuring the plasma temperature with ratio method (peak 1 and 2 in X5 Figure 4.3(d)), around 1.0 keV is calculated as shown in Figure 4.6(b) (peak 2). According to Figure 3.18, MCP is not sensitive to 1.5 keV and below compare to higher energy range. This means that there is a second compression of current sheath is continue but the energy is reduced because most energy is used in first compression of current sheath. Hence, the electron temperature at peak 2 is lower than the electron temperature at peak 1 (similar to Figure 4.6(a) peak 2).

It is observed in the first region, X-ray emission is mainly from neon emission with small amount of copper K-alpha emission. The emission due to copper K-alpha was detected by the PIN diode X1 (copper filter) at 1 ns later compared to X2, as shown in

Figure 4.7. The small delay of 1 ns has been confirmed as the same was observed when the PIN diodes and the connections were swapped.

Referring to Figure 4.3(e), the ICCD camera captured the image at the time after the peak of dI/dt , when the current sheath was dim thus not no emission registered near the anode surface. This indicates that the current sheath from the anode surface has move onto axis following the compression. The peak of the dI/dt signal showed the time at the maximum compression of the plasma column, at a moment before this image was captured. The 4 images registered by MCP include the duration during the maximum compression and after compression. Time of exposure of MCP's channel 1 is during the peak of dI/dt (arrow bar in dI/dt), it registered a very dim hot spot correlated to the plasma column breakup from the first compression (black arrow in MCP channel 1). MCP's channel 2's image shows several hot spots with less intensities, where this is similar to the image in Figure 4.3(d) registered by MCP's channel 4 when the plasma energy has reduced after first compression.

After the plasma column breaks up, several dense hot spots are usually formed due to instabilities. This is clearly shown in Figure 4.3(f) (ICCD's image: near the anode surface, bottom black arrow). In the same figure, second compression has also been observed, as indicated by the upper arrow. Is it believed that there is low intensity X-ray during the opening time of MCP's channel 1 that none has been registered. After the second compression, the MCP's channel 2 where the exposure time was during the small peak of dI/dt (arrow); the energy of X-ray emission increased and hot spots were

observed. However the PIN diode detectors did not record high X-ray signals. This could be because the emission was of softer wavelengths and below the sensitivity range of the detectors.

An ICCD image registered at the exposure time right at the peak of the dI/dt signal showed interesting features during the maximum compression. The image consists of a dim area near the anode and an intense bright area at higher position as in Figure 4.3(g). The intense bright area corresponds to second compression while the dim area indicates decaying hot spots including the necking area.

After current sheath compression, instabilities cause the plasma column to break up and forms hot spots. These hot spots continue to compress further before they decay. Intense hot spots are often observed after maximum compression. The formation of intense spots with low or no X-ray emissions have been registered at further distance from the anode surface as shown in Figure 4.3(h) to Figure 4.3(j). At this time, another peak signal was observed in the dip of dI/dt (indicated by arrow in the Figure 4.3(h) to Figure 4.3(j)) and the PIN diode X5 registered a broad signal. There was no image registered by the MCP. This can be explained as the emission has been lower or the energy of the X-ray was lower, which is consistent with the measurements shown in the PIN diode X4 with filter of 60 μm Aluminum foil.

The dynamics towards the end of the pinch evolution has often been neglected, but it is also important as the picture helps to build better understanding of the phenomenon. In Figure 4.3(h) to Figure 4.5(c), the ICCD images are recorded for a duration of 5 ns. They clearly shown a layer of glow (visible wavelengths) on top of the anode. This layer is believed to be due to ablation of the anode surface by to electron bombardment (Soh et al., 2004). It is observed that during the sharp drop of dI/dt , some intense activities take place on the top of the anode where several black spots have been registered and indicated in the Figure 4.8(b). The sequence of images shown that the activities on the anode surface continued and formed a layer of visible emission. Ablation of anode surface due to electron beam activities occurred randomly during the sharp drop in dI/dt signals. At this moment, voltage spikes indicating pinching action, while electron beams are accelerated toward the anode and their bombardment on the anode produces the visible emissions.

The remaining plasma compressed and pushed forward to reach to the top of the current sheath. This was followed by decay of intense spots, where they induced a shock wave as shown in Figure 4.3(j). The induced shock wave moved outward and forms a bubble like structure, which is labeled as plasma bubble in Figure 4.3(j). Some of the shots also shown more than one intense spot on top of the current sheath. This plasma bubble will continue to expand outward by the induced shock wave as shown in Figure 4.3(k). The expansion of plasma bubble is observed during the second region pinch. Several images showing the plasma bubble evolution are shown in Figure 4.4. First, Figure 4.4(a) shows the plasma bubble expanded outward. As the bubble

expanded outward, another pinch like formation is registered inside the bubble (Figure 4.4(b)). However, note that the ICCD timing covered the duration during the peak of dI/dt signal and the discharge voltage therefore missed the event occurred at later time. In Figure 4.4(c), the ablation of anode is continuing. The evolution of the pinch like structure inside the plasma bubble is unknown. Reasonable explanation is given based on the existing understanding; ablation of anode material due to electron beam created a “virtual anode” above anode consisting of copper vapor, due to azimuthally magnetic field (Soh et al., 2004). The compression of the current layer or “current sheath” (the electrons and ions in plasma bubble) resulted and this occurred inside the plasma bubble. Based on X-ray emission measurements, analyzed using ratio method, the emission from the second region is dominated by copper K-alpha. The X-ray image’s result is shown in Figure 4.9. MCP’s image showed that the X-ray emission was originated from a spot at around 4.93 mm above the anode while the plasma bubble was registered at around 12.47 mm above the anode. This is because the pinch inside the plasma bubble emits electrons and these electrons bombard with copper vapour and X-ray emitted. The emission could be due to heated copper plasma, copper plasma also observed in other devices, copper plasma also observed in other devices (Soh et al., 2004; Wong et al., 1996).

The process of pinching, electron beam ablation and heating of anode material continue while the energy was still sufficient to drive the “current sheath”; in some cases third region pinch action was registered. Results showing the plasma dynamics related to third region pinch are as shown in Figure 4.5. Figure 4.5(a), Figure 4.5(b)

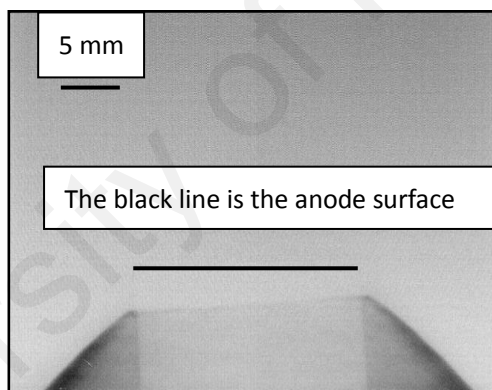
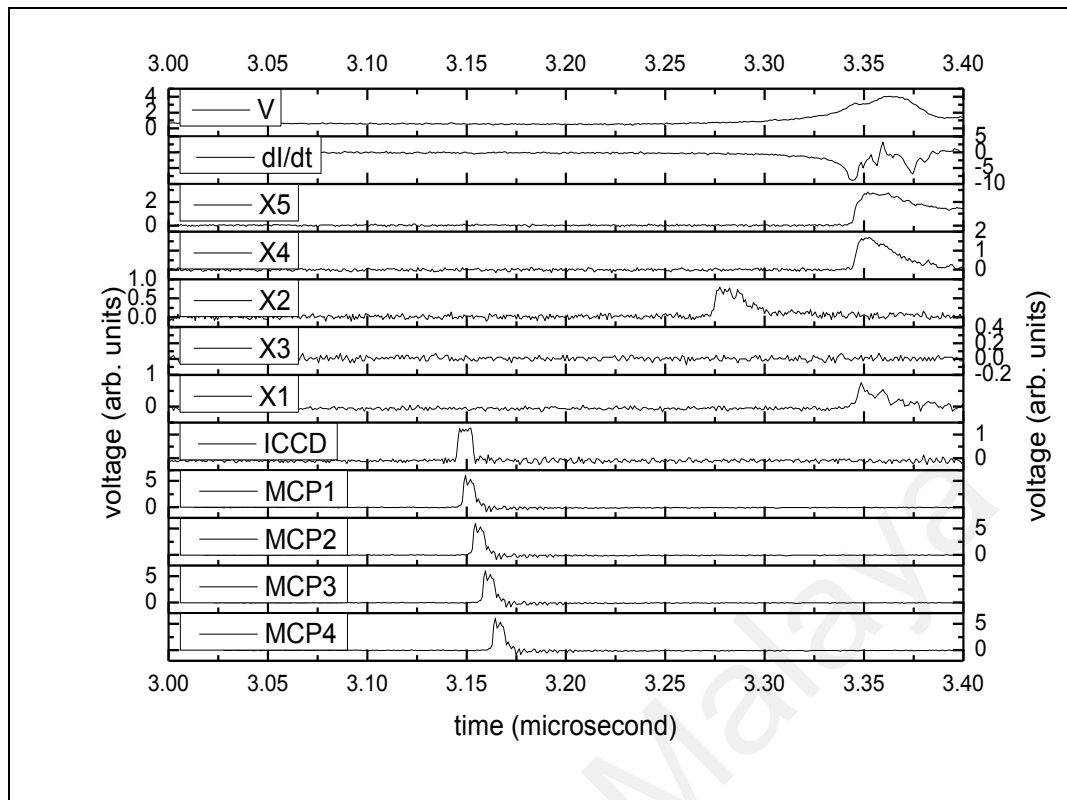
and Figure 4.5(c) are showing the ablation of anode is continuing and the remaining current sheath is pushed outward. Several images were obtained to study the plasma dynamic in this region, however no pinching has been registered through the spectrum of X-rays (Figure 4.10). The third region pinch may be due to sputtering of anode material (Rafique et al., 2010) or possibly also another plasma bubble formed above the first plasma bubble. However the field of view of ICCD is limited by the dimension of the view port did not allow the observation at further height. X-ray emission from the third region when pinching occurred on the surface of anode is shown in MCP's image in Figure 4.10. The emission is also dominated by copper K-alpha range.

After the third region pinch, ICCD imaging has been carried out with exposure time from 20 ns to 100 ns; the longer exposure time allowed integration of more intensity to identify the low intensity emission in this duration. Observation shown that ablation continues, more and more copper anode material evaporated to form a large amount of copper vapour above the anode (Figure 4.11(a) and Figure 4.11(b)). Initially the copper vapour expands upward collimated along the anode axis due to azimuthally magnetic field induced by focus discharge current. During the reverse cycle of the discharge it was observed that the copper vapour diffused to surrounding as shown in Figure 4.11(c) and Figure 4.11(d). Subsequently, in the next positive cycle of the voltage signal, it has been observed that copper vapour compressed at the center axis of anode (Figure 4.11(e)) and decay (Figure 4.11(f), Figure 4.11(g) and Figure 4.11(h)), then re-compressed again (Figure 4.11(i)). Finally the copper vapour decay and diffuse

into surrounding as shown in Figure 4.11(k).

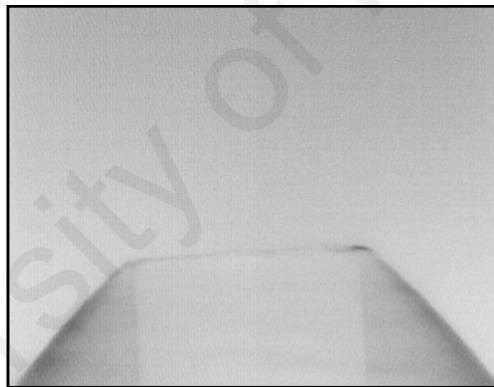
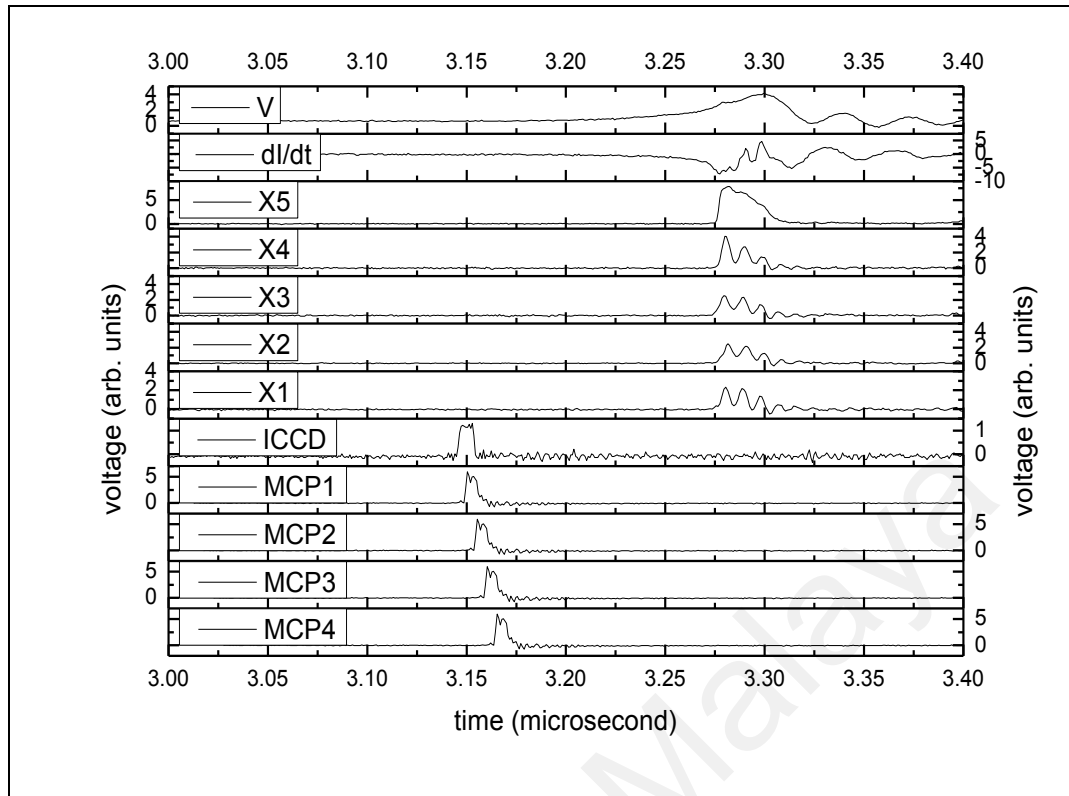
Throughout the whole experiment, an X-ray spectrometer XR-100 CR was used to measure an integrated the X-ray emission. A total 234 shots were accumulated and the spectrum is shown in Figure 4.12. Spectrum with energy of 400 eV and below are mainly due to background radiation. Emission from the neon plasma focus is mainly around 500 eV. This spectrum gives additional information to the measurements, while the PIN diode array and MCP did not have the respond sensitive to the 500 eV range.

University of Malaya



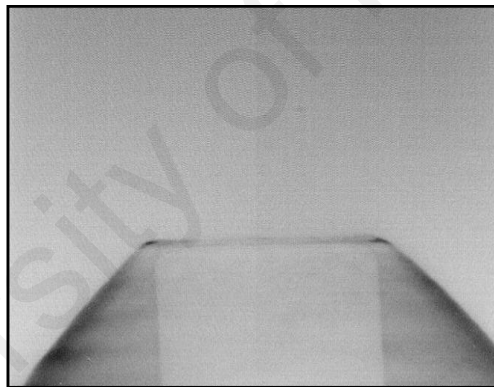
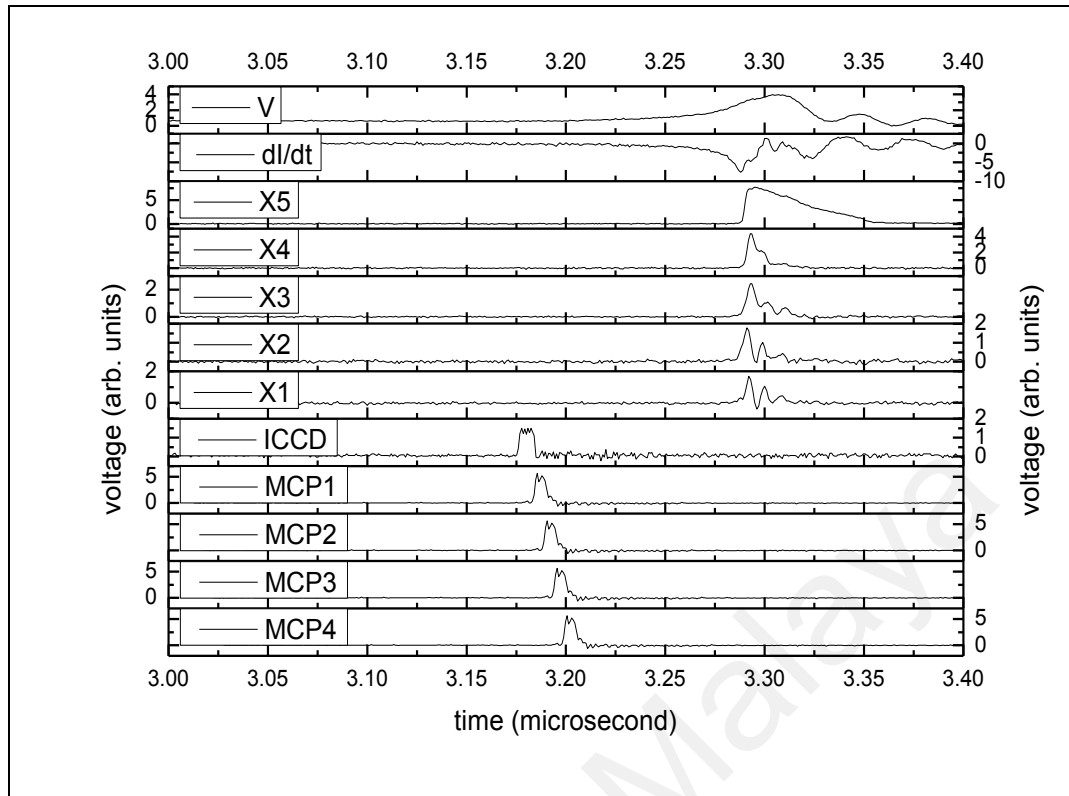
ICCD

Figure 4.2 (a): Before first region pinch for axial acceleration phase.



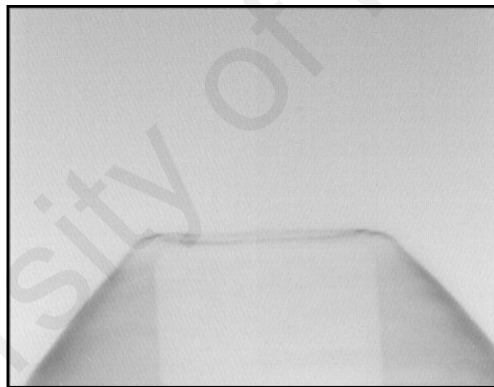
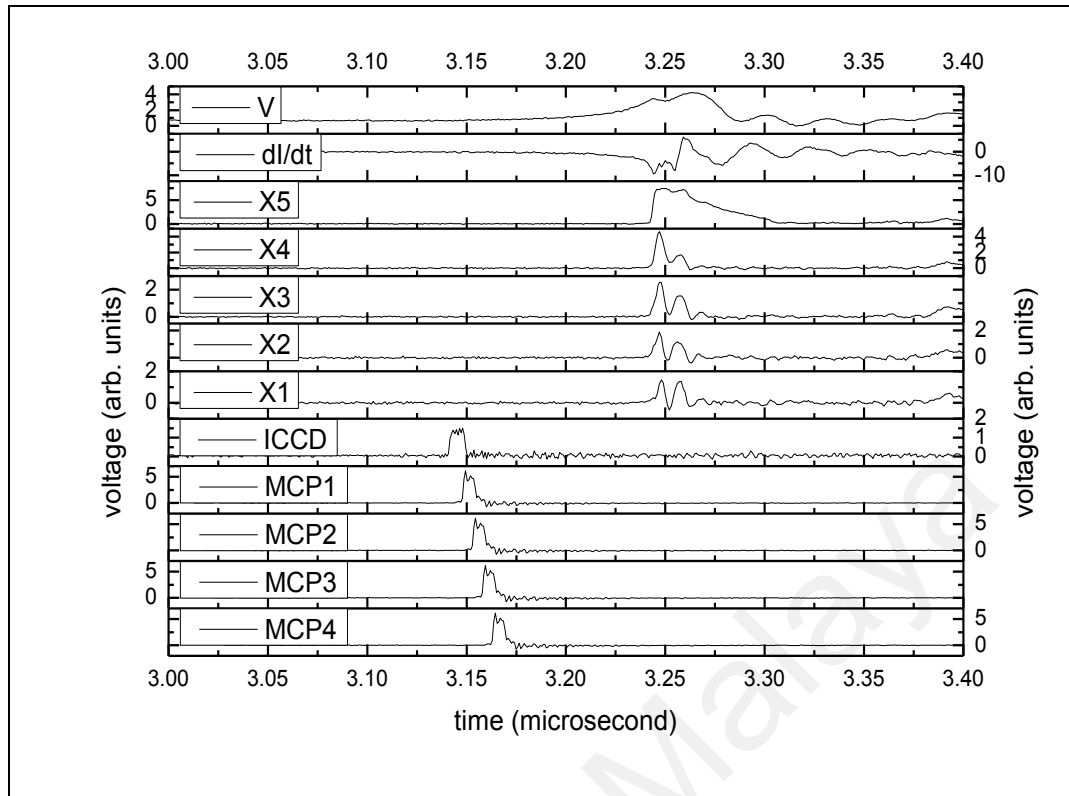
ICCD

Figure 4.2 (b): Before first region pinch for end of axial acceleration phase and at the point of beginning of the radial compression phase.



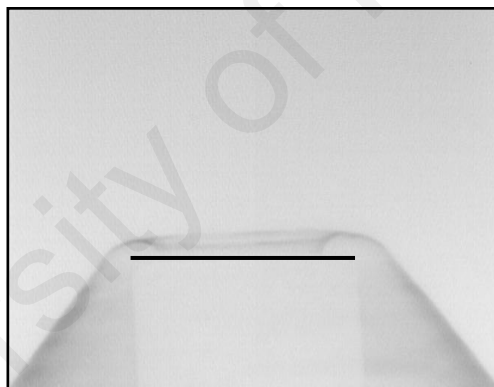
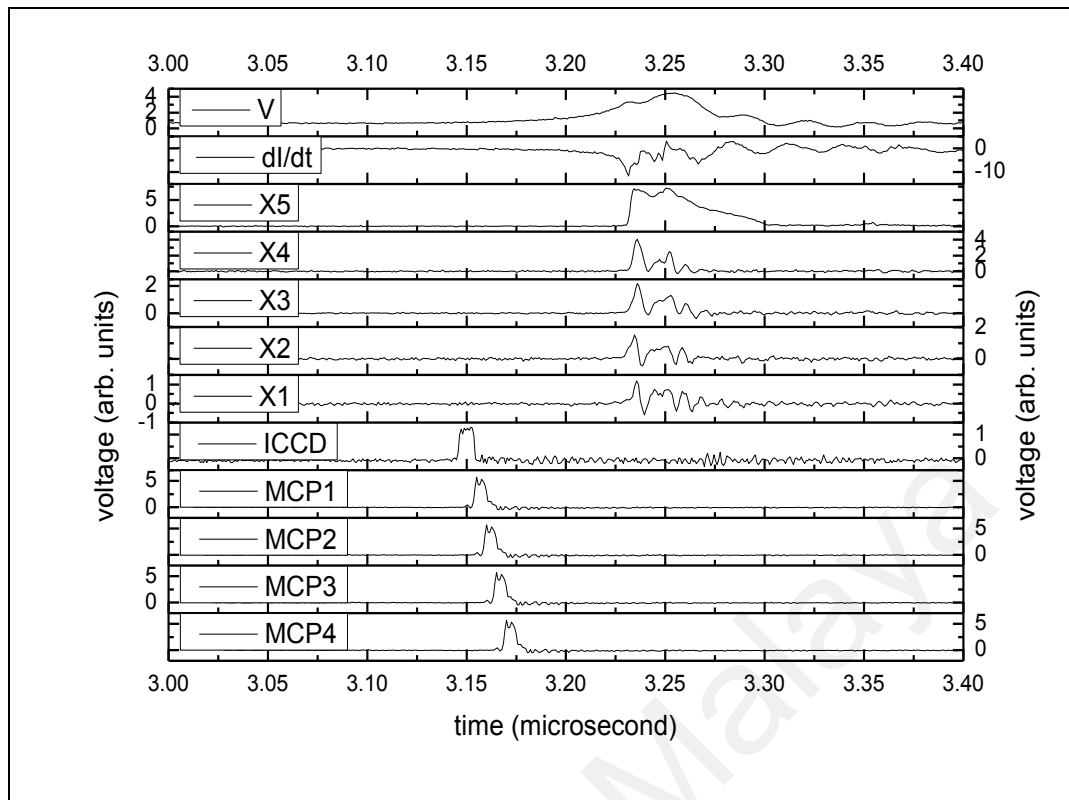
ICCD

Figure 4.2 (c): Before first region pinch for radial compression phase.



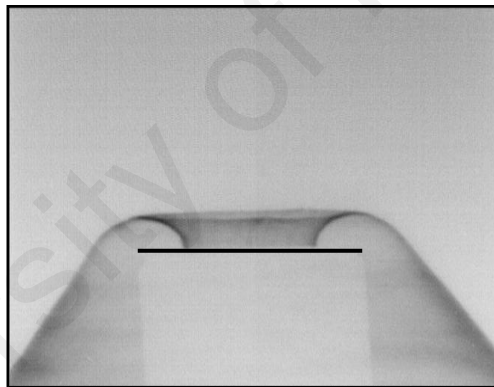
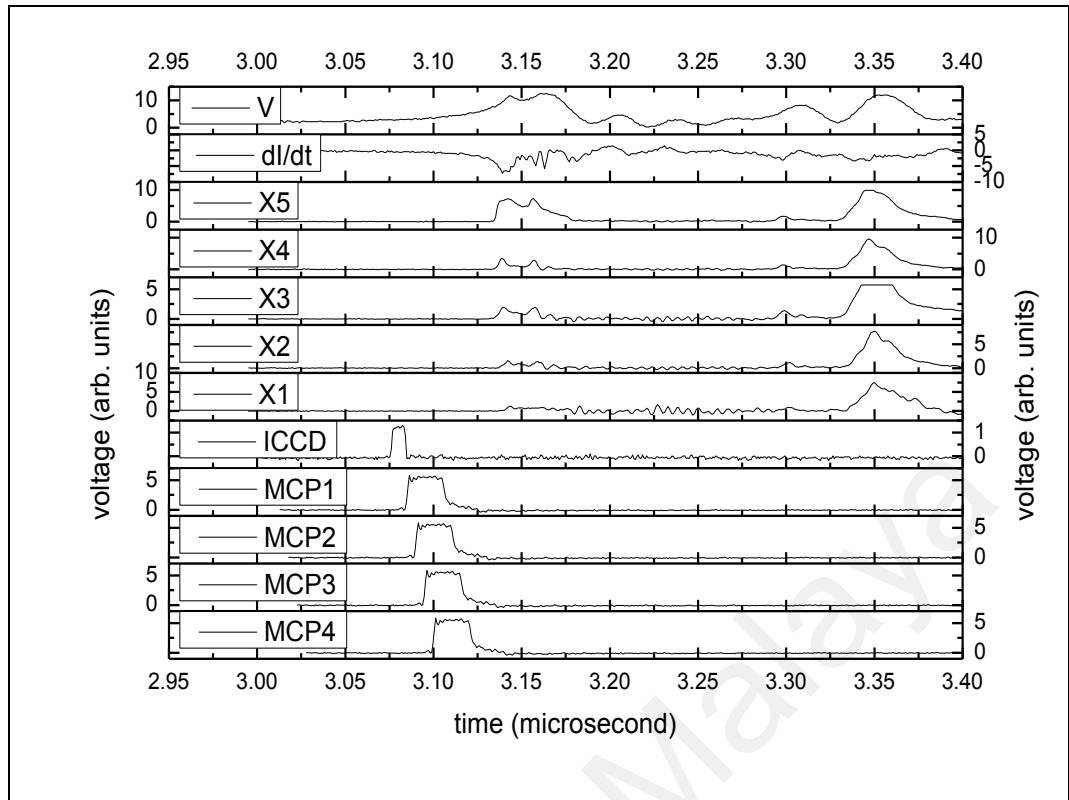
ICCD

Figure 4.2 (d): Before first region pinch for radial compression phase.



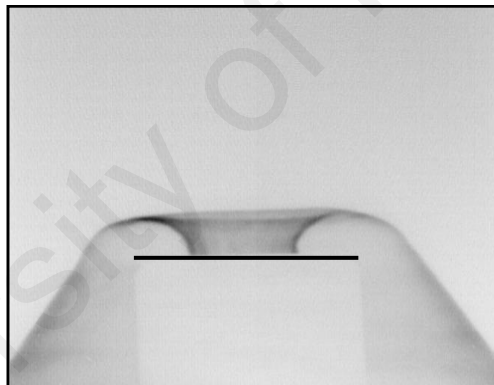
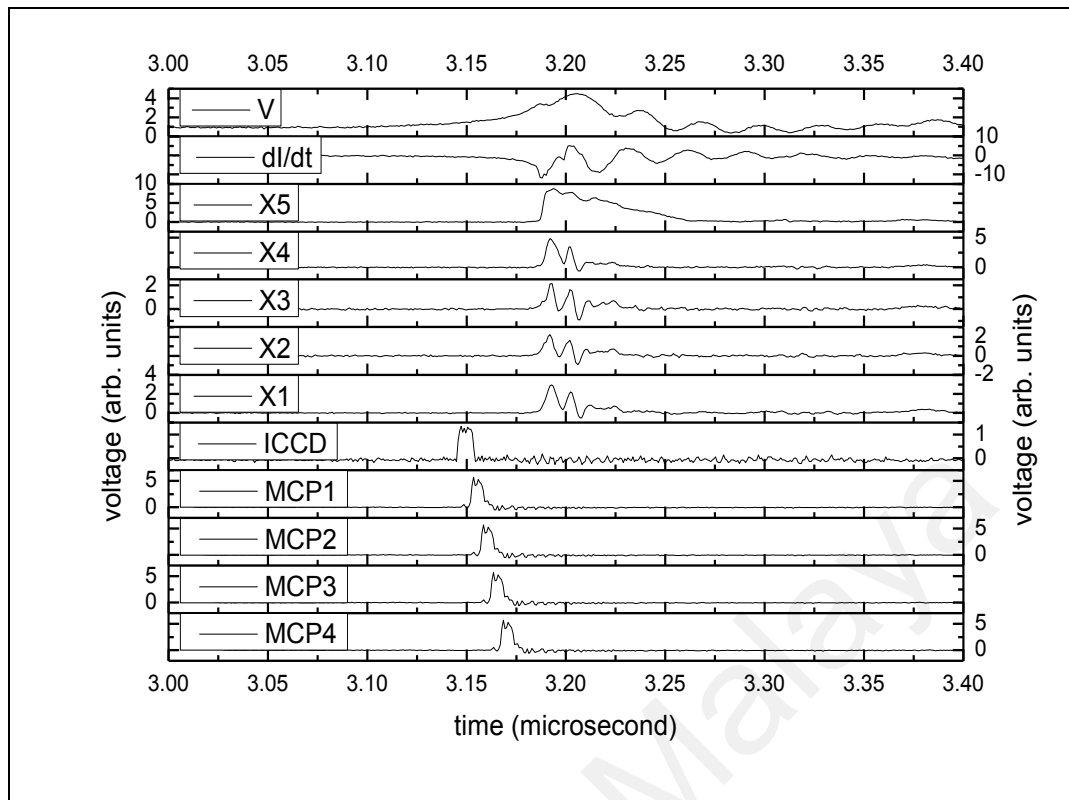
ICCD

Figure 4.2 (e): Before first region pinch for radial compression phase.



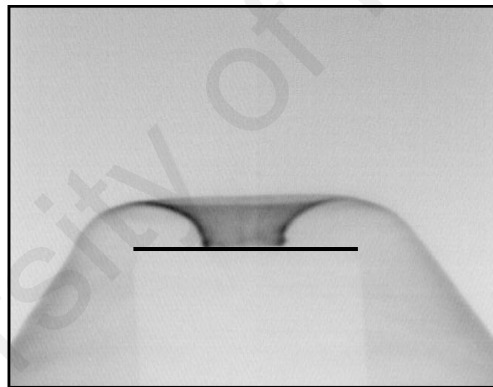
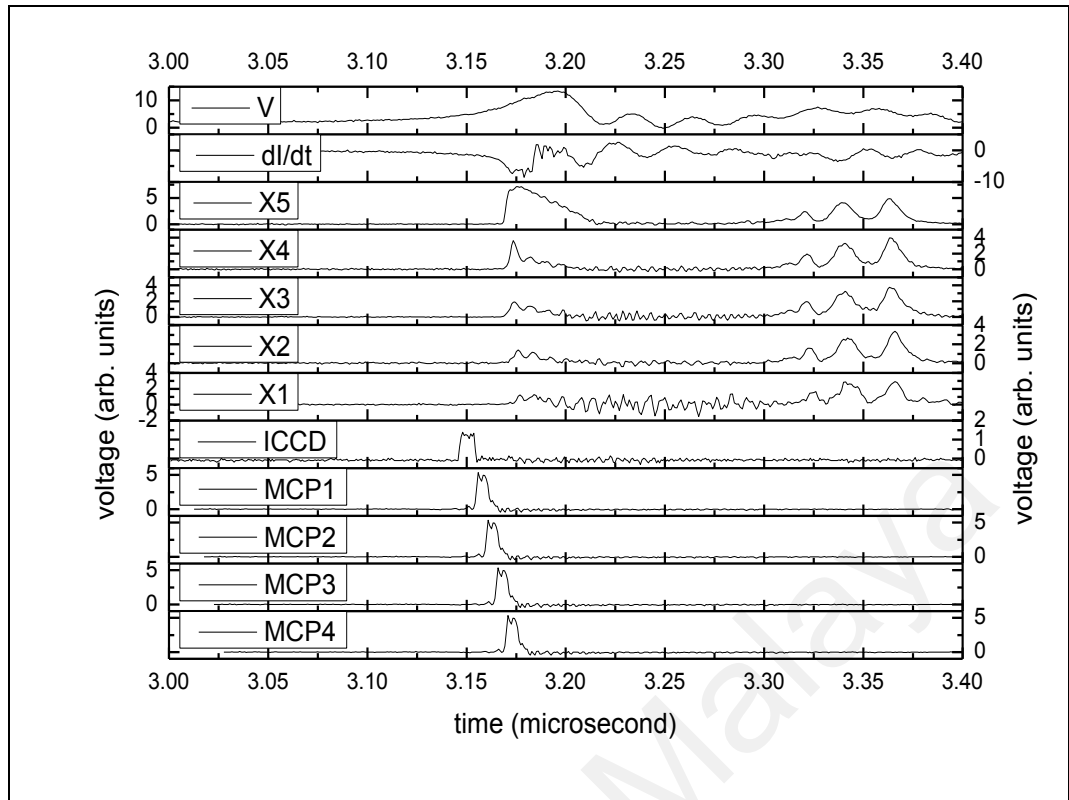
ICCD

Figure 4.2 (f): Before first region pinch for radial compression phase.



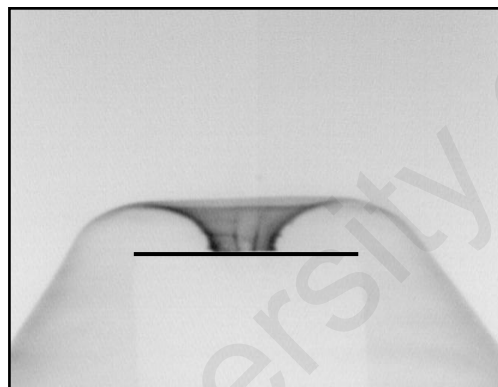
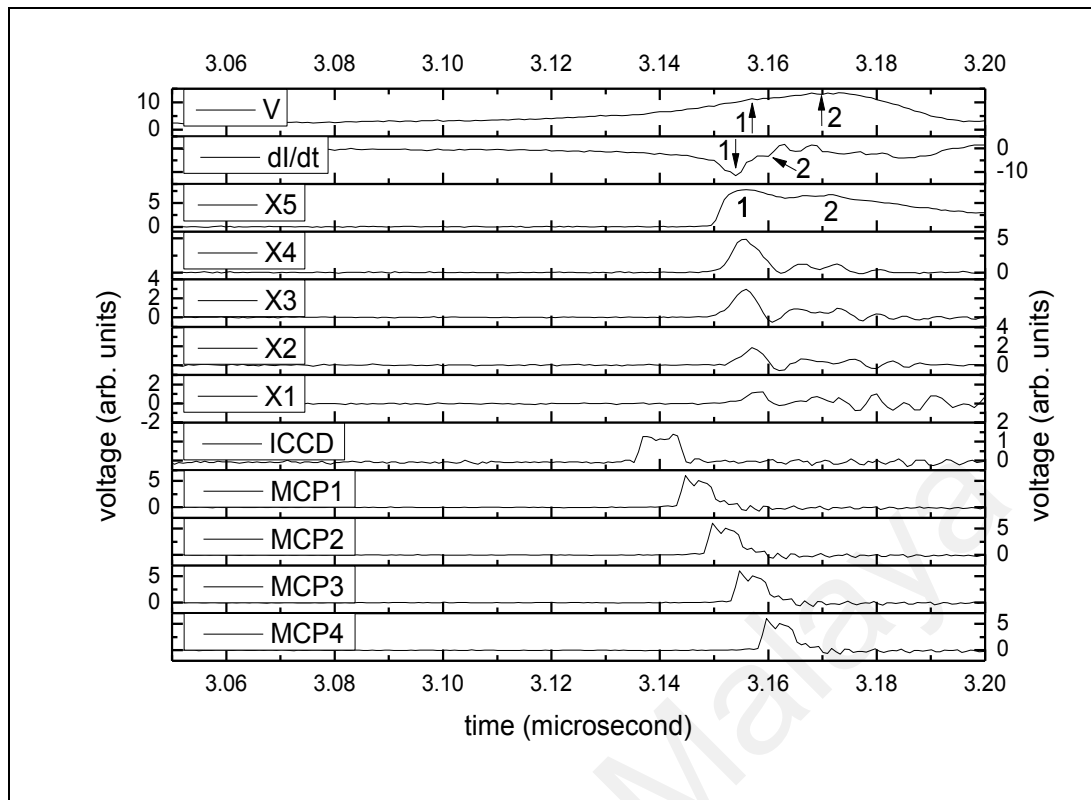
ICCD

Figure 4.2 (g): Before first region pinch for radial compression phase.

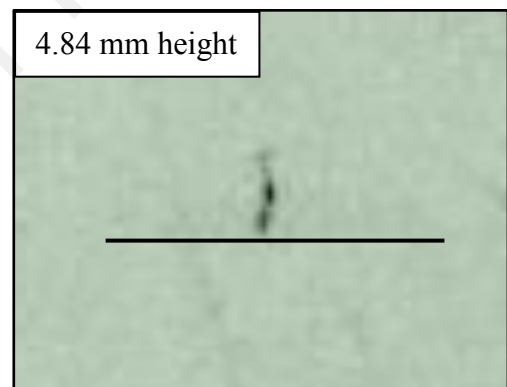


ICCD

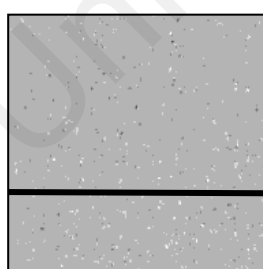
Figure 4.2 (h): Before first region pinch for radial compression phase.



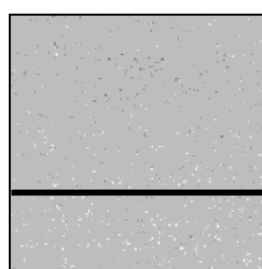
ICCD



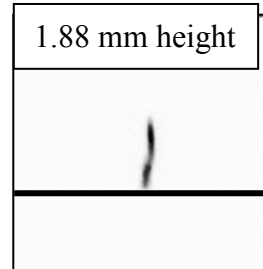
X-ray film



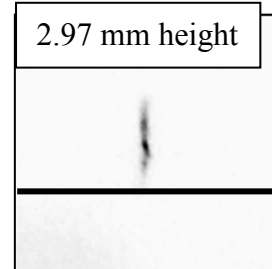
Channel 1



Channel 2

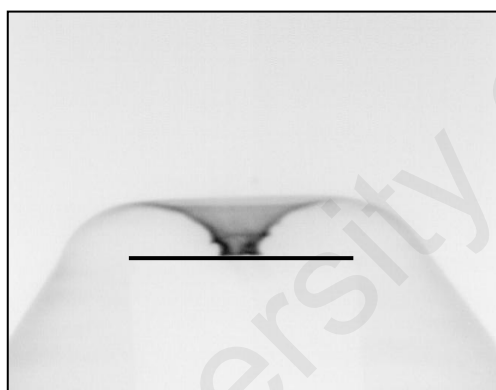
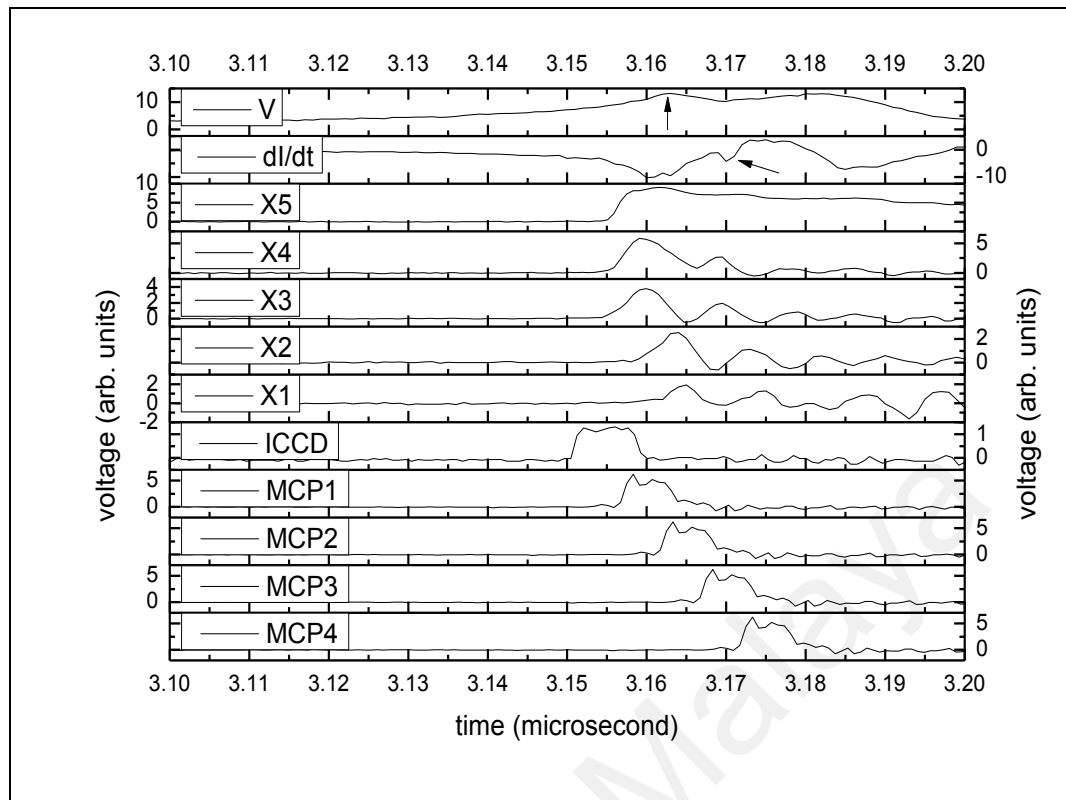


Channel 3

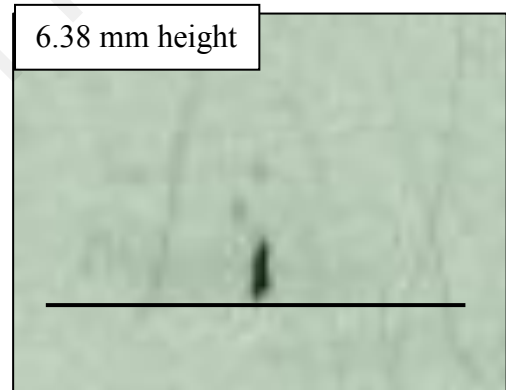


Channel 4

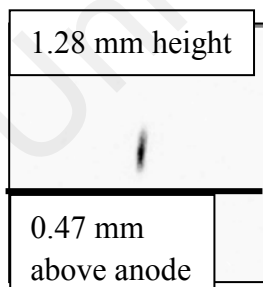
Figure 4.3 (a): First region pinch for distortion observed on current sheath due to RT instability, arrow 1 and 2 in dI/dt show in MCP3 (X-ray emitted from elongated plasma column) and MCP4 (column breaks into hot spots) respectively.



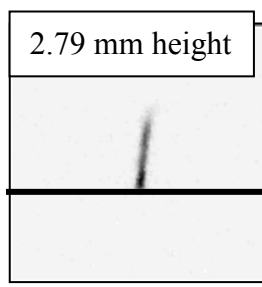
ICCD



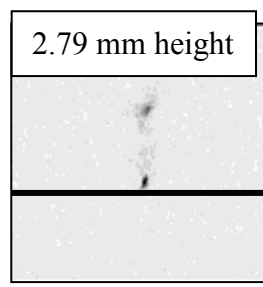
X-ray film



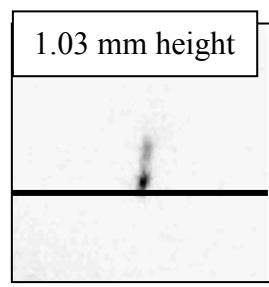
Channel 1



Channel 2

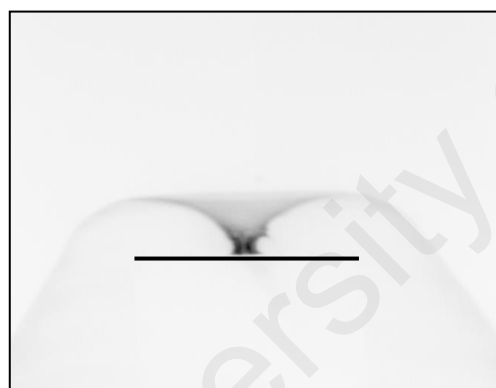
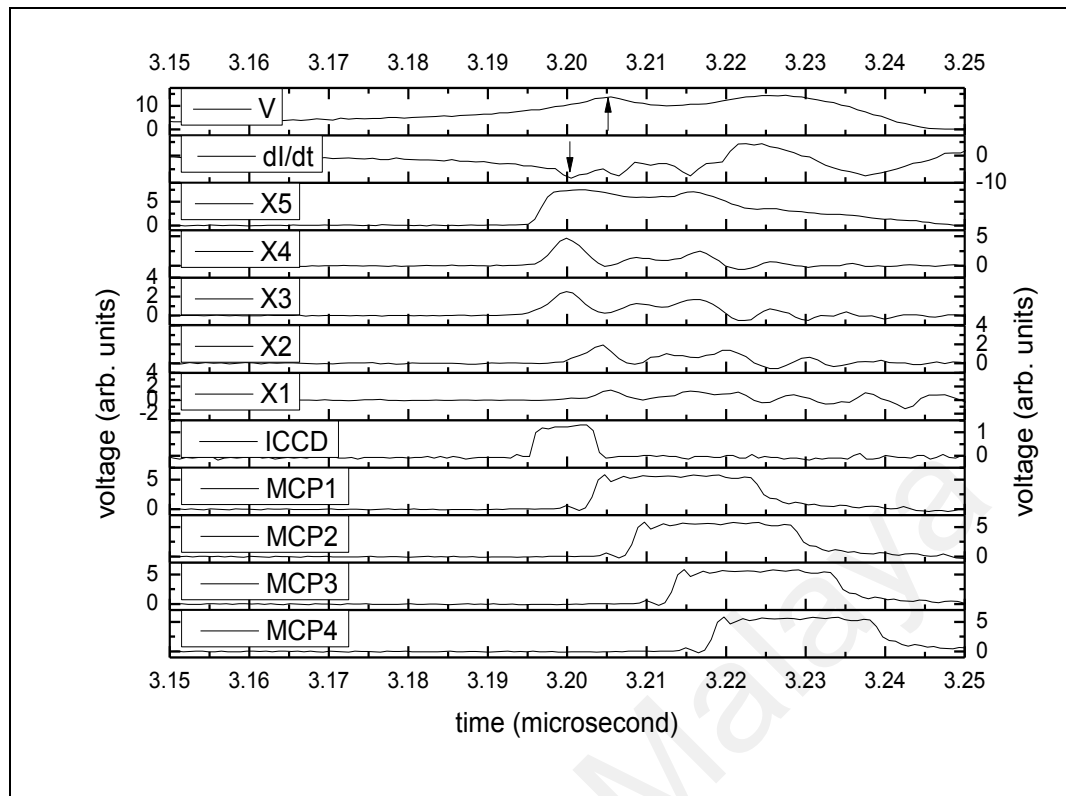


Channel 3

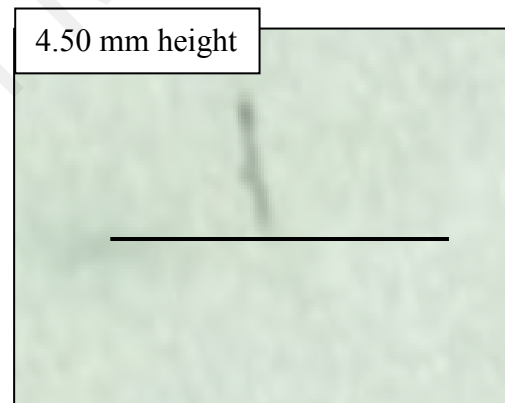


Channel 4

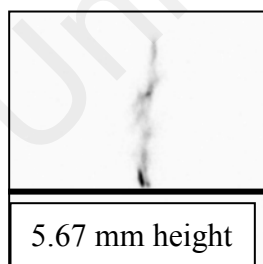
Figure 4.3 (b): First region pinch for MCP2 and MCP3 at the peak of V (arrow) and dI/dt (arrow) where plasma column elongated and break into hot spots respectively.



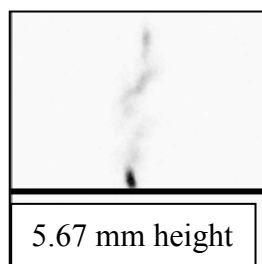
ICCD



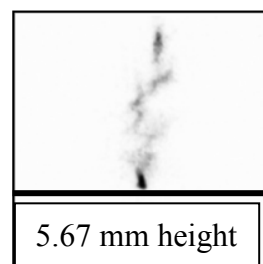
X-ray film



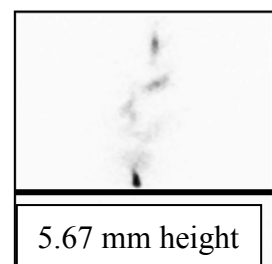
Channel 1



Channel 2

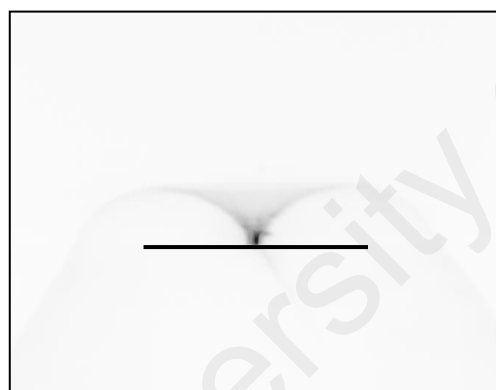
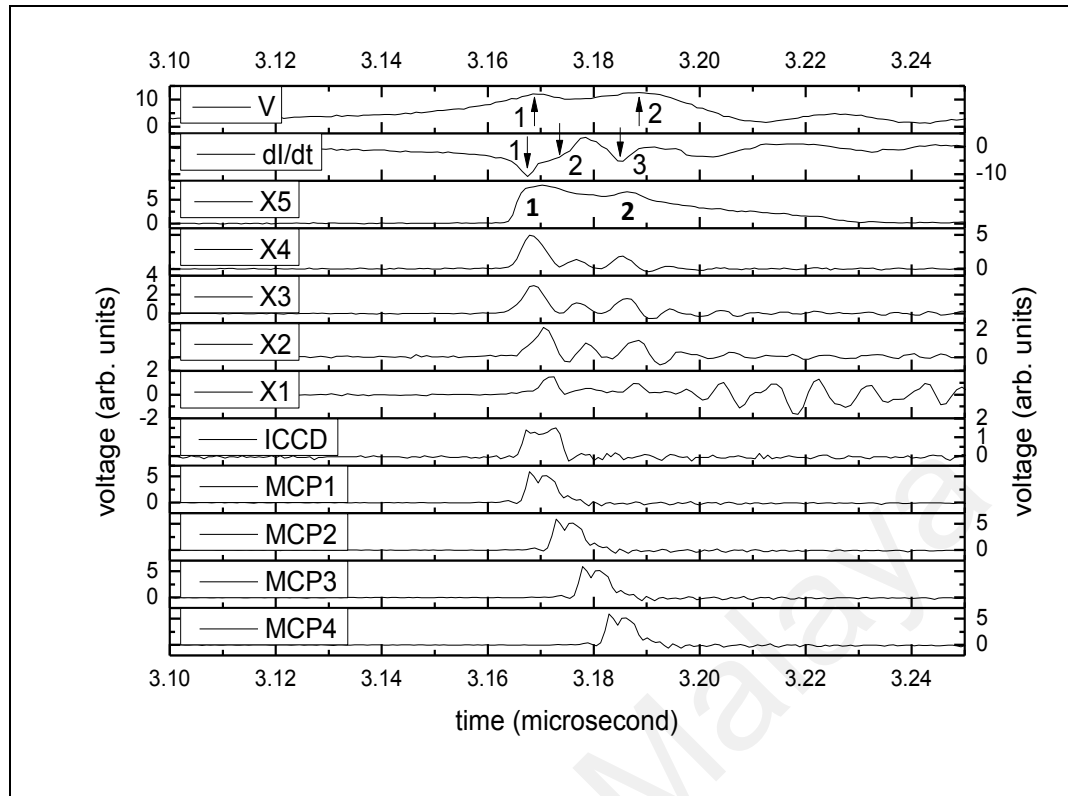


Channel 3

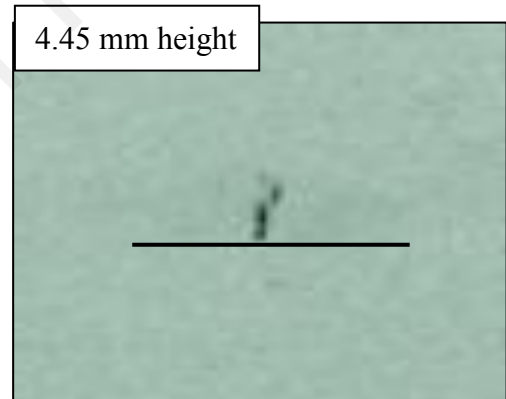


Channel 4

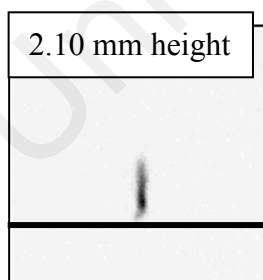
Figure 4.3 (c): First region pinch for MCP open shuttle time is 20 ns, kink instabilities is clearly view, ICCD's image shows the first compression at the first peak of dl/dt (arrow) and before first peak of V (arrow).



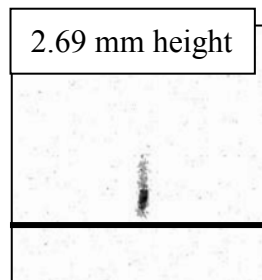
ICCD



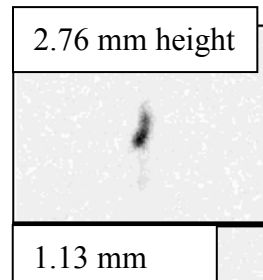
X-ray film



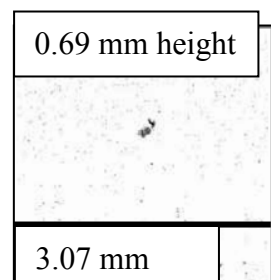
Channel 1



Channel 2

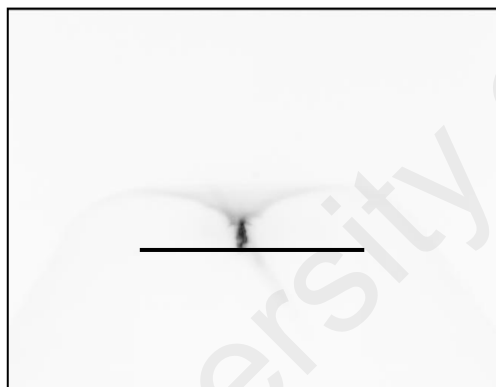
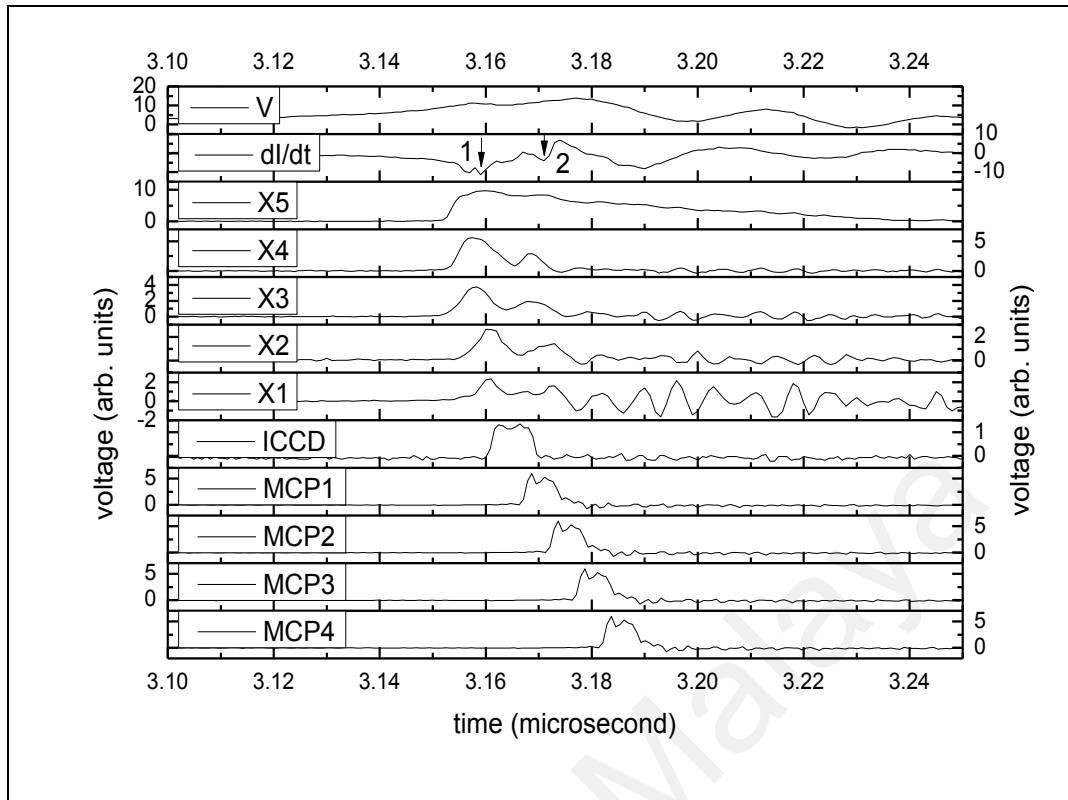


Channel 3

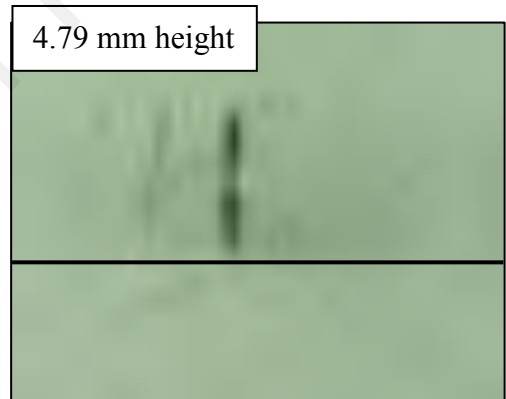


Channel 4

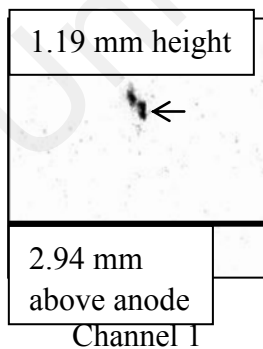
Figure 4.3 (d): First region pinch for first region pinch for arrow 1 (V and dl/dt) is first compression and plasma column elongated, arrow 2 (dl/dt , MCP2) is hot spots, arrow 3 (dl/dt , MCP4) is second compression breaks into hot spot.



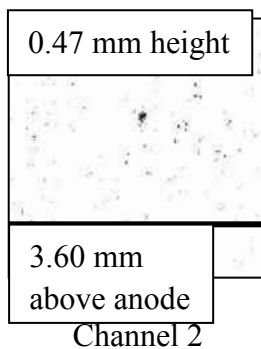
ICCD



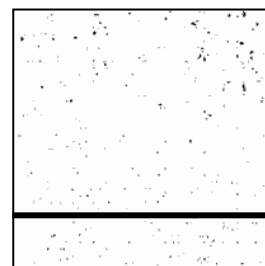
X-ray film



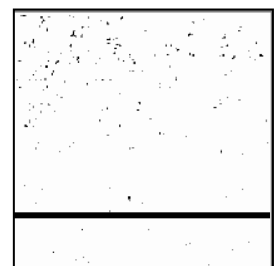
Channel 1



Channel 2

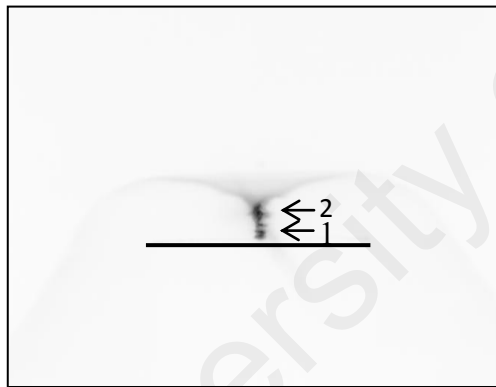
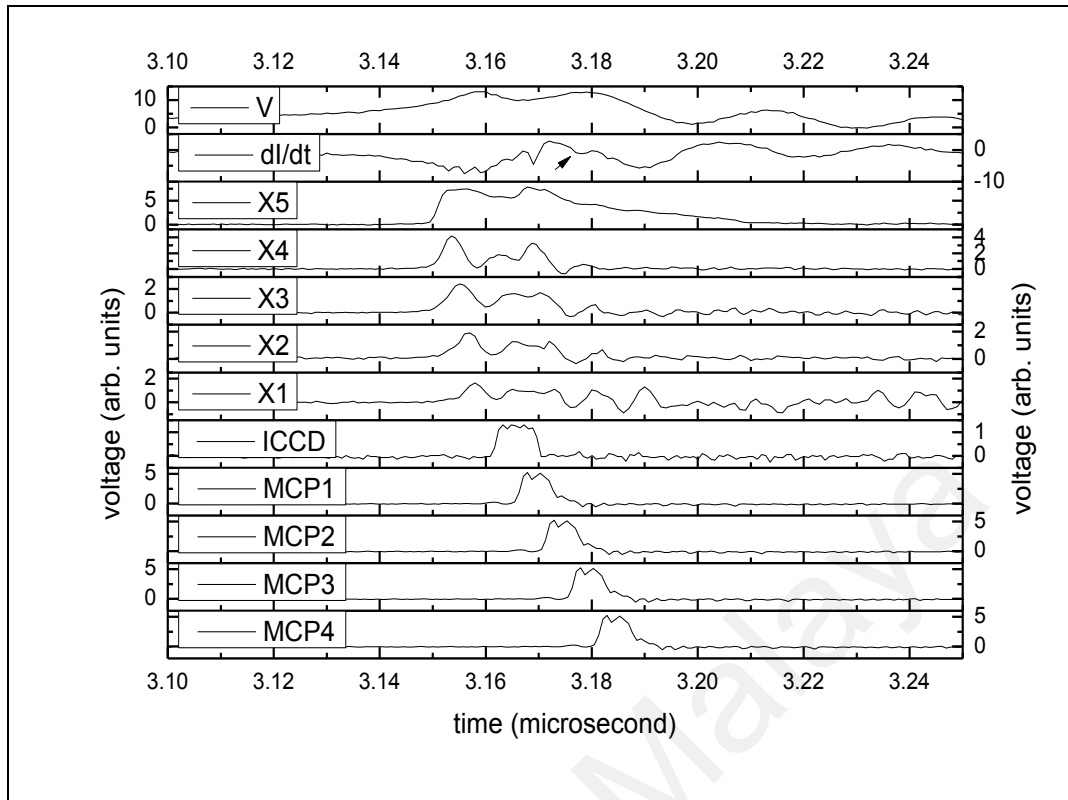


Channel 3

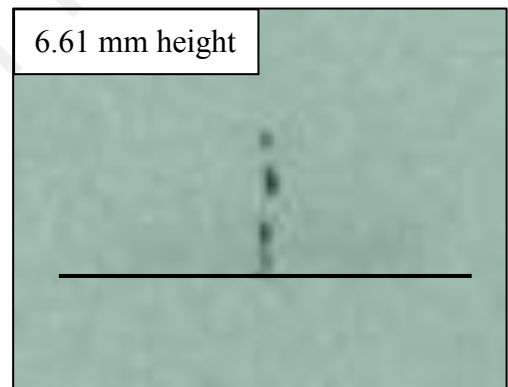


Channel 4

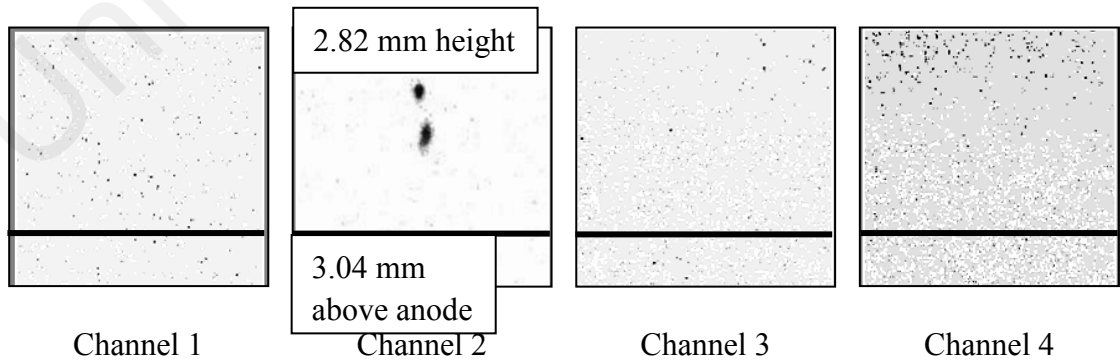
Figure 4.3 (e): First region pinch for arrow 1 of dl/dt is maximum compression, arrow 2 is plasma column break down as shown in MCP1.



ICCD



X-ray film



Channel 1

Channel 2

Channel 3

Channel 4

Figure 4.3 (f): First region pinch for in ICCD's image, the bottom black arrow 1 is hot spot from first compression, the upper black arrow 2 is second compression, arrow in dI/dt is second compression plasma column breaks into hot spots.

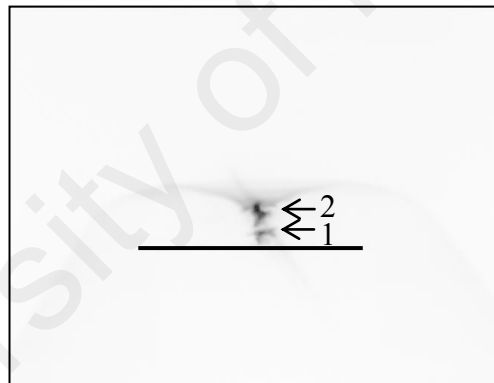
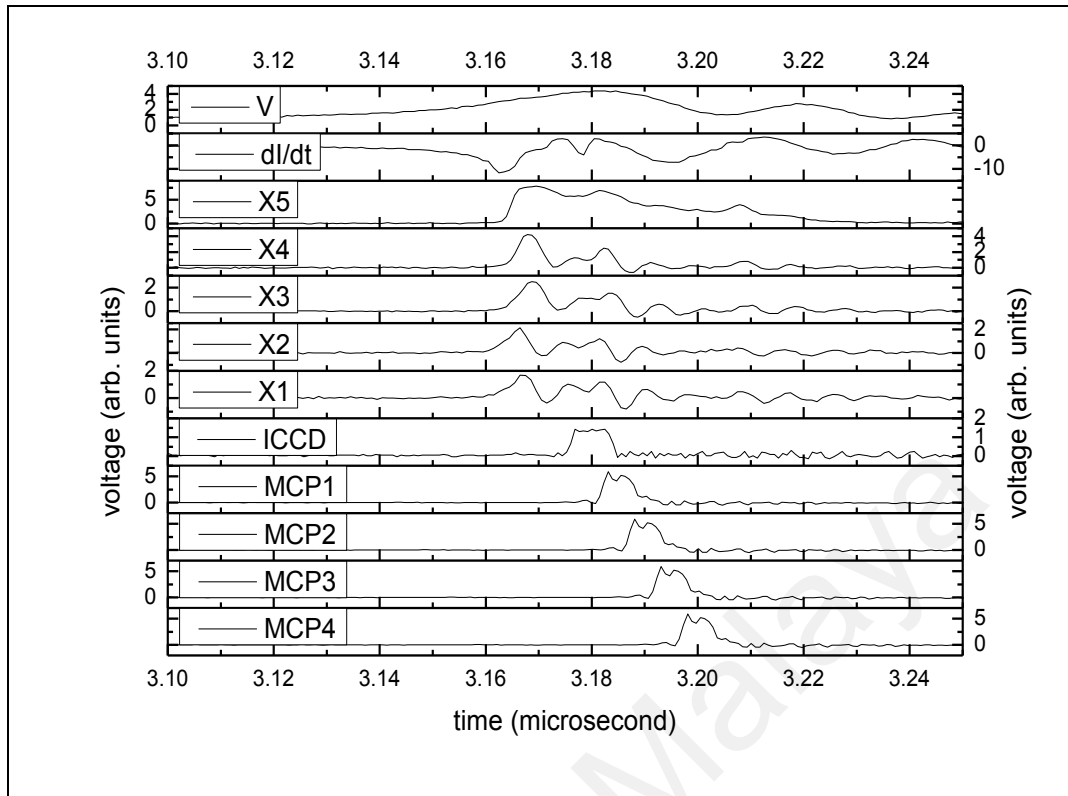


Figure 4.3 (g): First region pinch for In ICCD's image, the bottom black arrow 1 is hot spot from first compression undergoes diffusion, the upper black arrow 2 is second compression.

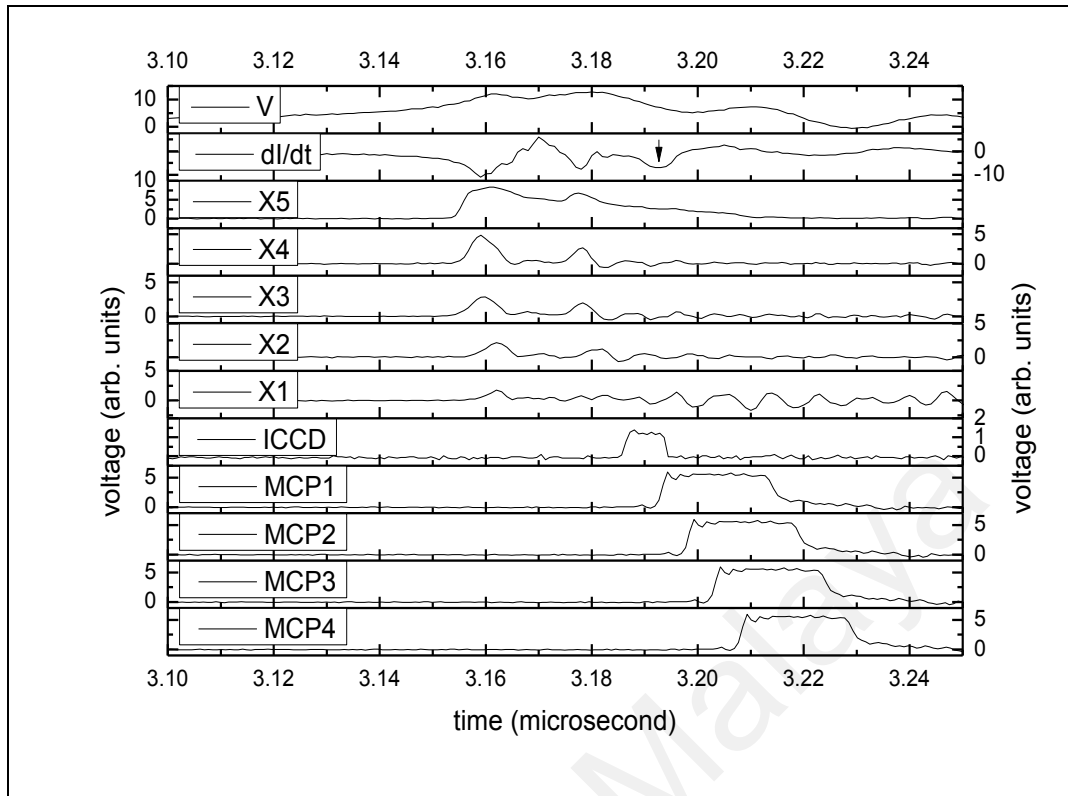


Figure 4.3 (h): First region pinch for a layer of visible light is observed on the anode's surface, arrow in dl/dt shows remaining plasma is compressed to higher area.

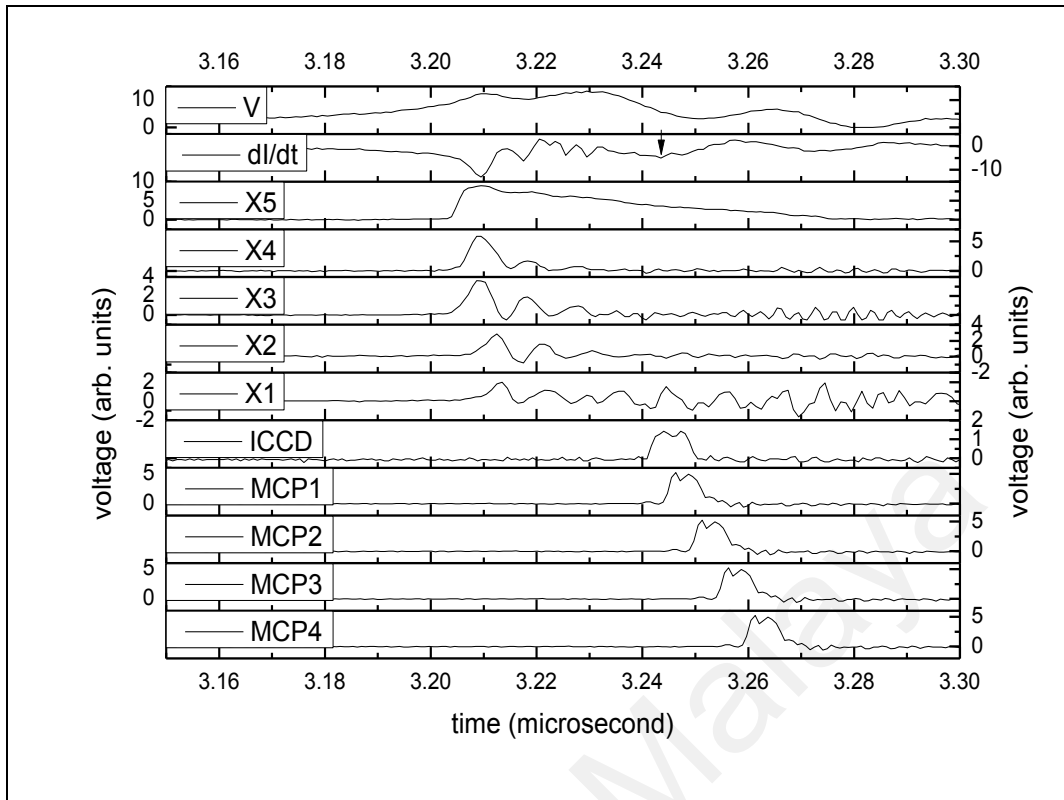


Figure 4.3 (i): First region pinch for the remaining plasma is compressed into another intense spot.

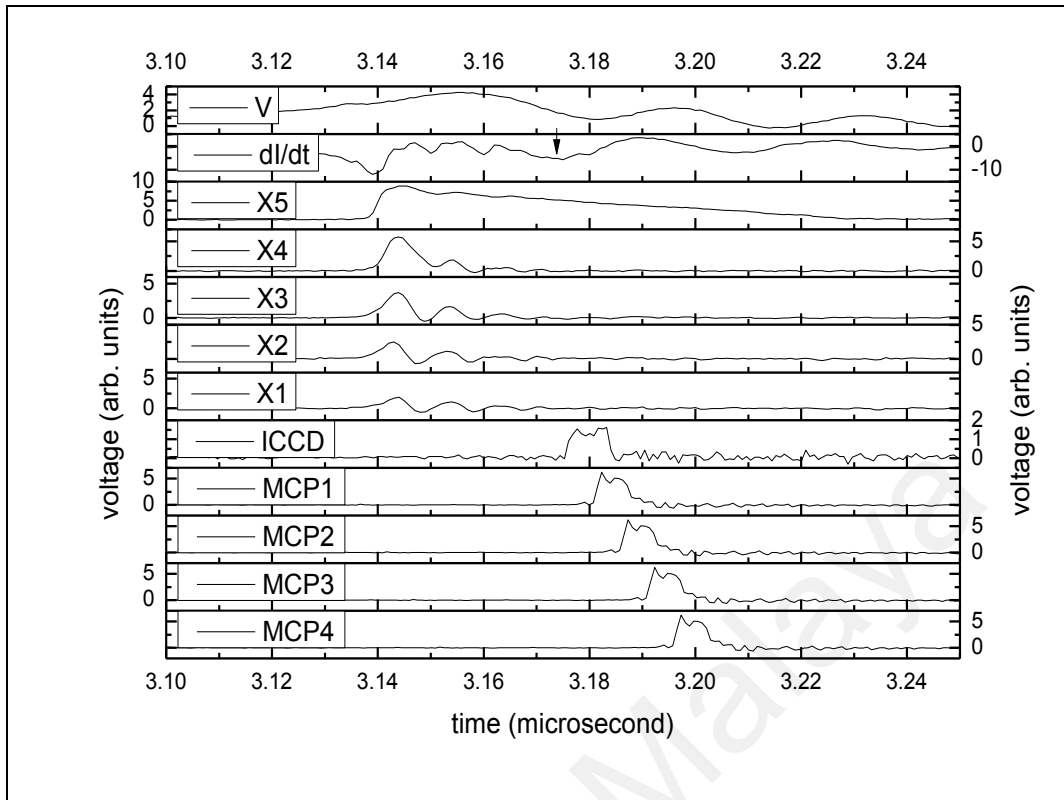


Figure 4.3 (j): First region pinch for intense spot starts to decay and induce a shock wave.

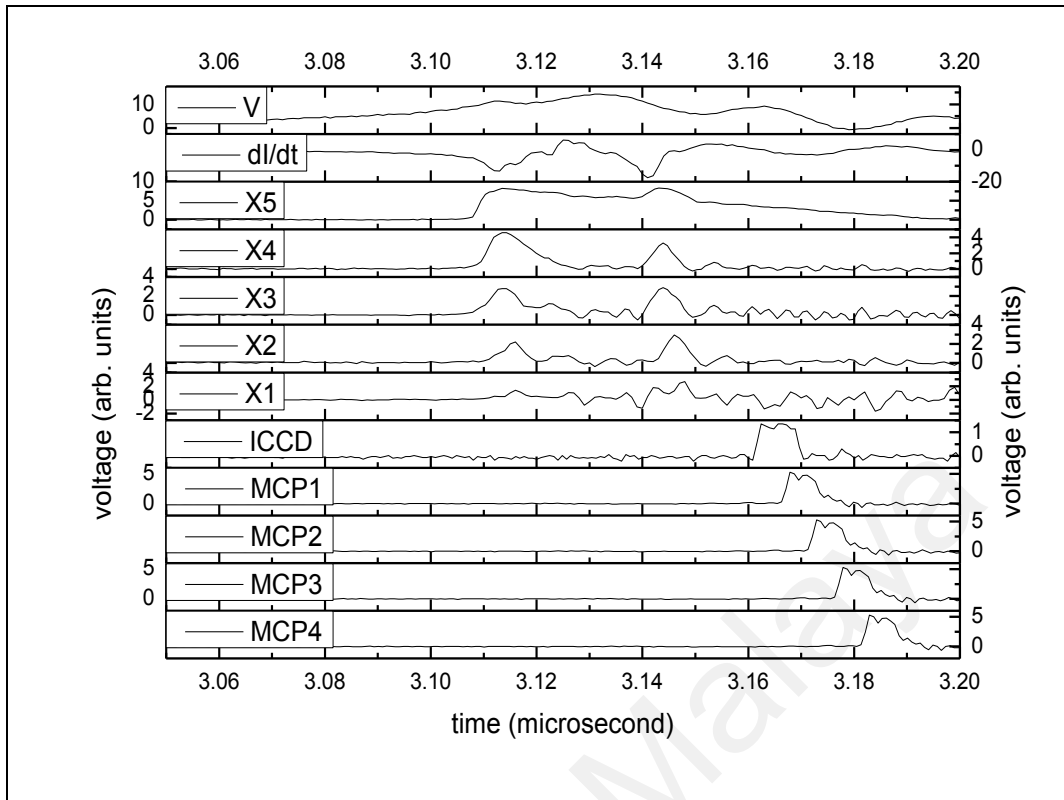


Figure 4.3 (k): First region pinch for induced shock wave move outward and form plasma bubble.

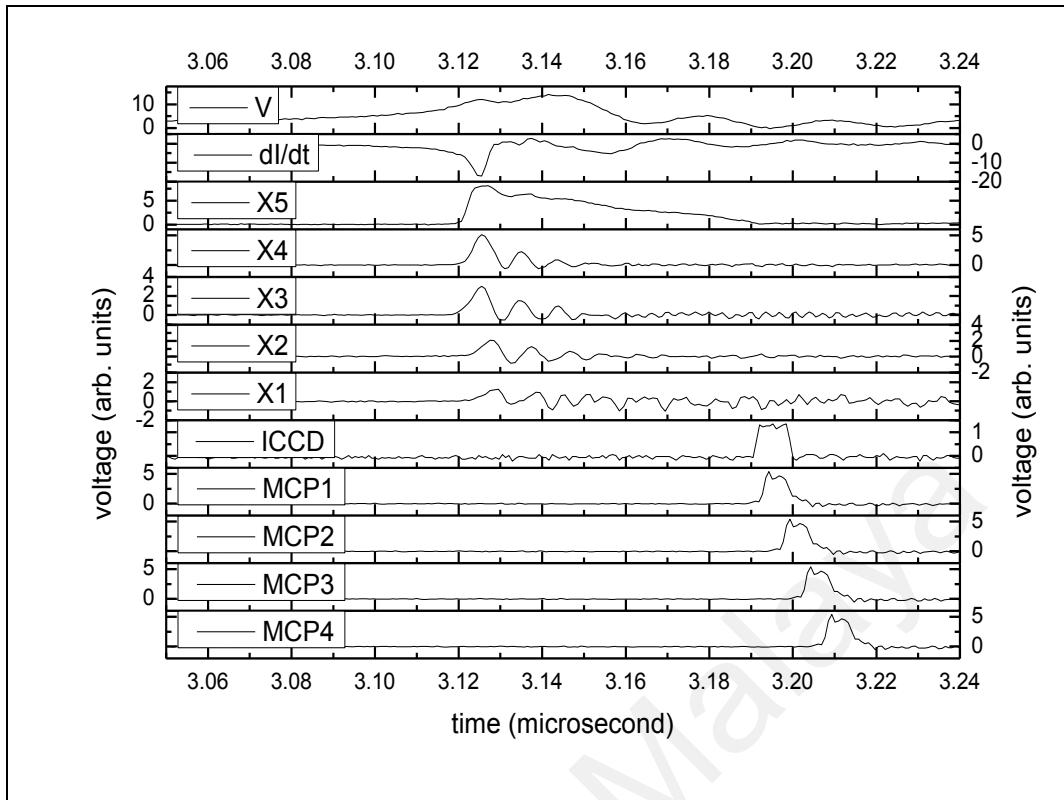


Figure 4.4 (a): Second region pinch for plasma bubble continues expand.

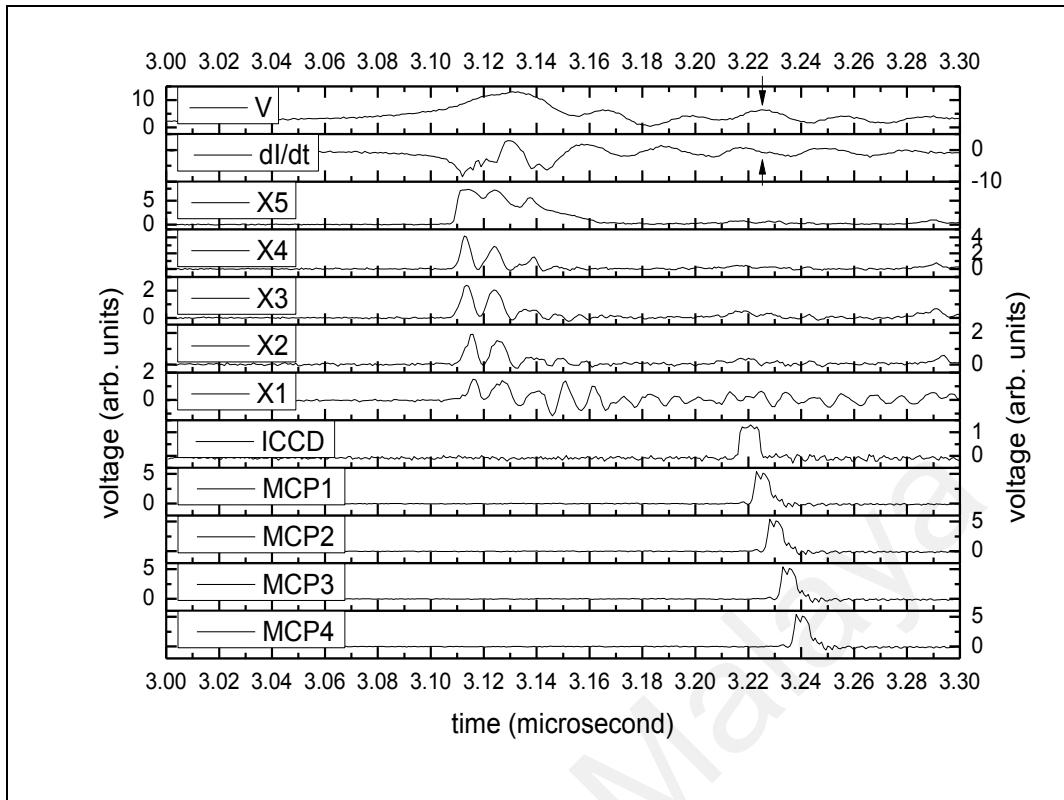


Figure 4.4 (b): Second region pinch for another pinch is formed inside plasma bubble, top of plasma bubble distorted may due to burst out of ion beams.

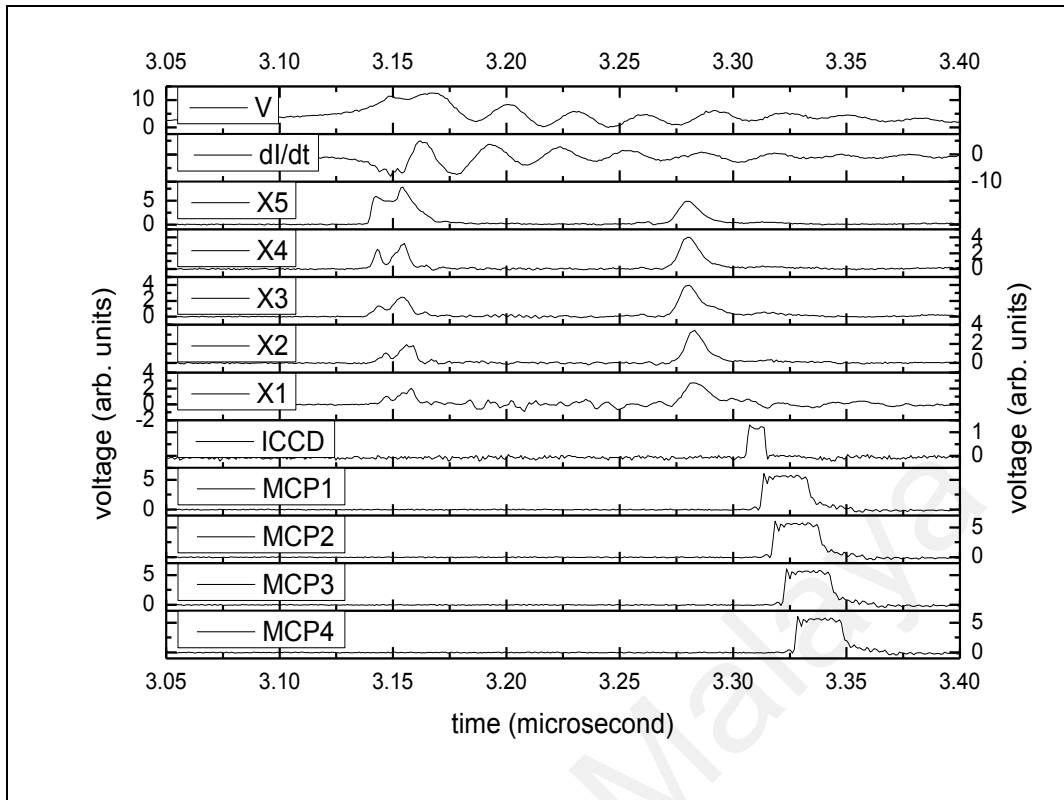


Figure 4.4 (c): Second region pinch for ablation of anode continues.

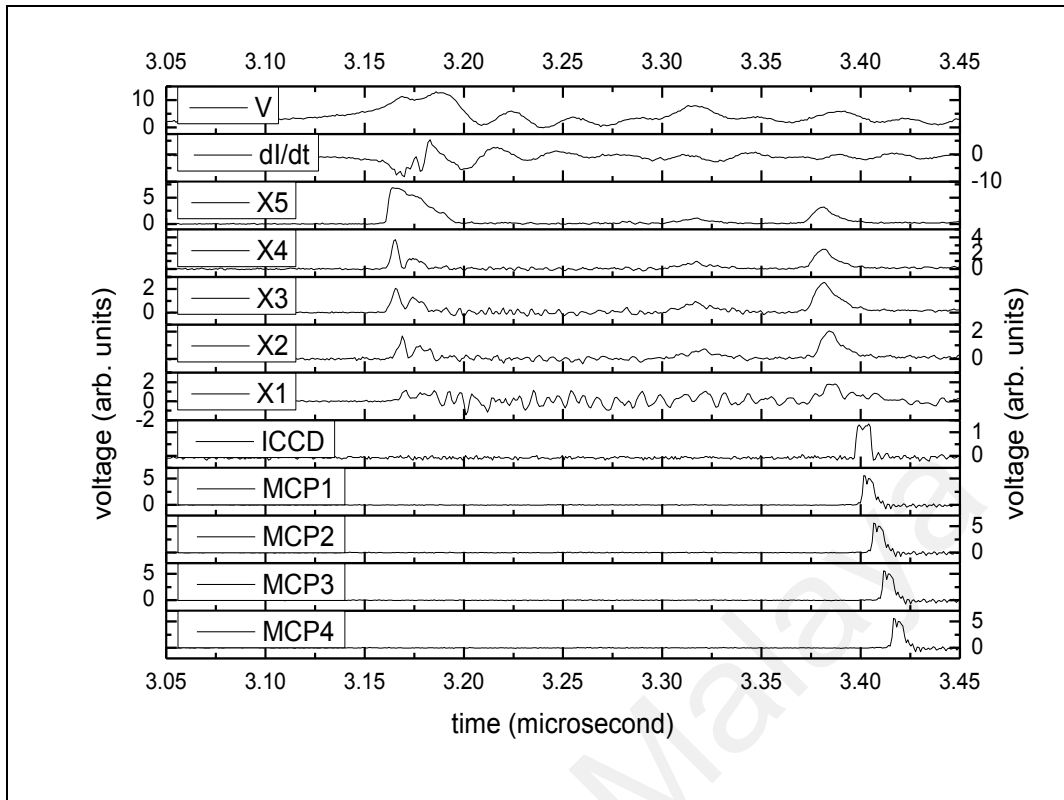


Figure 4.5 (a): Ablation on anode for ablation of anode continues.

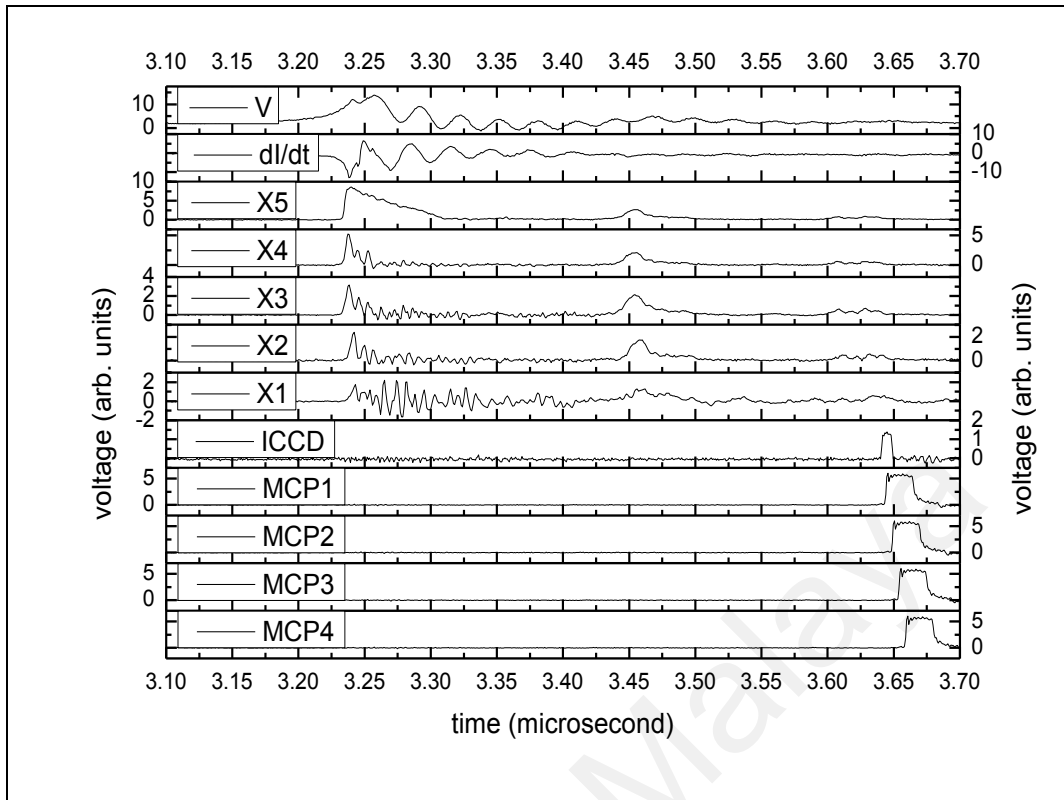


Figure 4.5 (b): Ablation on anode for ablation of anode continues.

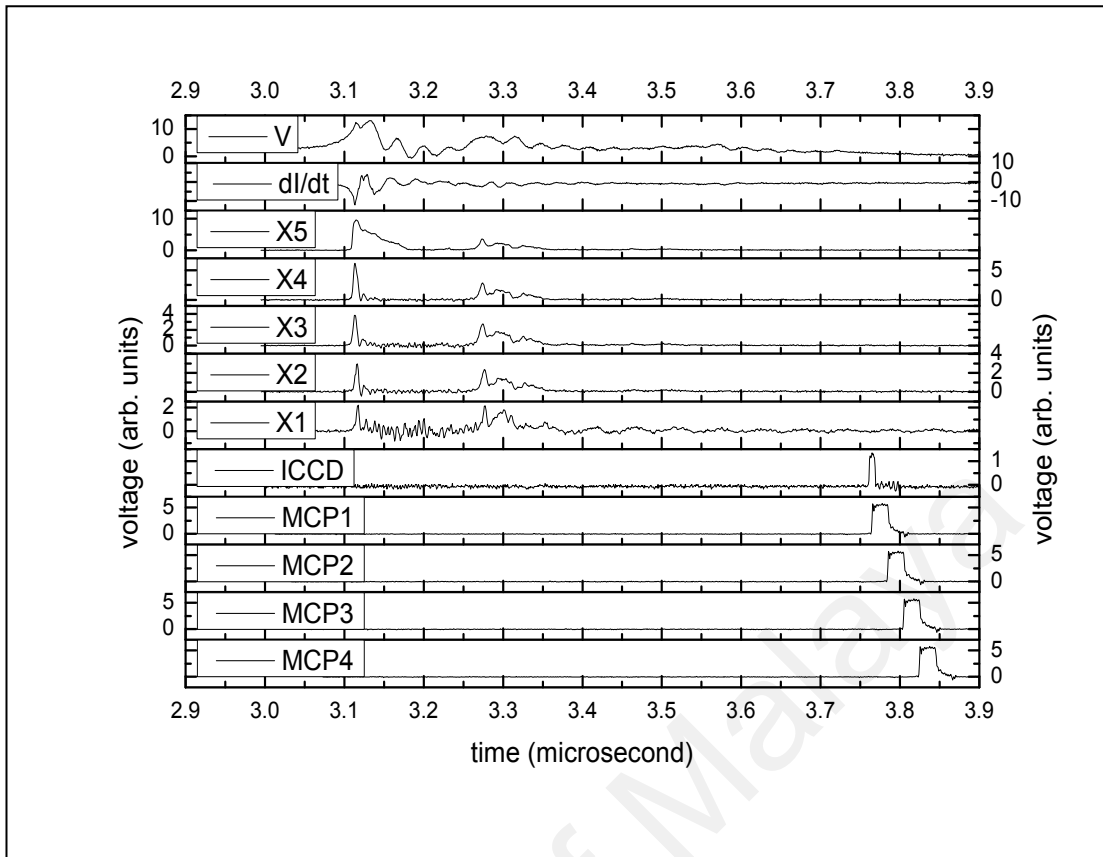


Figure 4.5 (c): Ablation on anode for ablation of anode continues.

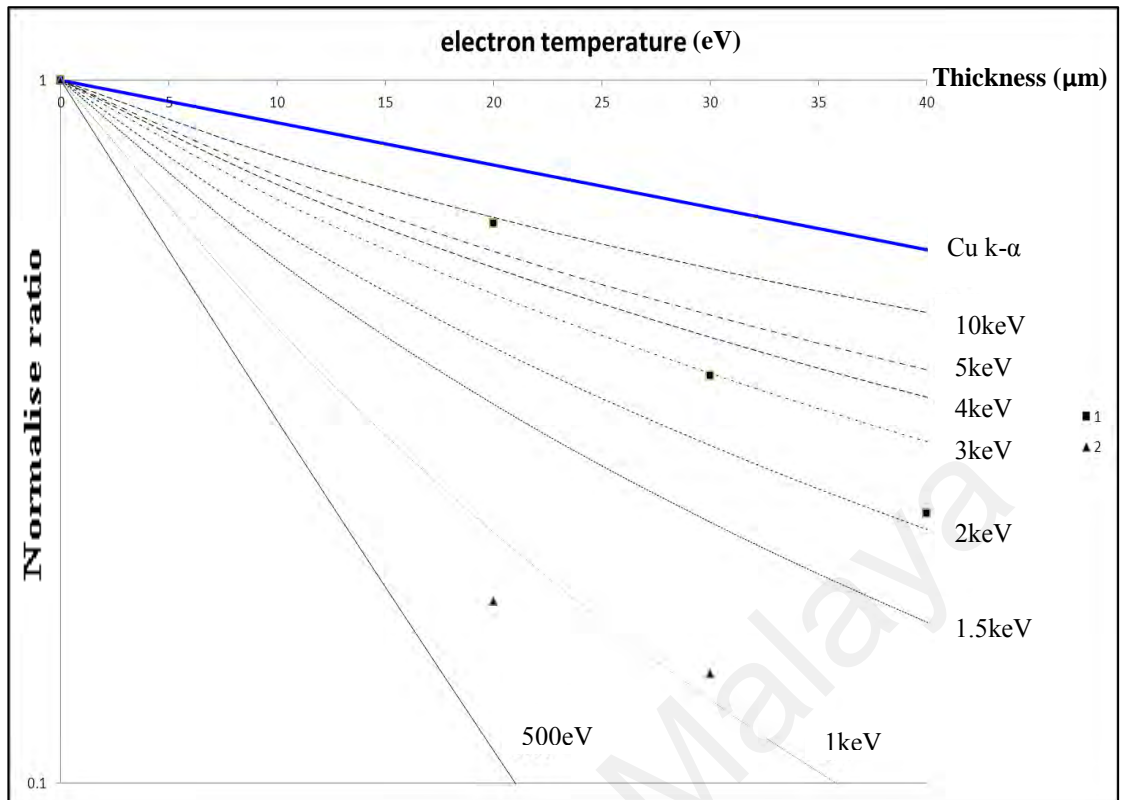


Figure 4.6 (a): Plasma temperature first region pinch for electron temperature of peak 1 and 2 in X5 from Figure 4.3(a).

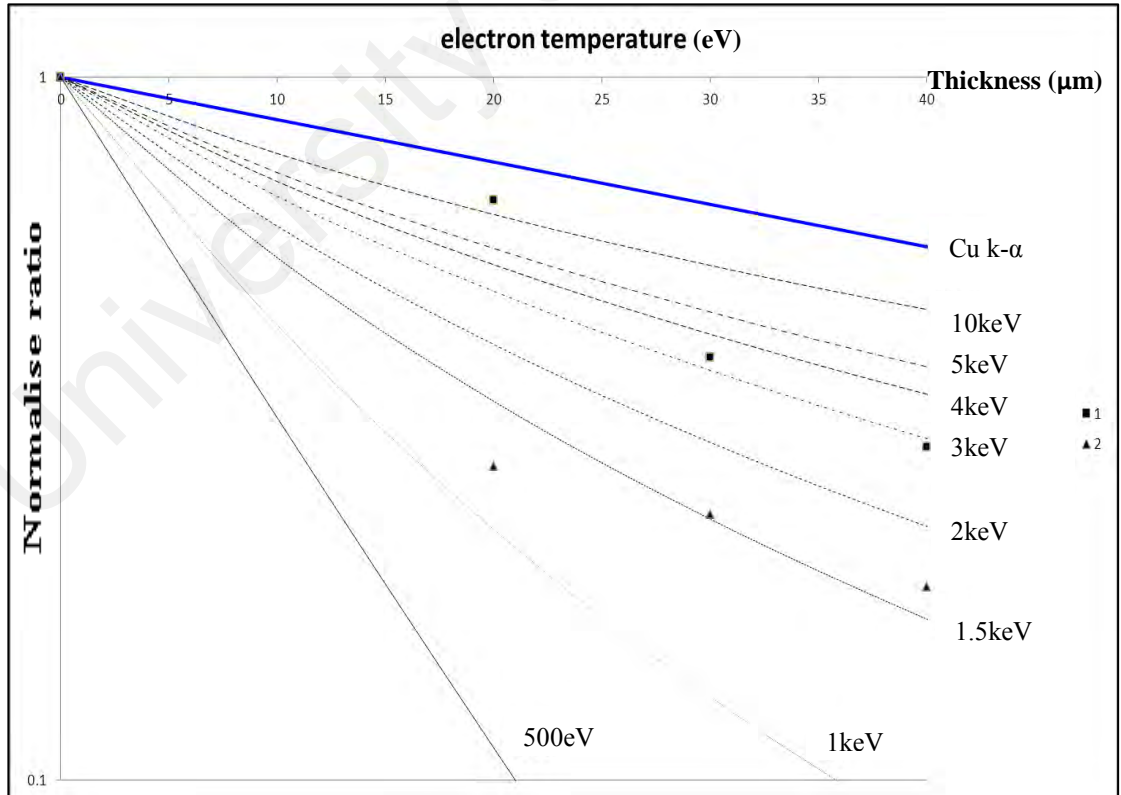


Figure 4.6 (b): Plasma temperature first region pinch for electron temperature of peak 1 and 2 in X5 from Figure 4.3(d).

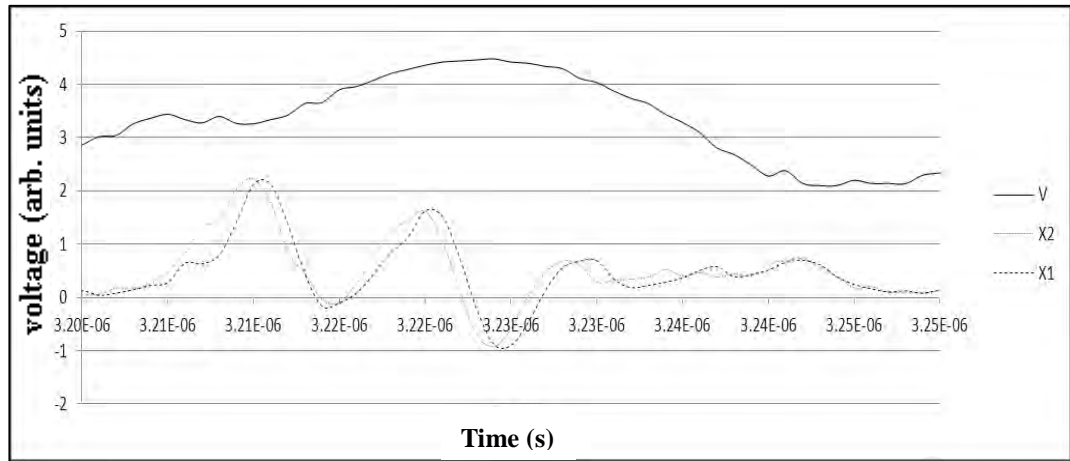


Figure 4.7: Neon X-ray (X2) and copper K-alpha (X1), X1 detected is 1 ns later after X2.

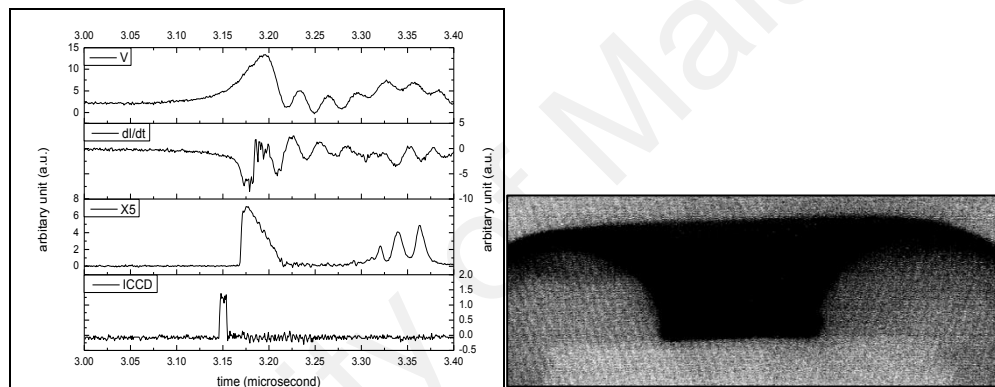


Figure 4.8 (a): Black spots (inside white circle) observed on the surface of the anode at sharp drop of dI/dt for before dI/dt sharp drop.

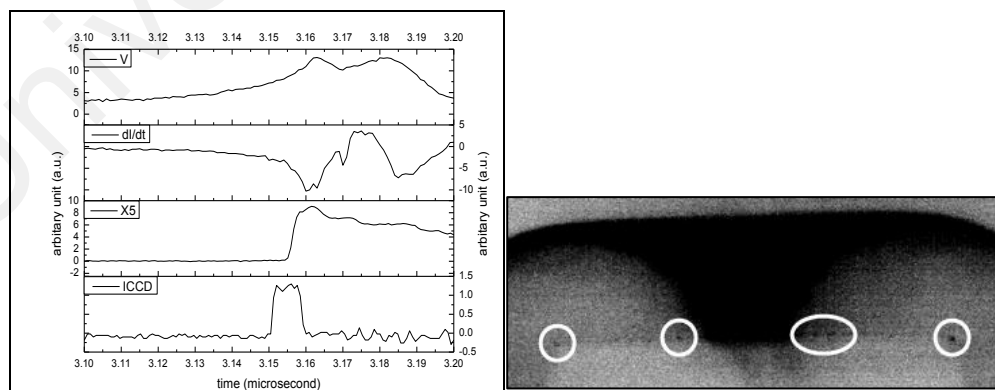


Figure 4.8 (a): Black spots (inside white circle) observed on the surface of the anode at sharp drop of dI/dt for when dI/dt sharp drop.

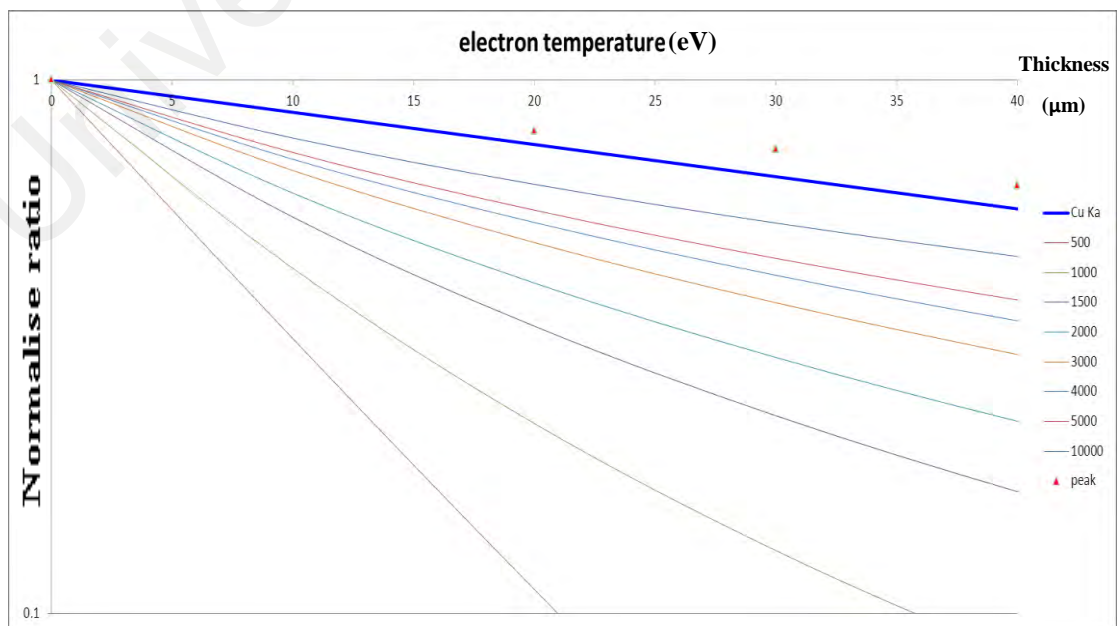
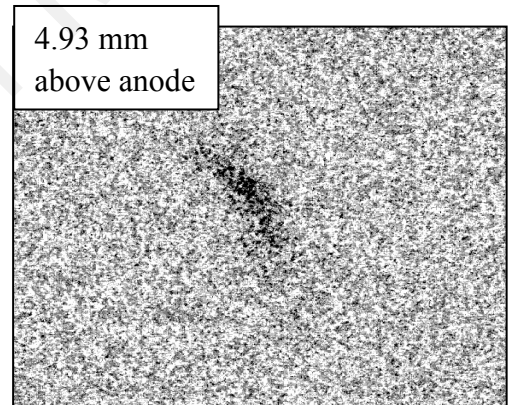
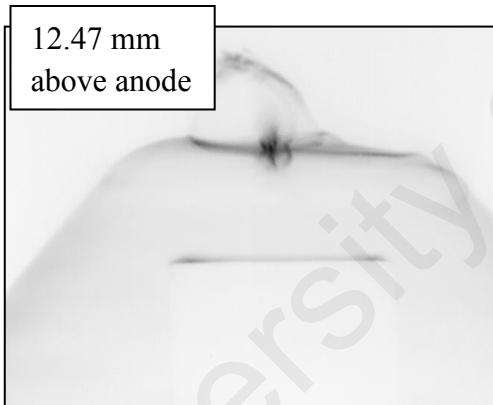
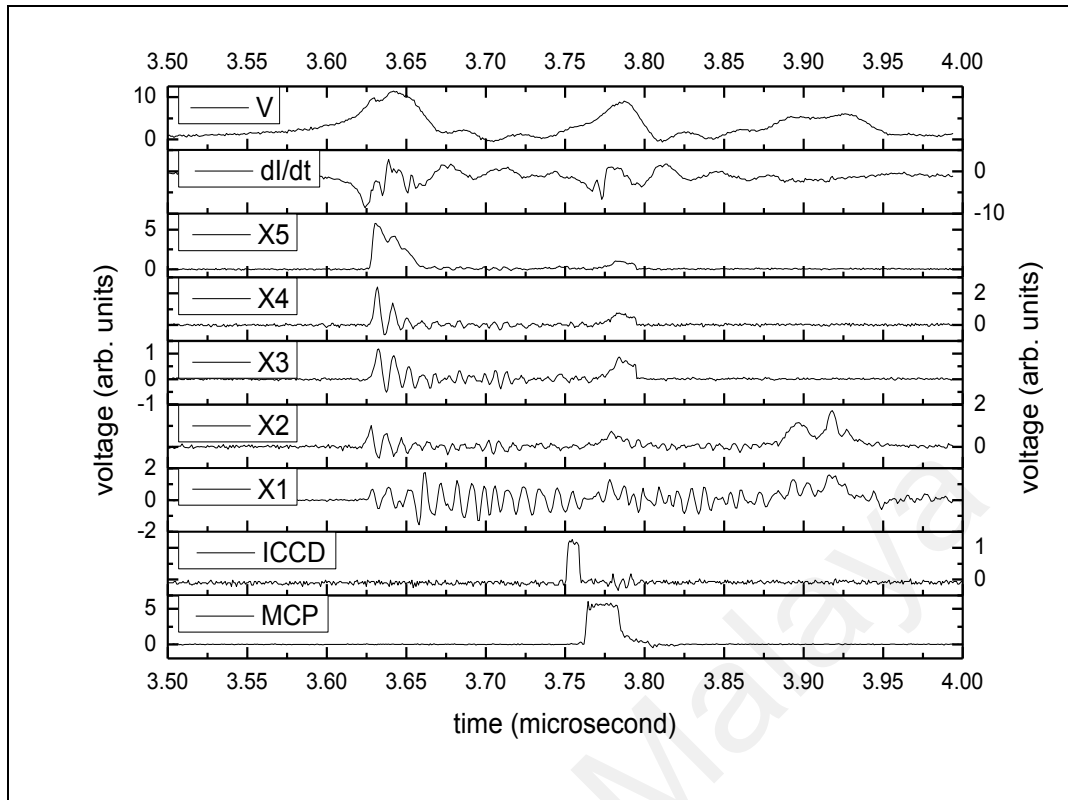


Figure 4.9: Second region pinch image.

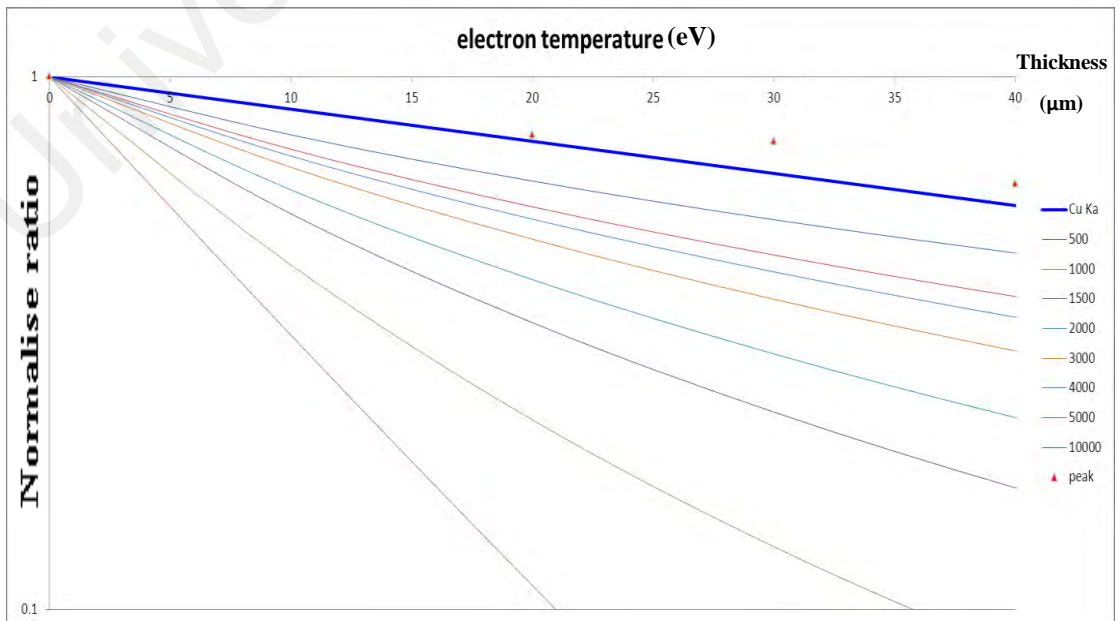
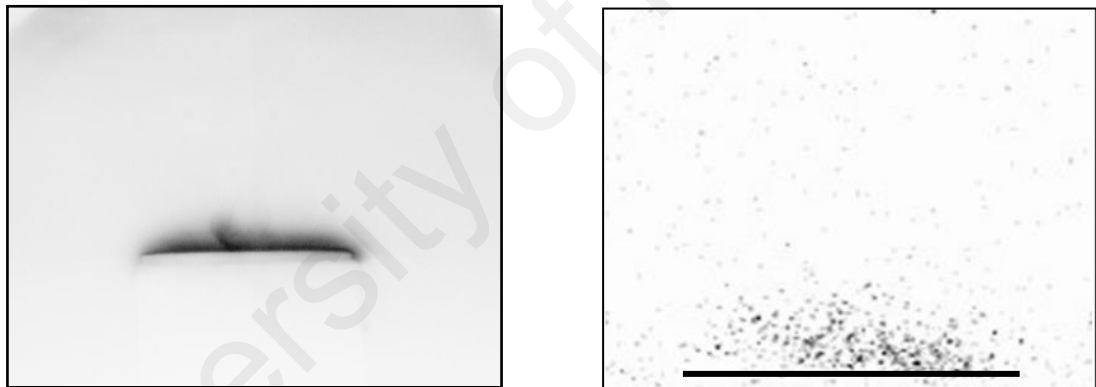
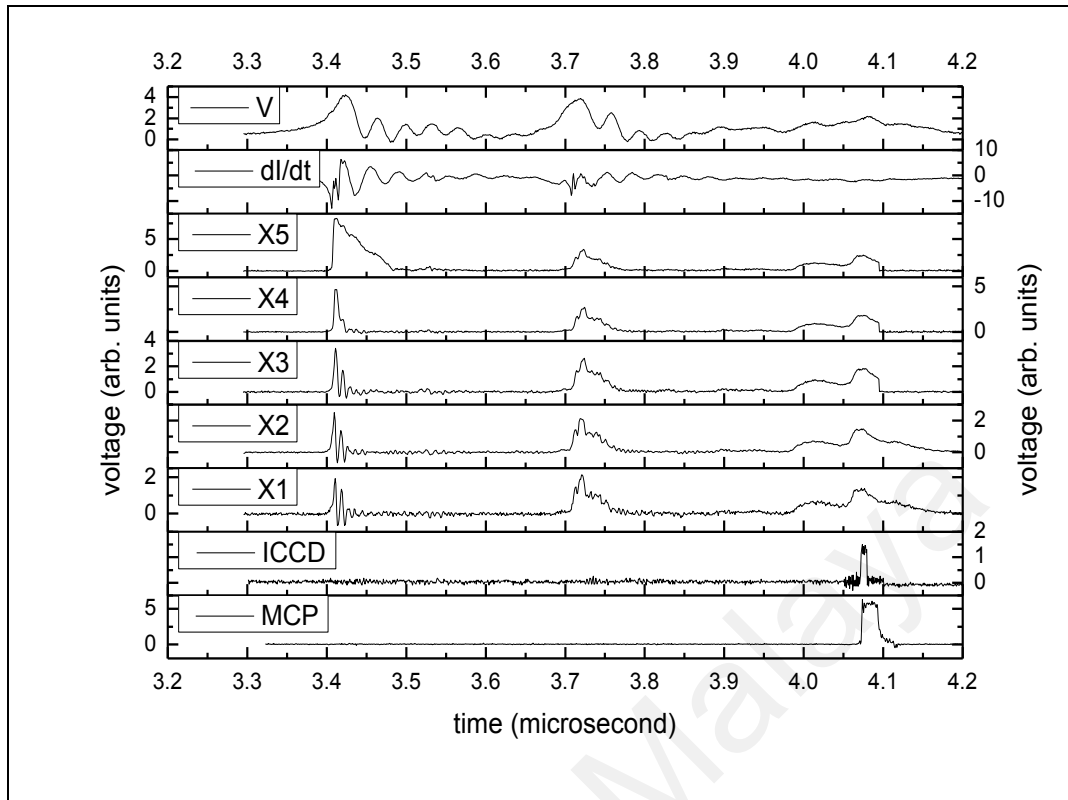


Figure 4.10: Third region pinch image.

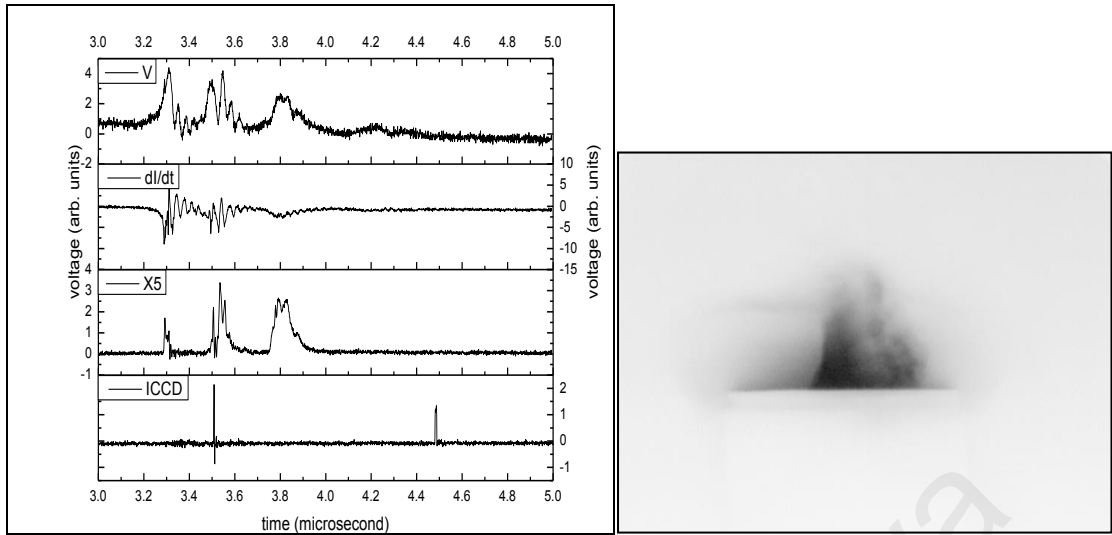


Figure 4.11 (a): After third region pinch for more copper vaporized.

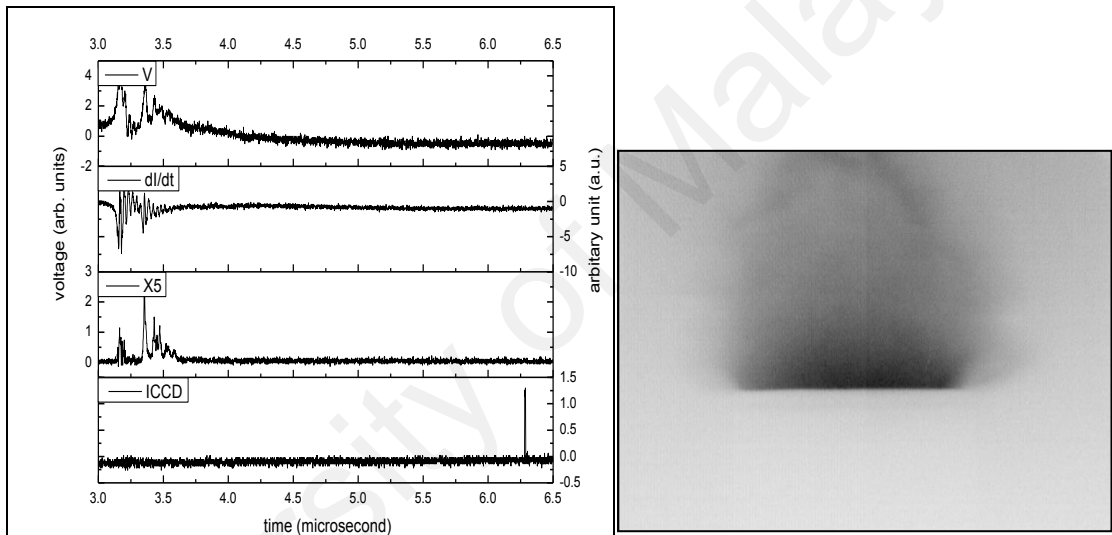


Figure 4.11 (b): After third region pinch for copper vapour diffuse into surrounding.

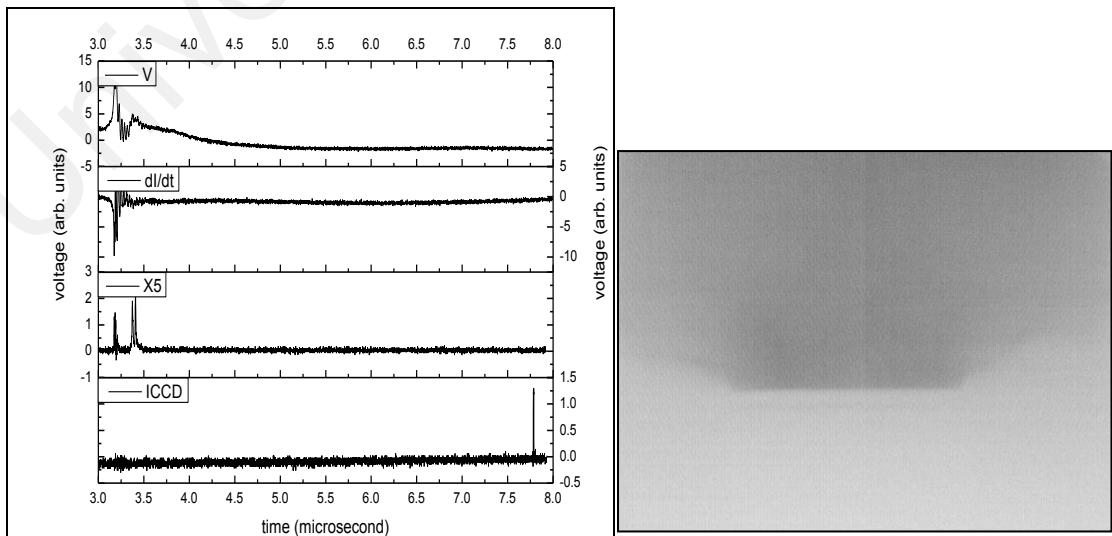


Figure 4.11 (c): After third region pinch for copper vapour diffuse into surrounding.

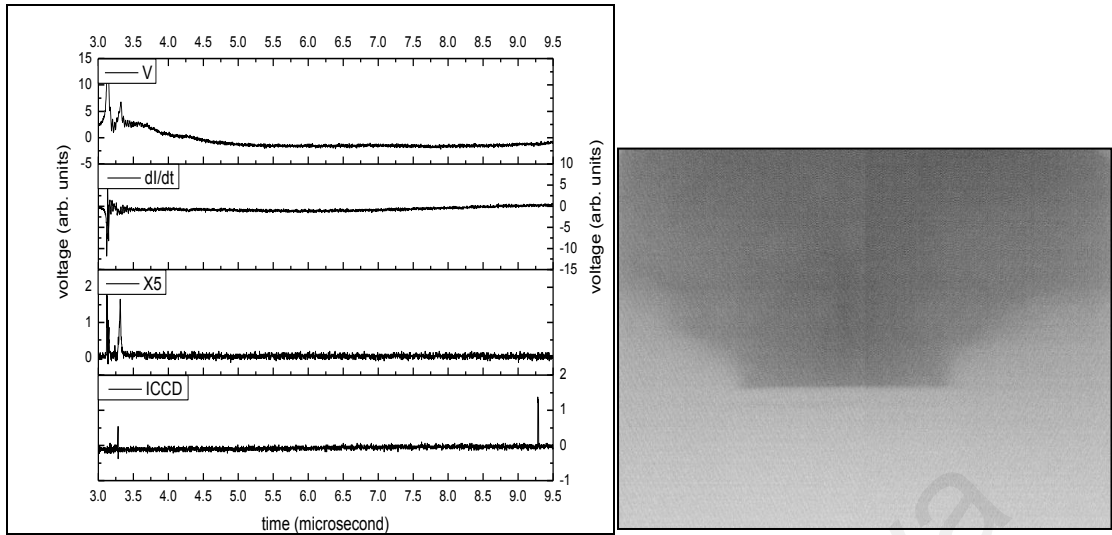


Figure 4.11 (d): After third region pinch for copper vapour starts compressed when V goes into positive cycle.

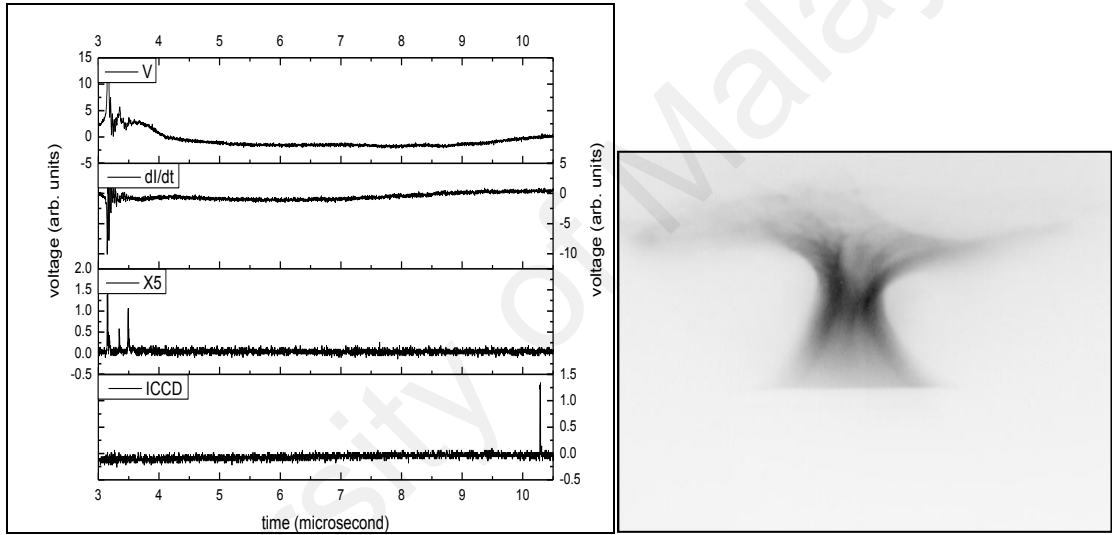


Figure 4.11 (e): After third region pinch for copper vapour compressed.

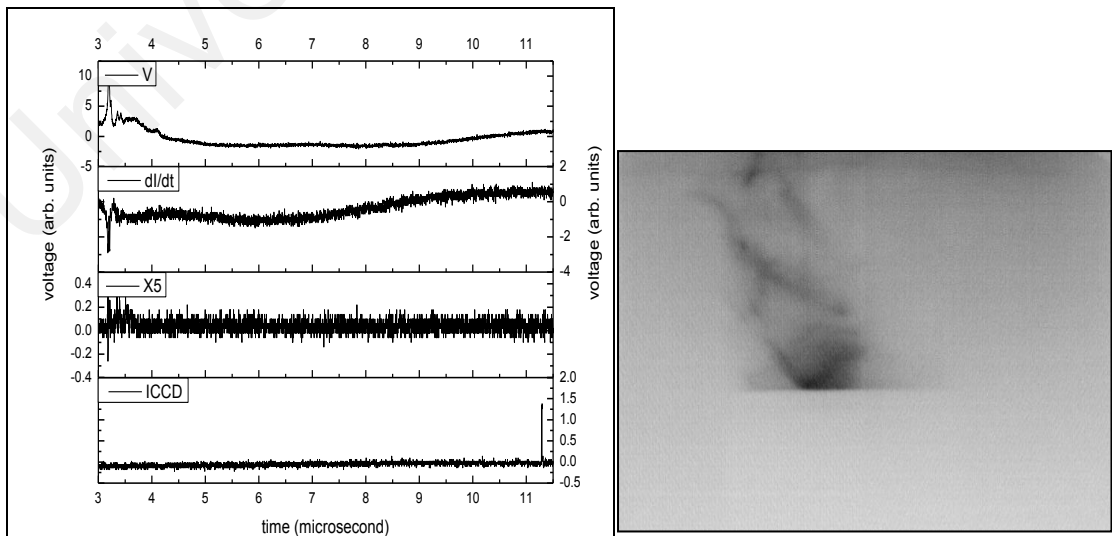


Figure 4.11 (f): After third region pinch for compression continues.

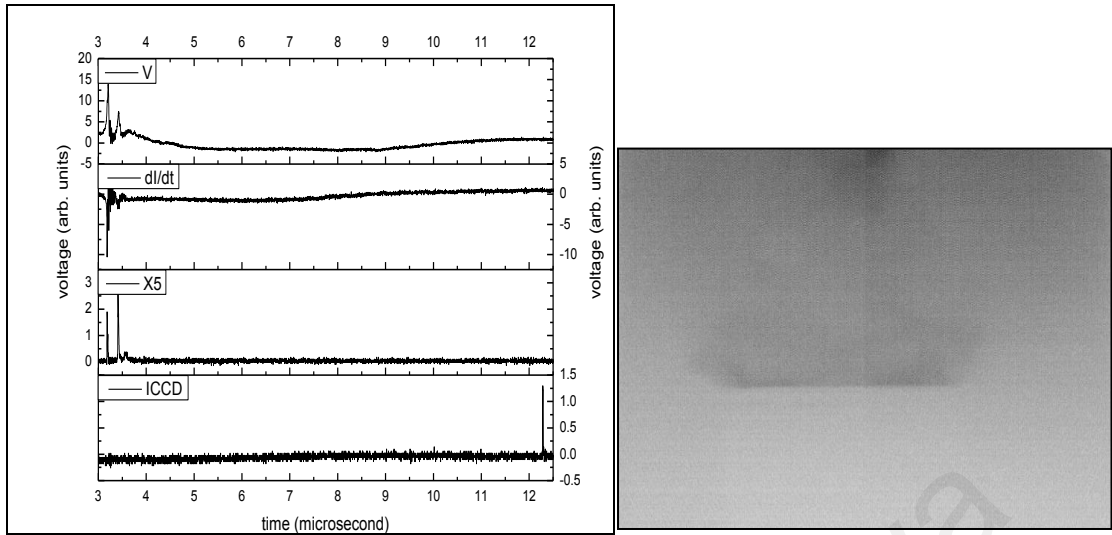


Figure 4.11 (g): After third region pinch for starts to diffuse when V enter reverse cycle.

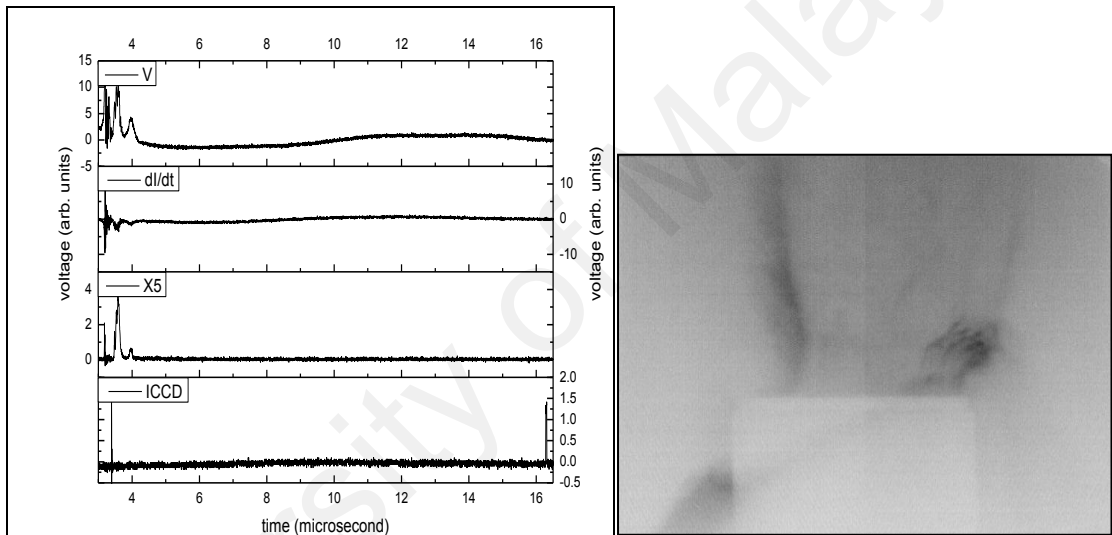


Figure 4.11 (h): After third region pinch for diffusion continues.

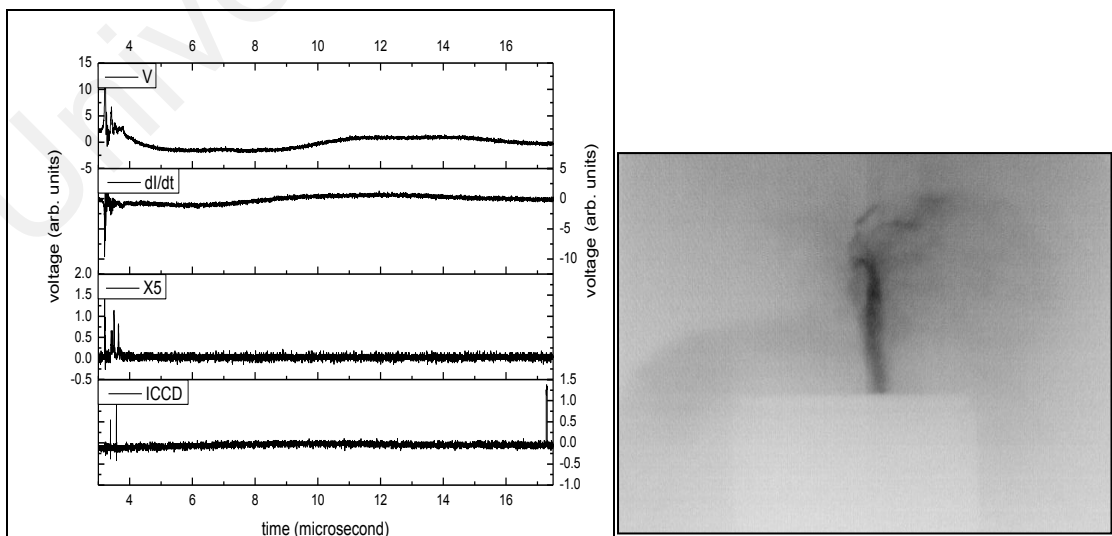


Figure 4.11 (i): After third region pinch for re-compressed again, and starts diffuse when enter reverse cycle.

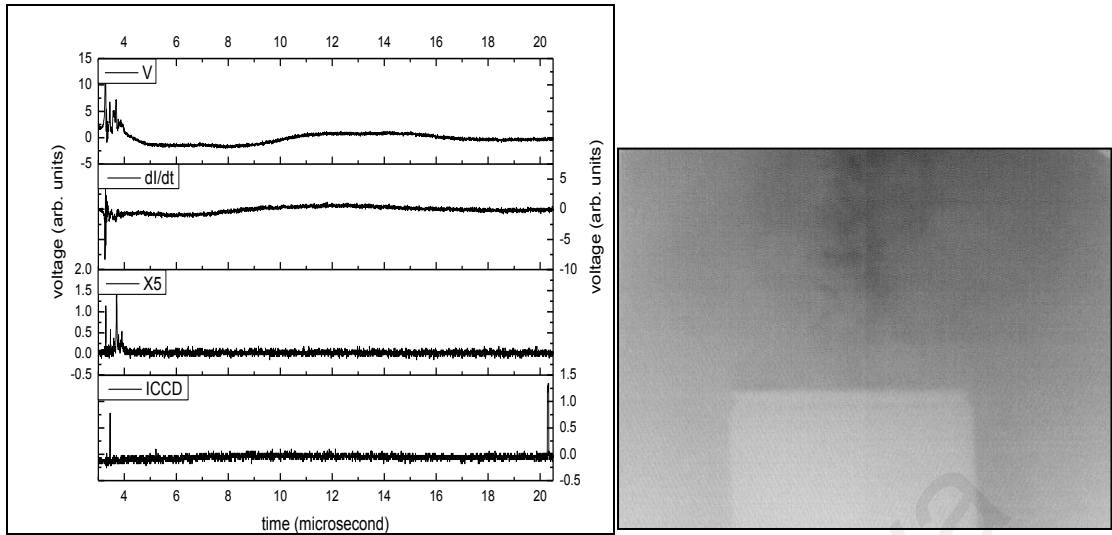


Figure 4.11 (j): After third region pinch for diffuse into surrounding.

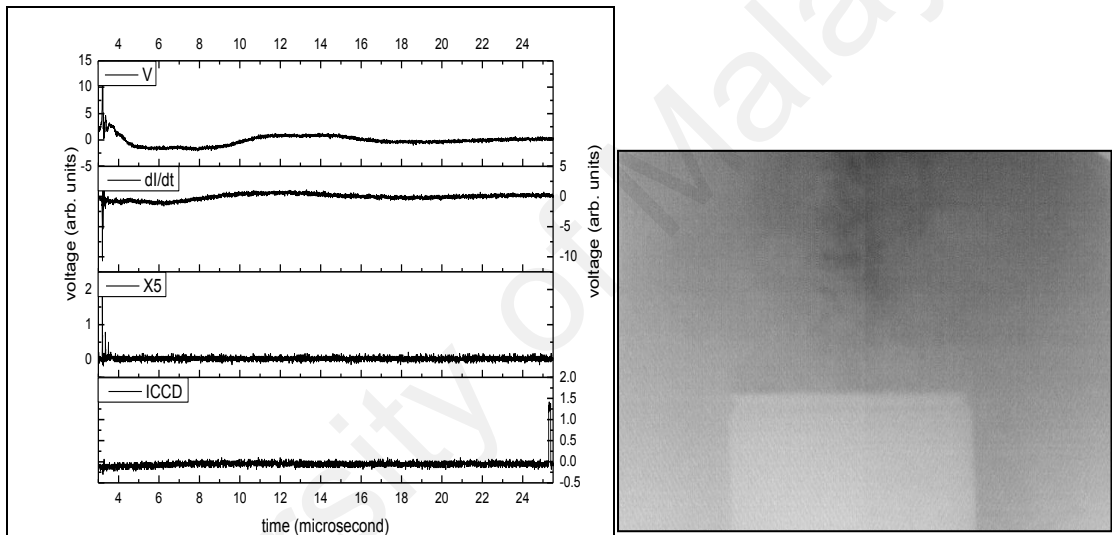


Figure 4.11 (k): After third region pinch for diffuse into surrounding.

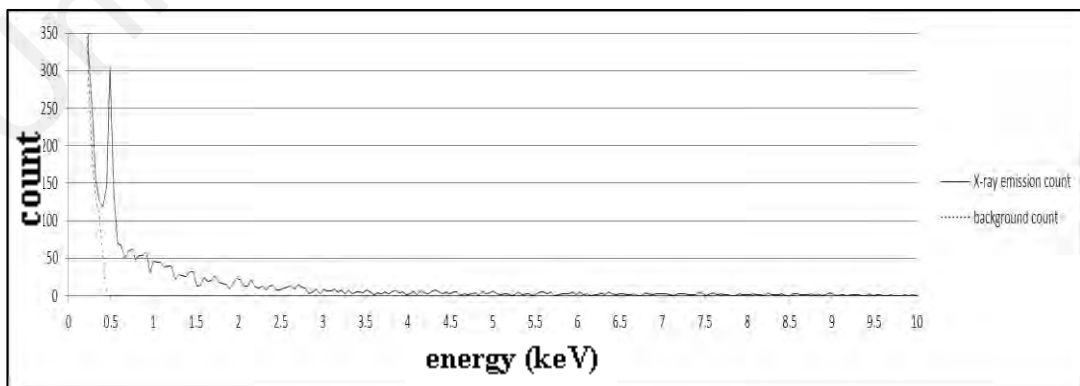


Figure 4.12: X-ray spectrometer accumulated 234 successive shots, below 400 eV are majority background radiation, majority of Neon X-ray is 500 eV but both PIN diode detector and MCP are not sensitive to 500 eV range.

CHAPTER 5: CONCLUSION

The radial compression phase of neon plasma focus device is investigated by employing multiple diagnostic techniques. ICCD and MCP imaging give good time resolution with aperture of 5 ns or 20 ns but operated independently. Thus the frames imaged in a single shot are correlated in time by referring to the opening time of the devices. A series of images have been compiled to show the whole compression phase by carefully selected shots that could reveal the plasma at different time. In the current setup, multiple compressions of neon plasma focus is often obtained and allow us to clearly identify the multiple regions in the radial compression phase. Analysis of the emission correlated to the three regions shown that neon X-ray emission is emitted in the first region, followed by emission due to electrodes material which are dominated by copper K-alpha. The electron temperature estimated from the soft X-ray emission registered by the X-ray spectrometer is 500 eV while the highest electron temperature could be obtained at around 10 keV due to the combination of neon X-ray and copper X-ray emission.

The multiple peaks in the dI/dt signal and the discharge voltage signals are correlated to the multiple compressions of the current sheath or plasma column breaks into hot spots during the plasma pinch. Several conditions are analyzed as following:

- i. During and approximately to the peak of the dI/dt signal, before the first peak of discharge voltage, is the first compression period of current sheath, X-ray emission is observed.
- ii. During the sharp drop of the dI/dt signal and rise of discharge voltage, ablation of anode due to electron bombardment is observed
- iii. Approximately and during the first peak of discharge voltage, elongation of plasma column is observed.
- iv. After the first peak of the dI/dt signal to the first peak of discharge voltage, it has been observed plasma column breaks-up into hot spots.
- v. Between the first peak of the dI/dt signal to the second peak of discharge voltage, X-ray emissions and second compression are observed. The electron temperature is less than that of the first compression.
- vi. The peak of the dI/dt signal that is close to the second peak of discharge voltage corresponds in time with the second formation of hot spots.
- vii. After the second peak of discharge voltage, the broad pulse of dI/dt indicates duration where plasma bubble started to form on the top of the current sheath.

- viii. The ablation of anode occurred more frequently, more copper material is vaporized until a layer of visible light is clearly observed on the anode's surface.
- ix. This is followed by the second region pinch occurred inside the plasma bubble.
- x. The third region pinches occurred at later stage, the formation is still uncertain. It is believed that either sputtering of anode material (Rafique et al., 2010) provided material for another plasma bubble after the first plasma bubble. A third pinch could occur inside the plasma bubble.
- xi. After the third region pinch, the large amount of copper vapour still continue to compressed, decay/diffused, re-compressed and decay/diffused again. No X-ray emission is observed.
- xii. The whole process from the breakdown phase until the end after the copper vapour diffuse into surrounding takes around 25 μ s.

SUGGESTION FOR FUTURE WORK

In current work due to constraint in the existing setup, the multiple diagnostics are at the best positions that can be aligned. This can be improved in a new setup if the four channels MCP position should be same with X-ray film especially the angle position which will block part of the images near the anode's surface. For the imaging techniques (ICCD, MCP and X-ray film), the camera and pinhole can be aligned closer to the source for clearer imaging. On the other hand, MCP, PIN diode detector and X-ray film not correlated well. As they are filters which are independent of each other. Similar filters should be used for better correlated. An X-ray film of better sensitivity also can be used. The ratio method by using different set of filters can be planned according to the requirement such as high or low electron temperature range.

These set of diagnostics techniques also can be setup together with neutron diagnostics techniques to reveal the evolution plasma focus fusion. Simple gas like hydrogen and deuterium are suggested for the imaging techniques. Hence, a better understanding can be achieved leading to the enhancement of plasma focus fusion.

REFERENCES

- Afsharmanesh, M., & M. Habibi. (2013). Experimental study and analysis of multiple peaks in the SXR emitted from a 4 kJ plasma focus device. *European Physical Journal D*, 67(4).
- Akel, M., S. Al-Hawat, & S. Lee. (2009). Numerical experiments on soft X-ray emission optimization of nitrogen plasma in 3 kJ plasma focus SY-1 using modified lee model. *Journal of Fusion Energy*, 28(4), 355-363.
- Akel, M., S. Alsheikh Salo, & C. S. Wong. (2013a). Computational Study of Emitted Spectra from the Neon Plasma Focus. *Journal of Fusion Energy*, 32(4), 503-508.
- Akel, M., S. Alsheikh Salo, & C. S. Wong. (2013b). Electron temperature measurement of argon focussed plasma based on non-local thermodynamic equilibrium model. *Journal of Fusion Energy*, 32(3), 350-354.
- Al-Hawat, S. (2004). Axial velocity measurement of current sheath in a plasma focus device using a magnetic probe. *IEEE Transactions on Plasma Science*, 32(2 III), 764-769.
- Asif, M., & G. S. Xu. (2004). Plasma electron temperature measurement in a mather-type plasma focus filled with hydrogen by a continuum intensity analysis. *Plasma Devices and Operations*, 12(1), 31-38.
- Borowiecki, M., B. Bieñkowska, S. Jednoróg, L. Karpiński, M. Paduch, M. Scholz, & M. J. Sadowski. (2006). Investigation of pinch dynamics in plasma-focus discharges by means of fast-streak-and fast-frame-cameras. *Czechoslovak Journal of Physics*, 56(SUPPL. 2), B184-B191.
- Chen, Y. H. (1972). *Study of Coaxial Plasma Guns In Mode I Operation*. Master, University of Malaya.
- Choi, P., C. S. Wong, & H. Herold. (1989). Studies of the spatial and temporal evolution of a dense plasma focus in the X-ray region. *Laser and Particle Beams*, 7 pt 4, 763-772.

- Chung, H. K., M. H. Chen, W. L. Morgan, Y. Ralchenko, & R. W. Lee. (2005). FLYCHK: Generalized population kinetics and spectral model for rapid spectroscopic analysis for all elements. *High Energy Density Physics*, 1(1), 3-12.
- Decker, G., W. Kies, R. Nadolny, P. Röwekamp, F. Schmilz, G. Ziethen, . . . & Y. V. Sopykin. (1996). Micropinch actuation in the SPEED 2 plasma focus. *Plasma Sources Science and Technology*, 5(1), 112-118.
- Favre, M., S. Lee, S. P. Moo, & C. S. Wong. (1992). X-ray emission in a small plasma focus operating with H₂-Ar mixtures. *Plasma Sources Science and Technology*, 1(2), 122-125.
- Favre, M., P. Silva, P. Choi, H. Chuaqui, C. Dumitrescu-Zoita, & E. S. Wyndham. (1998). Experimental investigations of hotspots in a low energy plasma focus operating in hydrogen-argon mixtures. *IEEE Transactions on Plasma Science*, 26(4), 1154-1161.
- Filippov, N. V., T. I. Filippova, & V. P. Vinogradov. (1962). Dense, high-temperature plasma in a noncylindrical 2-pinch compression. *Nuclear Fusion Supplement Pt. 2*, 577.
- Goh, B. T., S. K. Ngoi, S. L. Yap, C. S. Wong, & S. Abdul Rahman. (2013). Improvements in the structural and optical properties of a-Si:H by a dense plasma focus. *Materials Science in Semiconductor Processing*, 16(6), 1925-1930.
- Goudarzi, S., H. Babae, A. Esmali, & A. Nasiri. (2017). Experimental study of the performance of a very small repetitive plasma focus device in different working conditions. [journal article]. *Plasma Physics Reports*, 43(1), 94-98.
- Gribkov, V. A., A. Banaszak, B. Bienkowska, A. V. Dubrovsky, I. Ivanova-Stanik, L. Jakubowski, . . . & K. Tomaszewski. (2007). Plasma dynamics in the PF-1000 device under full-scale energy storage: II. Fast electron and ion characteristics versus neutron emission parameters and gun optimization perspectives. *Journal of Physics D: Applied Physics*, 40(12), 3592.

- Gribkov, V. A., B. Bienkowska, M. Borowiecki, A. V. Dubrovsky, I. Ivanova-Stanik, L. Karpinski, . . . & K. Tomaszewski. (2007). Plasma dynamics in PF-1000 device under full-scale energy storage: I. Pinch dynamics, shock-wave diffraction, and inertial electrode. *Journal of Physics D: Applied Physics*, 40(7), 1977-1989.
- Hirano, K., Y. Tagaya, K. Shimoda, Y. Okabe, & T. Yamamoto. (1986). Time correlation between plasma behaviour and soft X-ray emission in a plasma focus. *Journal of the Physical Society of Japan*, 55(7), 2211-2216.
- Hirano, K., T. Yamamoto, K. Shimoda, & Y. Tagaya. (1985). Correlation between time-resolved soft X-ray images and interferometric results in a plasma focus. *Japanese Journal of Applied Physics, Part 1: Regular Papers & Short Notes*, 24(11), 1514-1517.
- Jahoda, F. C., E. M. Little, W. E. Quinn, G. A. Sawyer, & T. F. Stratton. (1960). Continuum radiation in the X Ray and visible regions from a magnetically compressed plasma (Scylla). *Physical Review*, 119(3), 843-856.
- Jakubowski, L., M. Sadowski, & E. O. Baronova. (2000). Space-resolved studies of X-ray spectra within plasma-focus system. *Czechoslovak Journal of Physics*, 50(SUPPL. 3), 173-178.
- Jakubowski, L., & M. J. Sadowski. (2002). Hot-spots in Plasma-Focus discharges as intense sources of different radiation pulses. *Brazilian Journal of Physics*, 32(1), 187-192.
- Jakubowski, L., M. J. Sadowski, & E. O. Baronova. (2004). X-ray polarization studies of plasma focus experiments with a single hot spots. *Nuclear Fusion*, 44(3), 395-399.
- Kalaiselvi, S. M. P., T. L. Tan, A. Talebitaher, P. Lee, & R. S. Rawat. (2015). Neon soft x-ray lithography source based on low energy fast miniature plasma focus device C3 - ICOPS/BEAMS 2014 - 41st IEEE International Conference on Plasma Science and the 20th International Conference on High-Power Particle Beams 41st IEEE International Conference on Plasma Science, ICOPS 2014 and the 20th IEEE International Conference on High-Power Particle Beams, BEAMS 2014: Institute of Electrical and Electronics Engineers Inc.

- Kwek, K. H. (1989). *Pinch Structure of A Plasma Focus*. Phd, University of Malaya, Kuala Lumpur, Malaysia.
- Kwek, K. H., T. Y. Tou, & S. Lee. (1990). Current sheath structures of the plasma focus in the run-down phase. *IEEE Transactions on Plasma Science*, 18(5), 826-830.
- Lee, S. (1984). Electromagnetic Shock Tube. In B. C. T. S. Lee, C. S. Wong, A. C. Chew (Ed.), *Laser and Plasma Technology: proceedings of the First Tropical College on Applied Physics* (pp. 3-35). Physics Department, University of Malaya, Kuala Lumpur, Malaysia.
- Lee, S. (2014). Plasma Focus Radiative Model: Review of the Lee Model Code. *Journal of Fusion Energy*, 1-17.
- Lim, L. H., S. L. Yap, S. H. Saw, H. S. Poh, M. C. Lee, & S. Lee. (2017). Amending the reflected shock phase of the Lee code. *AIP Conference Proceedings*, 1824(1), 030010.
- Lim, L. K., S. L. Yap, L. H. Lim, Y. S. Neoh, M. Z. Khan, S. K. Ngoi, . . . & S. Lee. (2016). Parametric Optimisation of Plasma Focus Devices for Neutron Production. [journal article]. *Journal of Fusion Energy*, 35(2), 274-280.
- Lim, L. K., S. L. Yap, C. S. Wong, & M. Zakaullah. (2013). Deuteron beam source based on mather type plasma focus. *Journal of Fusion Energy*, 32(2), 287-292.
- Mather, J. W. (1965). Formation of a high-density deuterium plasma focus. *Physics of Fluids*, 8(2), 366-377.
- Mather, J. W. (1971). Dense plasma focus. In H. L. Ralph & R. G. Hans (Eds.), *Methods of experimental physics* (Vol. 9-Part B, pp. 187-249). New York and London: Academic Press.
- Momenei, M., Z. Khodabakhsh, N. Panahi, & M. A. Mohammadi. (2017). Experimental investigation of the effect of insulator sleeve length on the time to pinch and multipinch formation in the plasma focus facility. [journal article]. *Journal of Theoretical and Applied Physics*, 11(1), 59-62.

- Neog, N. K., S. R. Mohanty, & T. K. Borthakur. (2008). Time resolved studies on X-rays and charged particles emission from a low energy plasma focus device. *Physics Letters, Section A: General, Atomic and Solid State Physics*, 372(13), 2294-2299.
- Ng, C. M., S. P. Moo, & C. S. Wong. (1998). Variation of soft X-ray emission with gas pressure in a plasma focus. *IEEE Transactions on Plasma Science*, 26(4), 1146-1153.
- Raeisdana, A., A. Sadighzadeh, A. Ghorbani, M. Bakhshzad Mahmoudi, M. Babaei, & V. Damideh. (2017). Numerical Experiments on IR-MPF-100 Plasma Focus Operated in Neon and Deuterium Gases. [journal article]. *Journal of Fusion Energy*, 1-7.
- Rafique, M. S. (2000). *Compression Dynamic And Radiation Emission From A Deuterium Plasma Focus*. Phd, Nanyang Technological University, Singapore.
- Rafique, M. S., P. Lee, A. Patran, R. S. Rawat, & S. Lee. (2010). Radiation emission correlated with the evolution of current sheath from a deuterium plasma focus. *Journal of Fusion Energy*, 29(3), 295-304.
- Rawat, R. S., T. Zhang, C. B. L. Phua, J. X. Y. Then, K. A. Chandra, X. Lin, . . . & P. Lee. (2004). Effect of insulator sleeve length on soft x-ray emission from a neon-filled plasma focus device. *Plasma Sources Science and Technology*, 13(4), 569-575.
- Saw, S. H., M. Akel, P. C. K. Lee, S. T. Ong, S. N. Mohamad, F. D. Ismail, . . . & S. Lee. (2012). Magnetic probe measurements in INTI plasma focus to determine dependence of axial speed with pressure in neon. *Journal of Fusion Energy*, 31(5), 411-417.
- Saw, S. H., P. L. Chong, R. S. Rawat, C. T. L. Ching, P. Lee, A. Talebitaher, & S. Lee. (2014). The effect of specific heat ratio on neutron yield. *IEEE Transactions on Plasma Science*, 42(1), 99-104.
- Shad Sanjabad, M., B. Shirani Bidabadi, & I. Jabbari. (2017). Characteristics of X-ray Hot Spots in a 3.5 kJ Plasma Focus Device at Different Pressures of Argon and Air. [journal article]. *Journal of Fusion Energy*, 1-7.

- Soh, L. Y., P. Lee, X. Shuyan, S. Lee, & R. S. Rawat. (2004). Shadowgraphic studies of DLC film deposition process in dense plasma focus device. *IEEE Transactions on Plasma Science*, 32(2 I), 448-455.
- Soto, L., C. Pavez, J. Moreno, M. J. Inestrosa-Izurieta, F. Veloso, G. Gutiérrez, . . . & L. F. Delgado-Aparicio. (2014). Characterization of the axial plasma shock in a table top plasma focus after the pinch and its possible application to testing materials for fusion reactors. *Physics of Plasmas*, 21(12).
- Talukdar, N., T. K. Borthakur, & N. K. Neog. (2011). Studies on X-ray and neutron emission from 2.2 KJ plasma focus device. *Problems of Atomic Science and Technology*(1), 125-127.
- Tzeng, C. C., C. K. Yen, Y. J. Yu, Y. Y. Kuo, M. Wen, W. S. Hou, & T. R. Yeh. (1992). Plasma dynamics and hotspots studies from a plasma focus device *High-Power Particle Beams, 1992 9th International Conference on* (Vol. 3, pp. 1984-1989).
- Vinogradov, V. P., V. I. Krauz, A. N. Mokeev, V. V. Myalton, & A. M. Kharrasov. (2016). Dynamics of the plasma current sheath in plasma focus discharges in different gases. [journal article]. *Plasma Physics Reports*, 42(12), 1079-1090.
- Wong, C. S., S. P. Moo, J. Singh, P. Choi, C. Dumitrescu-Zoita, & C. Silawatshananai. (1996). Dynamics of X-ray emission from a small plasma focus. *Malaysian Journal of Science*, 17B, 109-117.
- Yap, S. L., & C. S. Wong. (2003). Deuteron Beam Production in a 3kJ Plasma Focus Device (pp. 244). Jeju.

LIST OF PUBLICATION AND PAPERS PRESENTED

Lee, M. C., Lee, S. and Yap, S. L., Compression Dynamics And X-ray Emission From A Neon Plasma Focus, 10th Asian-Europe International Conference On Plasma Engineering, Ramada Plaza Jeju Hotel, Jeju Island (Korea), 20 – 24 September 2015

Lee, M. C., Lee, S. and Yap, S. L., X-ray Emission In A Neon Plasma Focus, Physics Colloquium 2015, Department of Physics, University of Malaya, Kuala Lumpur (Malaysia), 10 – 11 June 2015

University of Malaya